Development of a substructuring approach to model the vibroacoustic behavior of submerged stiffened cylindrical shells coupled to non-axisymmetric internal frames

Valentin Meyer

▶ **To cite this version:**

Valentin Meyer. Development of a substructuring approach to model the vibroacoustic behavior of submerged stiffened cylindrical shells coupled to non-axisymmetric internal frames. Acoustics [physics.class-ph]. INSA de Lyon, 2016. English. NNT : 2016LYSEI111 . tel-01416015v1

HAL Id: tel-01416015

https://hal.science/tel-01416015v1

Submitted on 13 Dec 2016 (v1), last revised 1 Feb 2019 (v2)

HAL is a multi-disciplinary open access archive for the deposit and dissemination of scientific research documents, whether they are published or not. The documents may come from teaching and research institutions in France or abroad, or from public or private research centers.

L'archive ouverte pluridisciplinaire **HAL**, est destinée au dépôt et à la diffusion de documents scientifiques de niveau recherche, publiés ou non, émanant des établissements d'enseignement et de recherche français ou étrangers, des laboratoires publics ou privés.

N°d'ordre NNT : 2016LYSEI111

THESE de DOCTORAT DE L'UNIVERSITE DE LYON
opérée au sein de
l'INSA de Lyon

Ecole Doctorale N° 162
Mécanique - Energétique - Génie civil – Acoustique

Spécialité de doctorat : Acoustique

Soutenue publiquement le 28/10/2016, par :
Valentin Meyer
Ingénieur diplômé de l'ENSTA ParisTech

Development of a substructuring approach to model the vibroacoustic behavior of submerged stiffened cylindrical shells coupled to non-axisymmetric internal frames

---

Devant le jury composé de :

Christian Audoly	HDR, DCNS Research, Ollioules	Examinateur
Wim Desmet	Professeur des universités, KU Leuven	Rapporteur
Jean-Louis Guyader	Professeur des universités, INSA Lyon	Co-Directeur de thèse
Nicole Kessissoglou	Maître de conférences HDR, UNSW, Sydney	Rapporteure
Cédric Maury	Professeur des universités, LMA, Marseille	Président du jury
Laurent Maxit	Maitre de conférences HDR, INSA Lyon	Directeur de thèse

Département FEDORA – INSA Lyon - Ecoles Doctorales – Quinquennal 2016-2020

SIGLE	ECOLE DOCTORALE	NOM ET COORDONNEES DU RESPONSABLE
CHIMIE	**CHIMIE DE LYON** **http://www.edchimie-lyon.fr** Sec : Renée EL MELHEM Bat Blaise Pascal 3e etage secretariat@edchimie-lyon.fr Insa : R. GOURDON	M. Stéphane DANIELE Institut de Recherches sur la Catalyse et l'Environnement de Lyon IRCELYON-UMR 5256 Équipe CDFA 2 avenue Albert Einstein 69626 Villeurbanne cedex directeur@edchimie-lyon.fr
E.E.A.	**ELECTRONIQUE, ELECTROTECHNIQUE, AUTOMATIQUE** **http://edeea.ec-lyon.fr** Sec : M.C. HAVGOUDOUKIAN Ecole-Doctorale.eea@ec-lyon.fr	M. Gérard SCORLETTI Ecole Centrale de Lyon 36 avenue Guy de Collongue 69134 ECULLY Tél : 04.72.18 60.97 Fax : 04 78 43 37 17 Gerard.scorletti@ec-lyon.fr
E2M2	**EVOLUTION, ECOSYSTEME, MICROBIOLOGIE, MODELISATION** **http://e2m2.universite-lyon.fr** Sec : Safia AIT CHALAL Bat Darwin - UCB Lyon 1 04.72.43.28.91 Insa : H. CHARLES Safia.ait-chalal@univ-lyon1.fr	Mme Gudrun BORNETTE CNRS UMR 5023 LEHNA Université Claude Bernard Lyon 1 Bât Forel 43 bd du 11 novembre 1918 69622 VILLEURBANNE Cédex Tél : 06.07.53.89.13 e2m2@ univ-lyon1.fr
EDISS	**INTERDISCIPLINAIRE SCIENCES-SANTE** **http://www.ediss-lyon.fr** Sec : Safia AIT CHALAL Hôpital Louis Pradel - Bron 04 72 68 49 09 Insa : M. LAGARDE Safia.ait-chalal@univ-lyon1.fr	Mme Emmanuelle CANET-SOULAS INSERM U1060, CarMeN lab, Univ. Lyon 1 Bâtiment IMBL 11 avenue Jean Capelle INSA de Lyon 696621 Villeurbanne Tél : 04.72.68.49.09 Fax :04 72 68 49 16 Emmanuelle.canet@univ-lyon1.fr
INFOMATHS	**INFORMATIQUE ET MATHEMATIQUES** **http://infomaths.univ-lyon1.fr** Sec :Renée EL MELHEM Bat Blaise Pascal 3e etage infomaths@univ-lyon1.fr	Mme Sylvie CALABRETTO LIRIS – INSA de Lyon Bat Blaise Pascal 7 avenue Jean Capelle 69622 VILLEURBANNE Cedex Tél : 04.72. 43. 80. 46 Fax 04 72 43 16 87 Sylvie.calabretto@insa-lyon.fr
Matériaux	**MATERIAUX DE LYON** **http://ed34.universite-lyon.fr** Sec : M. LABOUNE PM : 71.70 –Fax : 87.12 Bat. Saint Exupéry Ed.materiaux@insa-lyon.fr	M. Jean-Yves BUFFIERE INSA de Lyon MATEIS Bâtiment Saint Exupéry 7 avenue Jean Capelle 69621 VILLEURBANNE Cedex Tél : 04.72.43 71.70 Fax 04 72 43 85 28 Ed.materiaux@insa-lyon.fr
MEGA	**MECANIQUE, ENERGETIQUE, GENIE CIVIL, ACOUSTIQUE** **http://mega.universite-lyon.fr** Sec : M. LABOUNE PM : 71.70 –Fax : 87.12 Bat. Saint Exupéry mega@insa-lyon.fr	M. Philippe BOISSE INSA de Lyon Laboratoire LAMCOS Bâtiment Jacquard 25 bis avenue Jean Capelle 69621 VILLEURBANNE Cedex Tél : 04.72 .43.71.70 Fax : 04 72 43 72 37 Philippe.boisse@insa-lyon.fr
ScSo	**ScSo*** **http://recherche.univ-lyon2.fr/scso/** Sec : Viviane POLSINELLI Brigitte DUBOIS Insa : J.Y. TOUSSAINT viviane.polsinelli@univ-lyon2.fr	Mme Isabelle VON BUELTZINGLOEWEN Université Lyon 2 86 rue Pasteur 69365 LYON Cedex 07 Tél : 04.78.77.23.86 Fax : 04.37.28.04.48

*ScSo : Histoire, Géographie, Aménagement, Urbanisme, Archéologie, Science politique, Sociologie, Anthropologie

ABSTRACT

Many works can be found in the literature concerning the vibroacoustic modeling of submerged stiffened cylindrical shells, because of their high interest and practical use in the industrial domain, in particular for aeronautical or naval applications. However, only a few of them can take into account non-axisymmetric internal frames. Indeed, structures as for instance engine foundations or floor partitions, can play a role on the vibroacoustic behavior of the system. On one hand, analytical models to include plates or resonators into stiffened cylindrical shells are available but are limited because of their low versatility, and are thus not always representative of the industrial need. On the other hand, discretization methods, such as the Finite Element Method (FEM), are very well adapted to take into account the geometrical complexity but are limited to low frequencies regarding the size of the system and the current computational capacities, and can be unadapted for preliminary design purpose. That is why a substructuring approach called the Condensed Transfer Functions (CTF) method is proposed in the first part of this thesis. The aim is to take advantage of both analytical models and element-based models, in order to be able to deal with the geometrical complexity, and to calculate at higher frequencies than with element-based methods only. The substructuring method is developed in the general case of thin mechanical structures coupled along lines. A set of orthonormal functions called condensation functions, which depend on the curvilinear abscissa along the coupling line, is considered. This set is used as a basis for approximating and decomposing the displacements and the applied forces at the line junctions. Thanks to the definition and calculation of Condensed Transfer Functions for each uncoupled subsystem and by using the superposition principle for passive linear systems, the behavior of the coupled subsystems can be obtained. The method is first developed and validated for plates and convergence criteria are defined in relation with the size of the basis of condensation functions. The CTF method is then applied to the case of a submerged stiffened cylindrical shell with non-axisymmetric internal frames. The system is partitioned in 3 types of subsystems: the submerged shell, the axisymmetric frames (stiffeners, bulkheads) and the non-axisymmetric frames. The

submerged shell is described by a semi-analytical method based on the Flügge equations in the spectral domain. The axisymmetric frames are described by axisymmetric Finite Element models and the non-axisymmetric frames by Finite Element models.

In the second part of the thesis, the CTF method is applied to different test cases in order to study the influence of non-axisymmetric internal frames on the vibroacoustic behavior of a cylindrical shell under different types of excitation particularly relevant for naval applications. First, for the case of a point force, it can be shown that additional circumferential orders play a role in the response of the system coupled with non-axisymmetric internal frames, and that the radiation efficiency tends to increase. This trend is verified experimentally in air on a model. Then, the influence of internal structures when the system is submerged in water and impinged by an acoustic plane wave is examined. In addition to Bragg and Bloch-Floquet scattering due to interferences created by the rib periodicity, the numerical model highlights scattering phenomena due to waves propagating in the internal structures. Finally, the wavenumber-point (k, M) reciprocity technique is used complementary to the CTF method to estimate the response of a complex shell under random excitations (diffuse sound field or turbulent boundary layer for instance). Results on a test case consisting of a submerged stiffened cylindrical shell excited by a diffuse sound field and a turbulent boundary layer show the versatility of the method. In this case, the non-axisymmetric internal frames have a strong influence on the power spectral densities of the shell acceleration but a smaller influence on the power spectral density of the pressure radiated in the fluid domain.

RÉSUMÉ EN FRANÇAIS

De nombreux travaux dans la littérature se sont concentrés sur la modélisation vibro-acoustique de coques cylindriques raidies immergées, du fait des nombreuses applications industrielles, en particulier dans le domaine aéronautique ou naval. Cependant, peu d'entre elles prennent en compte des structures internes non-axisymétriques. En effet, des structures telles que des supports moteurs, des planchers ou des carlingages, peuvent avoir une influence importante sur le comportement vibro-acoustique du système. D'un côté, des modèles analytiques permettent d'inclure des plaques ou des systèmes masse-ressort dans une coque cylindrique raidie, mais ne correspondent pas bien aux besoins industriels. D'un autre côté, les méthodes de discrétisation, telle que la méthode des éléments finis (FEM) par exemple, sont très bien adaptées pour rendre compte de la complexité géométrique mais sont limités à une gamme fréquentielle relativement basse au vu de la taille du système étudié et des capacités de calcul actuelles, et ne sont donc pas toujours adaptées à des phases de conception préliminaire. C'est pourquoi une méthode de sous-structuration baptisée CTF est présentée dans la première partie de cette thèse. Elle vise à profiter des avantages respectifs des méthodes analytiques et des méthodes de discrétisation afin de pouvoir prendre en compte la complexité structurelle tout en étant capable de calculer les réponses à des fréquences plus hautes que les méthodes de discrétisation. La méthode CTF est développée dans le cas général de deux structures minces couplées le long d'une ligne. Un ensemble de fonctions orthonormées, baptisées fonctions de condensation, est défini afin d'approximer les forces et déplacements à la jonction entre les sous-systèmes. Des fonctions de transfert condensées sont définies pour chaque sous-système découplé. L'utilisation du principe de superposition, de l'équilibre des forces et de la continuité des déplacements permet de déduire le comportement des sous-systèmes couplés. La méthode est d'abord développée et validée dans le cas de plaques, et un critère de convergence est défini à partir de la taille de la base des fonctions de condensation. La méthode CTF est ensuite appliquée au cas d'une coque cylindrique raidie immergée couplée à des structures internes non-axisymétriques. Le système est dans ce cas décomposé en

3 familles de sous-systèmes : la coque cylindrique immergée, les structures internes axisymétriques (raidisseurs, cloisons) et les structures non-axisymétriques. La coque cylindrique est décrite par une méthode semi-analytique basée sur la résolution des équations de Flügge dans le domaine des nombres d'onde. Les structures axisymétriques sont décrites par des modèles éléments finis axisymétriques et les structures non-axisymétriques sont décrites pas des modèles éléments finis.

Dans une seconde partie, la méthode CTF est appliquée à différents cas tests afin d'étudier l'influence des structures internes non-axisymétriques sur le comportement vibro-acoustique d'une coque cylindrique pour différents types d'excitations pertinents dans le domaine naval. Tout d'abord, dans le cas d'une force ponctuelle, on montre qu'un plus grand nombre d'ordres circonférentiels intervient dans la réponse du système couplé aux structures internes non-axisymétriques, et que l'efficacité de rayonnement a ainsi tendance à augmenter. Cette tendance est vérifiée expérimentalement sur une maquette en air. Dans un deuxième temps, l'influence des structures internes lorsque le système est immergé dans l'eau et excité par une onde plane acoustique est étudiée. En plus des phénomènes de diffraction de Bragg et de Bloch-Floquet dus aux interférences créées par les raidisseurs périodiques, les simulations numériques mettent en évidence des phénomènes supplémentaires liés à la propagation d'ondes dans les structures internes. Enfin, le principe de réciprocité (k, M) est utilisé en complément de la méthode CTF afin d'estimer le comportement d'une structure complexe excitée par un champ de pression aléatoire (tel qu'un champ acoustique diffus ou une couche limite turbulente). Des résultats sur un exemple de coque raidie immergée montrent l'intérêt de cet outil. Dans ce cas, on remarque que les structures internes non-axisymétriques peuvent avoir une forte influence sur la densité spectrale de puissance des accélérations sur la coque, tandis que la densité spectrale de puissance de la pression à un point dans le domaine acoustique est moins influencée.

N.B. : le manuscrit étant rédigé en anglais, un résumé étendu en français peut être consulté en annexe E.

REMERCIEMENTS

Ce manuscrit et les résultats qui y sont présentés sont le fruit d'un travail de trois ans que je n'aurai pas pu réaliser seul. C'est pourquoi je tiens à remercier ici toutes les personnes qui m'ont entourées aussi bien sur le plan professionnel que personnel.

J'aimerais tout d'abord commencer par mon directeur de thèse, Laurent Maxit. Il est certain que je dois une grande partie du succès de cette thèse à sa claire vision du sujet, à sa disponibilité et à sa patience. C'était un plaisir d'échanger et de travailler ensemble lors des réunions d'avancement, ou de discussion plus informelles. J'ai également énormément apprécié travailler avec Jean-Louis Guyader, non seulement pour ses qualités de pédagogue et son expérience en vibro-acoustique, mais aussi pour les discussions dépassant le cadre de ma thèse. Je remercie Christian Audoly pour la confiance qu'il m'a accordé durant ces trois années et pour avoir su se rendre disponible et rassurant aux moments cruciaux. Je remercie Ygaël Renou, qui a eu la lourde tâche de prendre le train en marche et qui, malgré ce qu'il pourra dire, a joué un rôle important dans mon encadrement. Je remercie Nicole Kessissoglou et Wim Desmet d'avoir rapporté ma thèse, et j'apprécie énormément le fait que Nicole ait voyagé depuis Sydney pour assister à ma soutenance. Merci à Cédric Maury d'avoir accepté de présider le jury de ma thèse.

Le choix de réaliser une thèse après mon cursus d'ingénieur n'était au départ pas une évidence pour moi. C'est pourquoi je tiens à remercier Antoine Chaigne et Benjamin Cotté de m'avoir donné le goût pour la recherche en acoustique lors de mon cursus à l'ENSTA ParisTech. Céline Rousset, qui m'a encadré lors de mon stage de fin d'étude chez DCNS Research, et Thomas Leissing, qui m'a encadré lors de ma première année de thèse, ont également joué un rôle dans cette décision en me donnant envie de travailler avec eux et je leur en suis reconnaissant. J'ai également une pensée pour mes autres collègues de DCNS Research: Rania, Patrick, Gilles, François, Agathe, Adrien, Benoît, Chantal, qui me permettent de travailler quotidiennement dans une bonne ambiance. Je sais que Rania aurait été déçue si je m'arrêtais là : je n'oublie donc pas de la remercier pour les discussions de la pause café qui ne parlent pas de boulot,

pour les apéros et les sorties resto. Merci à Laurent P. d'avoir toujours cru en moi. Je remercie Audrey, Jean, Enzo et Stef pour les pauses musicales qui m'ont permis de décompressersur la fin de ma thèse.

Durant ces trois ans, j'ai passé une grande partie de mon temps au LVA, et je m'y suis senti très bien. Je remercie tous les doctorants et post-doctorants : Youssef, qui m'a appris énormément de choses ; Ben et Coco avec qui j'ai partagé les galères, les voyages et les organisations d'évènements trop stylés ; Mehdi, Ed, Chris et Rémi pour leur groove et le concert de folie ; tous les autres pour la bonne ambiance, les sorties K-fêt et les bons moments partagés : Àngels, Antonio, Barra, Felipe, Fulbert, Ge, Gianluigi, Krist, Laurent, Yu Liang, Liangfen, Loïc, Mat-Pat, Marion, Maxime, Meriem, Mika, Min, Philéas, Raissa, Roberto, Roch, Sandra, Souha, Thibault, Thibaut, Ting, William,... Merci à tous les permanents pour les discussions enrichissantes en acoustique ou pour leur aide administrative. Merci à Patrick Blachier pour la mise en place de la campagne expérimentale. Je suis admiratif devant son efficacité et suis conscient que sans lui je n'aurais pas pu avoir de résultats aussi rapidement. Je voulais également citer Thibault et Charlie du LAUM, avec qui je garde de supers souvenirs de conférence en Croatie et au Mans.

Je voulais également remercier mon coloc Romain, avec qui je garderai un excellent souvenir des soirées ciné, des sorties ou tout simplement de débats autour d'une bonne platrée de carbonara. Merci également à Bono, Clara, Thibaut et Hélène pour les sorties à Lyon et les bonnes réponses du Paddy's. Je salue mes amis de l'ENSTA : les taspammeurs de la promo 2012, Bruno, Baptiste, Matthieu B... Merci également à Ludo d'avoir partagé une passion commune pendant quelques années et d'avoir pu entretenir notre amitié malgré la distance et les différents chemins que l'on a emprunté. Un énorme merci à Butti, Franz, Flo et Matou : en outre des voyages et soirées qu'on a pu se faire, on a su être présents les uns pour les autres dans les moments importants. Enfin, je remercie Tania pour tous les bons moments partagés, pour le réconfort qu'elle sait m'apporter et parce que je sais que j'ai beaucoup de chance de l'avoir rencontré. Mon dernier remerciement va à ma famille et en particulier à mes parents qui m'ont fait confiance et m'ont soutenu pendant toutes ces années d'études.

CONTENTS

LIST OF FIGURES

LIST OF TABLES

ACRONYMS

BEM Boundary Element Method

CAA Circumferential Admittance Approach

CAD Computer Aided Design

CFD Computational Fluid Dynamics

CTF Condensed Transfer Functions

DEA Dynamical Energy Analysis

DOF Degrees Of Freedom

DSF Diffuse Sound Field

FEM Finite Element Method

PTF Patch Transfer Functions

PML Perfectly Matched Layers

PSD Power Spectrum Density

RAM Random Access Memory

SDT Structural Dynamics Toolbox

SEA Statistical Energy Analysis

SmEdA Statistical modal Energy distribution Analysis

TBL Turbulent Boundary Layer

VTCR Variational Theory of Complex Rays

WBM Wave Based Method

NOMENCLATURE

Capital Roman letters

$\mathbb{C}$	Set of complex numbers
E	Young's modulus of the material of the shell
E^*	Complex Young's modulus to account for structural damping
F	Radial force exerted on the shell
$\mathbf{F}^c$	Vector of coupling forces between subsystems
$\mathbf{F}_0$	Vector of external forces
H_W	Transfer function in radial displacement
$H_n^{(1)}$	Hankel function of first kind and order n
$H_n^{(2)}$	Hankel function of second kind and order n
H_p	Transfer function in pressure
J_n	Bessel function of first kind of order n
$\mathbf{K}$	Stiffness matrix
$\mathbf{K}^*$	Complex value of the stiffness matrix to account for structural damping
L	Length of the shell
L_S	Length of a gate function
L_f	Axial force exerted on the shell
L_Γ	Length of the junction Γ
M	Point on the shell or in the fluid domain
M_T	Tangential moment exerted on the shell
M_f	Point in the fluid domain
M_s	Point on the shell
$\mathbf{M}$	Mass matrix
N	Number of condensation functions

N_f	Number of frequencies in the frequency range
$\mathbf{N_k}$	Vector of cutoff wavenumbers
N_m	Truncature for the number of modes
$\tilde{N}$	Number of circumferential orders
$\mathbb{N}$	Set of positive integers
P_{diss}	Dissipated power
P_{ij}	Exchanged power between subsystems i and j
P_{inj}	Injected power
$\mathbf{P}$	Modal basis with residual mode shapes
$\mathbf{Q}$	Orthogonal basis of mode and residual mode shapes
R	Radius of the cylindrical shell
R_T	Reynolds' number
R_{WW}	Inter-correlation function of the radial displacement
R_{int}	Internal radius of the stiffener
$\mathcal{R}$	Distance in the acoustic far-field
$\mathbb{R}$	Set of real numbers
S	Surface of the finite cylindrical shell
S_{WW}	Power spectrum density of the radial displacement
S_{pp}	Power spectrum density of the pressure
$S_{p_b p_b}$	Power spectrum density of the wall pressure
T	Tangential force exerted on the shell
$(T_n)_{n\in\mathbb{N}}$	Chebyshev polynomials
U	Axial displacement of the shell
U_T	Friction velocity
U_c	Convection speed
U_∞	Flow speed
$\mathbf{U}$	Vector of displacements
$\tilde{\mathbf{U}}$	Vector of free displacements

V	Tangential displacement of the shell
W	Radial displacement of the shell
W_a	Radiated power
$< \dot{W} >$	Mean quadratic velocity
$\mathbf{Y}$	Admittance matrix or Condensed Transfer Functions
Z_f	Fluid loading impedance
$\mathbb{Z}$	Set of integers

Lower-case Roman letters

a_p	Side of a square plate
a_n	Modal amplitude
c_0	Sound velocity in the fluid domain
d	Stiffeners spacing
d_s	Distance between the source and the observation point
d_{max}	Maximum distance between two grid points in the axial direction
f	Frequency
f_c	Coincidence frequency
f_{lim}	Upper limit of the frequency domain
f_r	Ring frequency
g	Gravitational force (9.81 m.s^{-2})
h	Thickness of the shell
h'	Corrected thickness
h_W	Impulse response in radial displacement of a system
h_w	Height of the stiffener web
j	Complex value of $\sqrt{-1}$
k_c	Convective wavenumber
k_f	Flexural wavenumber
k_r	Radial wavenumber $\left(k_0^2 - k_x^2\right)^{1/2}$

k_s	Sampling wavenumber
k_x	Axial wavenumber
k_{xf}	Axial flexural wavenumber in the internal plates
k_y	Transversal wavenumber
k_0	Acoustic wavenumber
$\mathbf{k}$	Vector of wavenumbers in different directions of space
l_1	Width of plate 1
l_2	Width of plate 2
n	Circumferential wavenumber
p	Pressure
p_b	Blocked pressure
p_i	Incident pressure
p_{re}	Reradiated pressure
p_s	Scattered pressure
p_0	Amplitude of the incident pressure
q_{exc}	Pressure of a monopole source
r	Radial coordinate
r_s	Radial coordinate of the monopole source
s	Curvilinear abscissa along the coupling line
t	Time
t_f	Thickness of the stiffener flange
t_w	Thickness of the stiffener web
w_f	Width of the stiffener flange
x	Axial coordinate
x_A	Axial coordinate of the section A
x_{exc}	Coordinate of the point force
$\mathbf{x}$	Vector of the space coordinates of a point on the shell
$\mathbf{z}$	Vector of the space coordinates of a point in the fluid

Capital Greek letters

Γ	Coupling line
Δ	Laplacian operator
Δ_f	Bandwidth
Σ_p	Surface excited by a random pressure field
$\mathbf{\Phi}$	Modal basis
$\mathbf{\Psi}$	Matrix of the residual mode shapes
Ω	Acoustic domain

Lower-case Greek letters

δ	Dirac delta distribution
δ_L	Turbulent boundary layer thickness
δk_x	Axial wavenumber resolution
δn	Circumferential order resolution
η	Structural damping coefficient
θ	Cylindrical coordinate
θ_{N+1}	Cylindrical coordinate of the end of the junction
θ_S	Angular length of a gate function
θ_{max}	Maximum angle between two grid points
θ_0	Cylindrical coordinate of the beginning of the junction
λ	Acoustical wavelength
λ_f	Flexural wavelength
ν	Poisson's coefficient of the material of the shell
ν_0	Kinematic viscosity
ξ	Angle to the normal of the cylinder
ρ_s	Density of the material of the shell
ρ_0	Fluid density
σ	Radiation efficiency

τ_w	Shear constraint at the wall
φ	Tangential rotation
φ_n	Condensation function
ϕ_{pp}	Wavenumber-frequency specturm of the wall pressure
ω	Pulsation
ω_n	Eigenfrequency

Symbols and accents

$\langle \bullet, \bullet \rangle$	Scalar product
$\bar{\bullet}$	Free displacement or free condensed displacement
$\check{\bullet}$	Used for differentiating coordinates
$\dot{\bullet}$	Derivative with respect with time
$\ddot{\bullet}$	Double derivative with respect with time
$\hat{\bullet}$	Quantity when the system is excited by a condensation function
$\tilde{\bullet}$	Quantity in the circumferential domain (spatial Fourier transform)
$\tilde{\tilde{\bullet}}$	Quantity in the wavenumber domain (2D Fourier transform)
$\bullet'$	Derivative with respect to the argument
$\underline{\bullet}$ and $\underline{\underline{\bullet}}$	Reduced matrices

INTRODUCTION

Modeling the vibroacoustic behavior of a system is of primarily importance for industrial applications. It is indeed important to be able to design the system prior to the industrialization in order to meet stricter noise and vibration requirements at the lowest cost. Therefore, numerical simulations are nowadays widely used. They allow predicting the noise and vibration of the system before having it produced. The present work focuses on the modeling of cylindrical shells coupled to an infinite fluid domain and with internal structures. They can indeed describe aeronautical or naval systems such as aircraft fuselages or pressure hulls of submarine vehicles, as shown in Fig 1.

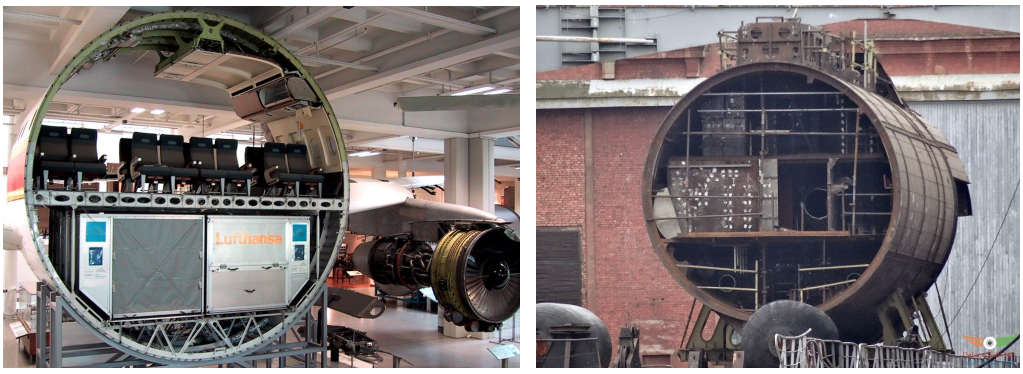

(a) (b)

(c)

Figure 1: (a) Cross-section of an Airbus A300. (b) Cross-section of a submarine pressure hull (Source: defencetalk.net). (c) Underwater mine-hunting drone

The cylindrical shells can be excited by different sources depending on the considered application. They can be divided in three categories:

MECHANICAL EXCITATION: internal mechanisms such as engines or pumps are source of vibrations. Even if they are usually elastically mounted, vibrations can be transmitted to the cylindrical shell. In this work they are modeled by harmonic point forces.

ACOUSTICAL EXCITATION: for aeronautical applications, jets and engines radiate high pressure levels in the near-field of the system. For naval applications, a sonar pulse emitted by another ship can be modeled by a plane wave exciting the cylindrical shell. In the two cases, the pressure at the surface of the cylindrical shell acts as an external force exciting the system.

RANDOM PRESSURE FIELD: when the vehicle is moving in the fluid domain, turbulences induced by the flow may appear near to the surface of the cylindrical shell. Besides, acoustic sources that can be modeled as a reverberant field can appear inside the cylindrical shell. In both cases, the pressure variations are described by random processes and can induce vibrations on the system.

For aeronautical systems, these three kinds of excitation induce interior noise that needs to be controlled for passengers' comfort. For a submarine vehicle, as light and electromagnetic waves cannot propagate easily in water, the vibroacoustic control is of primarily importance. Three main operational capabilities arise from these excitations [1]:

ACOUSTIC STEALTH: the radiated noise of the vehicle in the far-field is mainly due to internal mechanical or acoustical excitations, or to the turbulent flow on the hull. They can be passively detected by a system which is "listening" to the sea with an hydrophone. That noise should thus remain as low as possible.

TARGET STRENGTH: if an active localization sonar is used by a system, the incident acoustic wave induces a scattered pressure field around the vehicle. This scattered pressure can thus be measured, and in some configurations the acoustic signature can show some patterns that can be recognizable. The aim is thus to minimize the scattered field and understand the mechanisms linked to the patterns.

SONAR PERFORMANCES: hydrophone arrays are often mounted on the hull of the vehicle in the form of flank array, in order to detect and localize other vehicles. However, the near-field radiated pressure induced by the turbulences or internal mechanical and acoustical sources can disturb the measures and lower the performances. The near-field radiated pressure should thus be controlled in order to have a high signal-to-noise ratio.

The method developed in this thesis aims at modeling the vibroacoustic behavior of a cylindrical shell taking into account several couplings:

- an infinite fluid domain surrounding the cylindrical shell. The fluid can be light as for air for instance (weak coupling) or heavy as for water (strong coupling).
- axisymmetric stiffeners, which are structures welded along the circumference inside the cylindrical shell. Their role is to stiffen the structure in order to reduce the cylindrical shell thickness and weight, and to withstand hydrostatic pressure when the vehicle is designed for deep waters.
- non-axisymmetric internal frames, such as floors, seatings or engine foundations.

The method should be able to cover a wide frequency range: from some Hz to several kHz for typical industrial applications (*i.e.* radius of several meters and length of several dozens of meters). Besides, the computational cost should remain low enough to be able to run calculations on a basic working station in reasonable time for engineering and optimization purposes. The method should be flexible in order to take into account complex geometries for the internal frames.

Therefore a substructuring approach, called the Condensed Transfer Functions (CTF) method, is proposed in this work. It aims to couple a semi-analytical model of a submerged cylindrical shell with Finite Element models of internal structures. This division of the system provides a tool with great flexibility on the internal geometry, while keeping reasonable calculation cost. The principle of the method is presented in the general case of thin coupled mechanical structures in chapter 2. It is then applied to a submerged cylindrical shell with internal frames for the three types of excitations presented above, *i.e.* mechanical, acoustical and random pressure field in chapter 3, 5 and 6 respectively. The physical phenomena induced by the inclusion of non-axisymmetric

internal frames is discussed in each case. The trends observed through the numerical simulations for a mechanical excitation are checked experimentally on a model in air in chapter 4.

1

LITERATURE REVIEW

This chapter aims at giving an overview of the literature related to the problem considered in the introduction. On one hand, the vibroacoustics of cylindrical shells is discussed, starting from the *in vacuo* case and increasing the complexity step by step by adding stiffeners, heavy fluid loading and by considering different kind of excitations. On the other hand, a review of some substructuring approaches in vibroacoustics is given. A third part presents studies that are at the meeting point between these two topics, in order to study cylindrical shells with non-axisymmetric internal frames. Finally, the originality of the present work is highlighted.

1.1 VIBROACOUSTIC BEHAVIOR OF AXISYMMETRIC CYLINDRICAL SHELLS

1.1.1 *Cylindrical shells in vacuo*

The study of cylindrical shells have been of great interest in the last decades because of their many industrial applications, especially in the aeroacoustic and naval fields. In 1973, Leissa [2] compiles in his book most of the work related to the shells vibrations that has been done so far. In particular, a chapter presents the assumptions and different theories for cylindrical shells. The Flügge theory [3, 4] will be used in this work because of its simplicity and its good agreement with other theories [5, 6]. Let us consider an infinitely long cylindrical shell of radius R and thickness h in a cylindrical coordinate system (x, r, θ), as shown in Fig. 2. The shell is considered as thin, meaning that $R \gg h$. The material is assumed to be elastic and isotropic and is characterized by ρ_s, E and ν, being respectively the density, the Young's modulus and the Poisson's ratio.

U, V and W are respectively the axial, tangential and radial displacements of the shell. L_f, T and F are respectively the axial, tangential and radial point forces, and M_T is the tangential moment exerted on the shell by the external load. In harmonic regime,

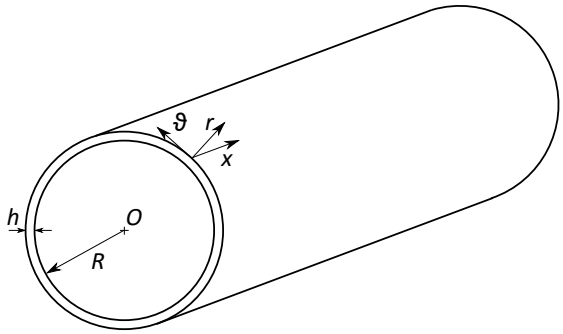

Figure 2: Circular cylindrical shell of radius R and thickness h, and its associated coordinate system.

the time dependence in $e^{j\omega t}$ is omitted, with $j^2 = -1$, ω the pulsation and t the time. The Flügge equations are written as follows:

$$\left(R^2\frac{\partial^2}{\partial x^2} + (1+\beta^2)\frac{1-\nu}{2}\frac{\partial^2}{\partial\theta^2} - \rho_s R^2\frac{1-\nu^2}{E}\frac{\partial^2}{\partial t^2}\right)U + \left(R\frac{1+\nu}{2}\frac{\partial^2}{\partial x\partial\theta}\right)V + \left(R\nu\frac{\partial}{\partial x} - \beta^2R^3\frac{\partial^3}{\partial x^3} + \beta^2R\frac{1-\nu}{2}\frac{\partial^3}{\partial x\partial\theta^2}\right)W = -\frac{\left(1-\nu^2\right)R^2}{Eh}L_f\delta(x)\delta(\theta) \tag{1a}$$

$$\left(R\frac{1+\nu}{2}\frac{\partial^2}{\partial x\partial\theta}\right)U + \left(R^2\left(1+3\beta^2\right)\frac{1-\nu}{2}\frac{\partial^2}{\partial x^2} + \frac{\partial^2}{\partial\theta^2} - \rho_s R^2\frac{1-\nu^2}{E}\frac{\partial^2}{\partial t^2}\right)V + \left(\frac{\partial}{\partial\theta} - \beta^2R^2\frac{3-\nu}{2}\frac{\partial^3}{\partial x^2\partial\theta}\right)W = -\frac{\left(1-\nu^2\right)R^2}{Eh}T\delta(x)\delta(\theta) \tag{1b}$$

$$\left(R\nu\frac{\partial}{\partial x} - \beta^2R^3\frac{\partial^3}{\partial x^3} + \beta^2R\frac{1-\nu}{2}\frac{\partial^3}{\partial x\partial\theta^2}\right)U + \left(\frac{\partial}{\partial\theta} - \beta^2R^2\frac{3-\nu}{2}\frac{\partial^3}{\partial x^2\partial\theta}\right)V + \left(1+\beta^2\left(R^4\frac{\partial^4}{\partial x^4} + 2R^2\frac{\partial^4}{\partial x^2\partial\theta^2} + \frac{\partial^4}{\partial\theta^4}\right) + \rho_s R^2\frac{1-\nu^2}{E}\frac{\partial^2}{\partial t^2} + \beta^2\left(1+2\frac{\partial^2}{\partial\theta^2}\right)\right)W = \frac{\left(1-\nu^2\right)R^2}{Eh}\left(F\delta(x) - M_T\delta'(x)\right)\delta(\theta) \tag{1c}$$

where δ and δ' are the Dirac delta distribution and its derivative, and $\beta = \frac{h}{R\sqrt{12}}$. Structural damping of the shell can be introduced by assigning a complex value with a loss factor η to the elastic modulus of the shell material $E^* = E(1+j\eta)$.

One of the approaches to solve this problem is to write the system of equations in the wavenumber domain [7]. It is achieved by applying a spatial 2D Fourier transform to Eqs. (1a)-(1c). This transform is defined by:

$$f(x,\theta) \mapsto \tilde{\tilde{f}}(k_x,n) = \frac{1}{(2\pi)^2}\int_{\mathbb{R}}\int_{\theta=0}^{2\pi} f(x,\theta)e^{-j(k_x x+n\theta)}\mathrm{d}x\mathrm{d}\theta \tag{2}$$

where k_x is the axial wavenumber and n the circumferential order ($n \in \mathbb{Z}$, because the system is 2π-periodic along the circumferential coordinate). The spectral Flügge equations are thus:

$$\begin{bmatrix} \tilde{\tilde{Z}}_{UU} & \tilde{\tilde{Z}}_{UV} & \tilde{\tilde{Z}}_{UW} \\ \tilde{\tilde{Z}}_{UV} & \tilde{\tilde{Z}}_{VV} & \tilde{\tilde{Z}}_{VW} \\ \tilde{\tilde{Z}}_{UW} & \tilde{\tilde{Z}}_{VW} & \tilde{\tilde{Z}}_{WW} \end{bmatrix} \begin{bmatrix} \tilde{\tilde{U}} \\ \tilde{\tilde{V}} \\ \tilde{\tilde{W}} \end{bmatrix} = \frac{(1-\nu^2)R^2}{Eh} \begin{bmatrix} -\tilde{\tilde{L}}_f \\ -\tilde{\tilde{T}} \\ \tilde{\tilde{F}} + \mathrm{j}k_x \tilde{\tilde{M}}_T \end{bmatrix} \tag{3}$$

with the values of $\tilde{\tilde{Z}}_{UU}$, $\tilde{\tilde{Z}}_{UV}$, $\tilde{\tilde{Z}}_{UW}$, $\tilde{\tilde{Z}}_{VV}$, $\tilde{\tilde{Z}}_{VW}$ and $\tilde{\tilde{Z}}_{WW}$ given in appendix A.1, as well as the expressions for the spectral displacements $\tilde{\tilde{U}}$, $\tilde{\tilde{V}}$ and $\tilde{\tilde{W}}$. The displacements in the phyiscal space are retrieved by applying a 2D inverse Fourier transform to the spectral displacements. The 2D inverse Fourier transform is defined by:

$$\tilde{\tilde{f}}(k_x, n) \mapsto f(x, \theta) = \int_{\mathbb{R}} \int_{\mathbb{R}} \tilde{\tilde{f}}(k_x, n) e^{\mathrm{j}(k_x x + n\theta)} \mathrm{d}k_x \mathrm{d}n \tag{4}$$

The study of the vibrations of the cylindrical shell exhibits a frequency, called the ring frequency f_r, for which the longitudinal wavelength is equal to the circumference. It is defined by the following equation [8]:

$$f_r = \frac{1}{2\pi R} \sqrt{\frac{E}{\rho_s (1-\nu^2)}} \tag{5}$$

To give an order of magnitude, the ring frequency is $f_r = 173$ Hz for a cylindrical shell of radius $R = 5$ m made of steel. At the ring frequency, the radiation efficiency of the cylinder is high [9, 10]. The radiation efficiency of a cylindrical shell is defined by the ratio between the actual far-field radiated power W_a and the power that would be radiated by a cylindrical shell of the same radiating surface S, having an uniform radial velocity V_0:

$$\sigma = \frac{W_a}{\rho_0 c_0 S V_0^2} \tag{6}$$

with ρ_0 the fluid density and c_0 the speed of sound in the fluid. Besides, it can be considered that above the ring frequency, the flexural waves are decoupled from the shear and compressional waves. At higher frequencies, it can be considered that the cylinder behaves like a plate [11]. In this case, the coincidence frequency, for which the acoustic wavenumber $k_0 = \frac{\omega}{c_0}$ is equal to the flexural wavenumber in an equivalent plate of thickness h, can be defined as [8]:

$$f_c = \frac{c_0^2}{2\pi h} \sqrt{\frac{12\rho_s(1-\nu^2)}{E}} \tag{7}$$

It is well known that the radiation efficiency of a structure is low when the frequency is lower than f_c (subsonic domain), reaches a maximum at f_c and tends to 1 above f_c (supersonic domain) [12]. To give an order of magnitude, the coincidence frequency is $f_c = 7602$ Hz for a plate of thickness $h = 30$ mm, made of steel and submerged in water ($c_0 = 1500$ m.s^{-1}). Qatu [13] summarizes more than 600 studies on homogeneous shells done in the 1990's and shows that tremendous work has been done on this topic.

1.1.2 *Stiffened cylindrical shells*

In industrial applications, many systems can be modeled by cylinders reinforced by circumferential stiffeners (also called ribs or rings) as shown in Fig. 3a. The stiffeners are considered axisymmetric (*i.e.* invariant along the circumferential coordinate) and they can have different section profiles, as shown in Fig. 3b. Their role is to stiffen the cylindrical shell, allowing a reduced shell thickness and thus a reduced weight of the structure. For structures designed to be submerged in deep waters, the stiffeners give a better resistance to hydrostatic pressure. Nevertheless, they have an influence on the vibroacoustic behavior of the shell. Galletly [14] presents an analytical solution based on the Lagrange equations to determine the free vibrations of a simply supported ring-stiffened cylindrical shell *in vacuo*. As expected, an increase in the frequency of vibrations can be seen when the structure is stiffened, but Galletly points out that a decrease can be seen on certain geometries. This result has been formerly observed by Arnold and Warburton [15] who concluded that it is caused by the division of the potential energy between bending deformation and deformation of the middle surface. Another approach is proposed by Hoppman [16], where an equivalent orthotropic shell is considered to be analog to a shell having uniform and closely spaced stiffeners. Wah and Hu [17] treat the rings as discrete substructures and determine exactly the inter-ring motions of the shell using the linear shell theory, in the circumferential order space. They show that the inter-ring motion highly depends on the circumferential order, as well as on the rings spacing and on the rings rigidity in comparison with the shell. Beskos and Oates [18] solve the problem in the Laplace transform domain and obtain the response in the time domain by a numerical inversion. Al-Najafi and Warburton [19] use an axisymmetric Finite Element model to calculate the eigenmodes and eigenfre-

quencies of a finite stiffened cylindrical shell. The FEM consists in solving the partial differential equations by using the variational formulation of the local equations. The latter are discretized into elements where interpolation functions are defined and make the link between the nodes on the mesh [20] (more details are given in section 1.2.1). More especially, Al-Najafi and Warburton examine the influence of the number and size of stiffeners on the vibroacoustic behavior of the cylindrical shell.

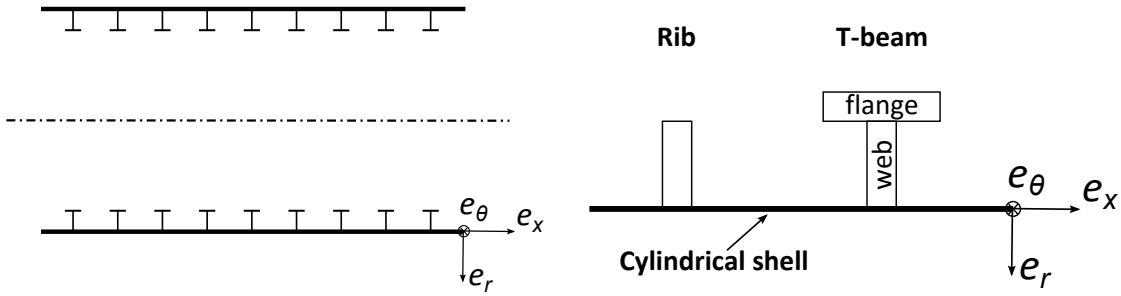

(a) (b)

Figure 3: (a) Section of a stiffened circular shell and its coordinate system in the plane $\theta = 0$. (b) Examples of stiffeners cross-sections and associated vocabulary.

1.1.3 *Heavy fluid loading*

In order to study the vibroacoustic behavior of submerged structures, heavy fluid loading is taken into account. The coupling with a heavy fluid can be represented by adding a reacting pressure term p in the right-hand side of the shell equation of movement governing the radial component (*i.e.* in Eq. (1c)):

$$\left(R\nu\frac{\partial}{\partial x} - \beta^2 R^3\frac{\partial^3}{\partial x^3} + \beta^2 R\frac{1-\nu}{2}\frac{\partial^3}{\partial x\partial\theta^2}\right)U + \left(\frac{\partial}{\partial\theta} - \beta^2 R^2\frac{3-\nu}{2}\frac{\partial^3}{\partial x^2\partial\theta}\right)V$$
$$+\left(1+\beta^2\left(R^4\frac{\partial^4}{\partial x^4} + 2R^2\frac{\partial^4}{\partial x^2\partial\theta^2} + \frac{\partial^4}{\partial\theta^4}\right) + \rho_s R^2\frac{1-\nu^2}{E}\frac{\partial^2}{\partial t^2} + \beta^2\left(1+2\frac{\partial^2}{\partial\theta^2}\right)\right)W$$
$$= \frac{\left(1-\nu^2\right)R^2}{Eh}\left(F\delta(x)\delta(\theta) - M_T\delta'(x)\delta(\theta) - p\right) \quad (8)$$

The first two equations of motion Eqs. (1a) and (1b) remain unaltered from their *in vacuo* form. The pressure satisfies the homogeneous Helmholtz equation in the external fluid domain:

$$\Delta p(x,r,\theta) + k_0^2 p(x,r,\theta) = 0 \quad (9)$$

where in cylindrical coordinates, the Laplacian operator is $\Delta = (\partial^2/\partial x^2) + (\partial^2/\partial r^2) + 1/r(\partial/\partial r) + 1/r^2(\partial^2/\partial\theta^2)$. The pressure also satisfies the Sommerfeld radiation condition and Euler's relation at the interface with the shell:

$$\begin{cases} p(x,r,\theta) & = 0 \quad \text{when } r \to \infty \\ \dfrac{\partial p}{\partial r}(x,R,\theta) & = \rho_0 \ddot{W}(x,\theta) \end{cases} \tag{10}$$

The problem of Eqs. (9)-(10) can be solved in the wavenumber domain, as presented in details by Junger and Feit [8]. The spectral pressure at the interface is then linked to the spectral radial velocity thanks to an impendance term $\tilde{\tilde{Z}}_f$:

$$\tilde{\tilde{p}} = \tilde{\tilde{Z}}_f \tilde{\tilde{W}} \tag{11}$$

with

$$\tilde{\tilde{Z}}_f = \frac{\rho_0 \omega^2}{k_r} \frac{H_n^{(2)}(k_r R)}{H_n^{(2)'}(k_r R)} \tag{12}$$

$k_r = \left(k_0^2 - k_x^2\right)^{1/2}$ and $H_n^{(2)}$ and $H_n^{(2)'}$ are respectively the Hankel functions of the second kind and order n and their derivatives with respect to the argument. Eq. (11) can be injected into the Flügge spectral equation with the pressure term on the right hand side and yields a solvable linear equation system. The solution is derived by Maxit and Ginoux [21] and given in appendix A.2. The circumferential pressure $\tilde{p}$ for a point (x,r) can be written by applying an inverse Fourier transform along the axial wavenumber:

$$\tilde{p}(x,r,n) = \int_{-\infty}^{+\infty} \frac{\rho_0 \omega^2}{k_r} \frac{H_n^{(2)}(k_r r)}{H_n^{(2)'}(k_r R)} \tilde{\tilde{W}}(k_x,n) e^{\mathrm{j}k_x x} \mathrm{d}k_x \tag{13}$$

For $\mathcal{R}$ in the acoustic far-field, *i.e.* $\mathcal{R} \gg \frac{2\pi}{k_0}$, the asymptotic expression for the Hankel function and the stationary phase theorem can be used [8]. If ξ is the angle from the point with the normal axis and θ is the circumferential angle, the far-field pressure p can be written as:

$$p(\mathcal{R},\xi,\theta) = \sum_{n=-\infty}^{+\infty} \frac{2\mathrm{j}\rho_0 \omega^2}{\mathcal{R} k_0 \cos\xi} \frac{\tilde{\tilde{W}}(-k_0 \sin\xi, n)}{H_n^{(2)'}(R k_0 \cos\xi)} e^{-\mathrm{j}\mathcal{R}k_0 + \mathrm{j}n(\theta + \frac{\pi}{2})} \tag{14}$$

Photiadis [22] uses this approach for the case of an infinite cylinder excited by a ring drive. Burroughs [23] adds doubly periodic ring supports that interact with the shell through normal forces only and calculate the far-field pressure radiated by the system

excited by a point force. He points out that the radiation from the shell appears like an array of radiators located at the ring supports. His study is investigated further by considering different excitations [24].

The impedance term $\tilde{\tilde{Z}}_f$ can be decomposed into its real and imaginary parts, respectively called resistance and reactance. The resistance represents energy dissipation through acoustic radiation, while the reactance describes the added mass effect. Because of the orthogonality of the $\cos(n\theta)$ functions, there is no coupling between modes of different circumferential orders [25]. For the case of a baffled finite cylindrical shell (*i.e.* a finite cylindrical shell embodied in an infinitely long and rigid cylinder), explicit expressions for the modal amplitude cannot always be determined and numerical integration is required, as for example in a study by Sandman [26]. Sandman also shows that the baffle has a weak influence on the radiation of finite cylindrical shells due to radial vibrations.

Laulagnet and Guyader [27] use the *in vacuo* modes basis and the calculation of the radiation impedance to determine the radiated power by a submerged finite cylindrical shell. Stiffeners with cross-sections like those encountered in the industry are added to the structure [28], and results show that they have strong influence on the quadratic velocity of the submerged cylindrical shell and a smaller influence on power radiated below the ring frequency. The same configuration is studied using a spectral approach, which means that the equations are derived in the axial and circumferential wavenumbers domain [29, 30]. Caresta and Kessissoglou [31] study the influence of ring-stiffeners, bulkheads and fluid loading on the vibroacoustic response of a finite cylindrical shell. Their aim is to model at low frequencies the response of a submarine hull excited by the propeller-shafting system. The ring-stiffeners are modeled using a smeared theory. Their effect is to increase inertia for the low circumferential orders, to reduce the displacements for the $n = 0$ mode, and to increase rigidity at higher circumferential orders. In further studies [32, 33], they consider a cylindrical shell with conical ends instead of a baffled cylinder. The structural response is calculated using shell equations and use the Boundary Element Method (BEM) to determine the far-field radiated sound pressured. The BEM consists in deriving the Helmholtz integral on a discretization of the radiating surface of the structure and is particularly well-suited to radiation problem in infinite domains. The influence of the endings is thus highlighted.

They propose to isolate the end caps with passive rubber mounts, to avoid the axial fluctuations of the shafting system to propagate on the main hull and to reduce the sound pressure radiated [34]. Qu *et al.*[35] present a modified variational method to analyze the vibroacoustic behavior of a stiffened shell with spherical ends and a spectral Helmholtz integral formulation is taken to model the exterior fluid. A coupled Finite Element Method/ Boundary Element Method (FEM/BEM) is used at low frequencies to calculate the response of a submarine hull due to the propeller forces and its reduction through a resonance changer [36, 37]. The main problem of this approach is that it has usually high computational cost, and Peters *et al.* propose therefore the use of reduced models [38]. The BEM can also be used to calculate the impedance due to the fluid loading and use it as an input of a Finite Element model [39]. Alternatively, the fluid can be discretized by FEM on a domain delimited by Perfectly Matched Layers (PML) [40]. The PML is a technique used to model a free-space domain by suppressing the reflections on the boundaries [41]. It is based on the definition of theoretic absorbing layers where there is no reflection at the boundary with the fluid domain, and where the amplitude of propagating acoustic wave decreases exponentially.

1.1.4 *Scattering from submerged cylindrical shells*

The scattering from a shell immersed in a heavy fluid and impinged by an acoustic plane wave has been extensively studied in the past. In addition to the specular reflection of the incident wave, the elastic shell vibrates and re-radiates noise. The far-field scattered pressure shows typical patterns in the frequency-angle spectrum due to structural wave propagation and geometric diffraction. Compressional and shear waves that propagate helicoidally on the surface of the cylinder are highlighted using the elastic theory on infinite shells [42, 43] or on simply supported finite shells [44]. Helical propagation is also identified on experimental data [45]. The influence of evenly spaced ribs was first investigated experimentally [46, 47, 48]. Two scattering phenomena are observed: the Bragg scattering, which is due to the interferences between the geometrical reflections of the incident plane wave on the ribs, and the Bloch-Floquet scattering which is due to the subsonic flexural waves that propagate along the shell and interact with the internal frames. These scattering phenomena are illustrated in Fig. 4 [48].

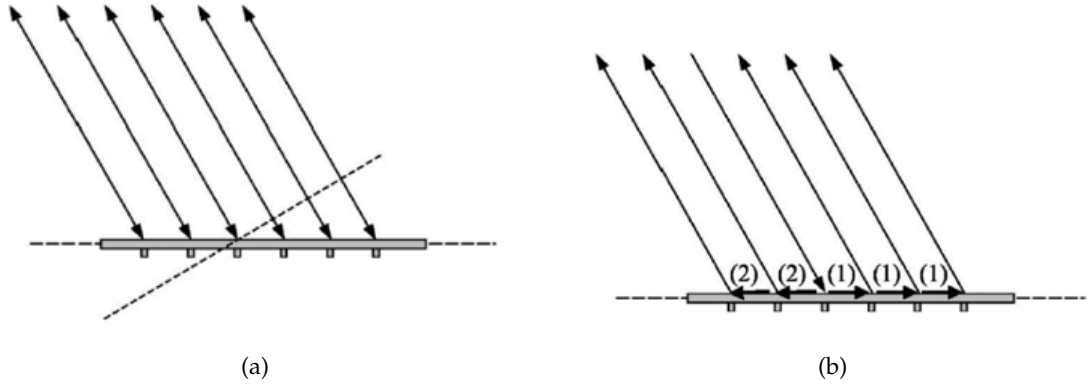

(a) (b)

Figure 4: Illustration of the scattering phenomena. (a) Bragg scattering. (b) Scattering from Bloch-Floquet waves [(1) forward BF, (2) backward BF].

Tran-Van-Nhieu [49] derives the problem analytically on a simply supported slender cylindrical shell, taking into account only the normal component of the reacting forces applied by the stiffeners to the shell. Guo [50] distinguishes geometric and dynamic effects of an internal plate loading on an infinitely long cylinder, showing that resonances of the internal structure may affect greatly the scattered field. A similar 2D problem is analytically derived by Klauson and Metsaveer [51] and they point out that lengthwise ribs and walls affect the circumferential waves. A lengthwise reinforced shell has been studied using elasticity theory at very high frequencies, where the shell theory is not valid because the wavelengths in the fluid and in the structure are smaller than the shell thickness [52, 53]. The inclusion of bulkheads is investigated in several studies [54, 55, 56] which show that the coupling has an influence on the scattered pressure field. A quadrant symmetric arrangement of rods connected to the ring stiffeners through rubber blocks is considered by Park [57] and he shows that the internal structures can store energy and lengthen the decay rate of an impulse response. Pan *et al.* [58] describe the scattering from a finite cylindrical shell loaded by sets of stiffeners and bulkheads with two different spacings.

Experimental and numerical work are conducted to evaluate the effect of an increasing structural complexity of the submerged cylindrical shells: irregularly spaced ribs are considered [59, 60], internal degrees of freedom are added through resonators [61]. The theoretical formulations for these problems is given by Tran-Van-Nhieu [62]. Several conclusions can be drawn from these studies. First the rib spacing irregularity has

mainly an influence on the near-field pressure, but can also modify the Bloch-Floquet and Bragg phenomena. Then, as mentioned by Soize [63] or Piece [64], it is shown that the internal fuzzy structures give rise to an apparent damping effect.

1.1.5 *Ribbed structures excited by random excitations*

In some applications, cylindrical shells can be subject to random pressure fields such as Diffuse Sound Field (DSF) or Turbulent Boundary Layer (TBL). These excitations yield vibrations, which knowledge is of primarily importance in practice. An extensive amount of studies is available in the literature for the characterization of the excitation and the determination of the vibroacoustic behavior of structures excited by a TBL [65, 66, 67]. As the excitation is a random process, the classical approach consists in determining the second order moments of the physical values. More particularly the Power Spectrum Density (PSD) of the displacement S_{WW} and the PSD of the pressure S_{pp} are determined.

Let us consider a vibroacoustic system made of a structure coupled to a fluid domain. The surface Σ_p is excited by a random pressure field (*i.e.* TBL or DSF). The wall pressure $p_b(\check{\mathbf{x}}, t)$ is expressed at a location $\check{\mathbf{x}} \in \Sigma_p$ as a function of the time t. The system is supposed to be linear and invariant in time, so that the displacement W at a point $\mathbf{x}$ can be expressed as:

$$W(\mathbf{x}, t) = \int_{\Sigma_p} \int_{-\infty}^{+\infty} h_W\left(\mathbf{x}, \check{\mathbf{x}}, t - \tilde{\tau}\right) p_b\left(\check{\mathbf{x}}, \tilde{\tau}\right) \mathrm{d}\tilde{\tau}\mathrm{d}\check{\mathbf{x}} \tag{15}$$

where $h_W\left(\mathbf{x}, \check{\mathbf{x}}, t\right)$ is the impulse response of the system at point $\mathbf{x}$ when excited by an impulse unitary force at point $\check{\mathbf{x}}$. Considering that the random process is ergodic, the inter-correlation function $R_{WW}(\mathbf{x}, \mathbf{x}', t)$ is defined as:

$$R_{WW}(\mathbf{x}, \mathbf{x}', t) = \int_{-\infty}^{+\infty} W(\mathbf{x}, \tau) W(\mathbf{x}', t + \tau) \mathrm{d}\tau \tag{16}$$

Injecting Eq. (15) into Eq. (16) and applying a Fourier transform in the time domain yields the space-frequency spectrum $S_{WW}(\mathbf{x}, \mathbf{x}', f)$ [68]:

$$S_{WW}(\mathbf{x}, \mathbf{x}', f) = \int_{\Sigma_p} \int_{\Sigma_p} H_W^*\left(\mathbf{x}, \check{\mathbf{x}}, f\right) S_{p_b p_b}\left(\check{\mathbf{x}}, \check{\check{\mathbf{x}}}, f\right) H_W\left(\mathbf{x}', \check{\check{\mathbf{x}}}, f\right) \mathrm{d}\check{\mathbf{x}}\mathrm{d}\check{\check{\mathbf{x}}} \tag{17}$$

where $H_W\left(\mathbf{x}, \check{\mathbf{x}}, f\right)$ is the transfer function in displacement of point $\mathbf{x}$ when excited at point $\check{\mathbf{x}}$, $S_{p_b p_b}\left(\check{\mathbf{x}}, \check{\check{\mathbf{x}}}, f\right)$ is the space-frequency spectrum of the wall pressure, and *

denotes the conjugate. Similarly, the PSD for the radiated pressure $S_{pp}(\mathbf{z}, \mathbf{x}', f)$ at the location $\mathbf{z}$ is:

$$S_{pp}(\mathbf{z}, \mathbf{z}', f) = \int_{\Sigma_p} \int_{\Sigma_p} H_p^* (\mathbf{z}, \check{\mathbf{x}}, f) \, S_{p_b p_b} (\check{\mathbf{x}}, \check{\check{\mathbf{x}}}, f) \, H_p (\mathbf{z}', \check{\check{\mathbf{x}}}, f) \, \mathrm{d}\check{\mathbf{x}} \mathrm{d}\check{\check{\mathbf{x}}} \tag{18}$$

where $H_p (\mathbf{z}, \check{\mathbf{x}}, f)$ is the transfer function of the radiated pressure at point $\mathbf{z}$ when excited at point $\check{\mathbf{x}}$.

A few studies, summarized by Blake [66], propose models for $S_{p_b p_b}$ for the case of a cylinder excited by a TBL. Willmarth *et al.* can for example be cited for their experimental work and the comparison with planar structures [69, 70]. They point out that for the case where the ratio of the TBL thickness to the radius of the cylinder is large, there is a poor agreement between the measurements on a cylinder and models for a plate. Nevertheless, when the TBL thickness is small compared with the radius of curvature of the system, which is the case in aeronautical and naval applications, the TBL can be considered as a planar one [71]. This is why classical models developed for plates are used in this case, as for instance Corcos' [72] or Chase's [73], writing that the transversal wavenumber k_y is linked to the circumferential order n by $k_y = \frac{n}{R}$. For a DSF inside the cylindrical shell, models for planar surfaces are used [74, 75, 76].

The excitation being characterized by $S_{p_b p_b}$, the main challenge lies in the calculation of the transfer functions H_W and H_p. Strawderman [77] reviews the first existing models of finite and infinite plates. He points out that none of the models fully agrees with experimental results but that the ones for the finite plate performs better. Birgersson *et al.* [78] show numerical results on a plate using the spectral FEM. The complexity of the problem is successively increased by taking into account heavy fluid loading [79] or by stiffening the plates [80]. Some authors apply a 2D Fourier transform to Eqs. (17) and (18) to avoid calculating transfer functions between any couple of points on the structure [81, 82, 83]. The 2D Fourier transform of the transfer functions are called the sensitivity functions. Maxit and Denis [84] use the reciprocity principle to estimate the sensitivity function at a point M from the vibratory field induced by a point excitation at M. An application to a ribbed plate with heavy fluid loading is proposed and highlights the apparition of Bloch-Floquet waves.

1.2 SUBSTRUCTURING METHODS IN VIBROACOUSTICS

In this section, we focus on substructuring approaches to model the vibroacoustic behavior of complex mechanical systems on a wide frequency range. Indeed in this case numerical element-based models are not always adapted, mainly because of computational cost. Therefore, the idea is to divide a system into several subsystems that can be studied easily when they are isolated. These methods are called substructuring methods and are widely used for industrial applications. Some of these methods are presented in this section.

1.2.1 *Modal synthesis*

1.2.1.1 *The Finite Element Method (FEM)*

Nowadays, one of the most common way to predict numerically the vibroacoustic behavior of a system in the low frequency range is to use the Finite Element Method (FEM). It consists in solving the partial differential equations by using the variational formulation of the local equations. The latter are discretized into elements where interpolation functions are defined and make the link between the nodes on the mesh [20]. The mass and stiffness matrices, respectively noted $\mathbf{M}$ and $\mathbf{K}$ are defined and the problem can thus be expressed as a linear equations system at an angular frequency ω:

$$(-\omega^2\mathbf{M} + \mathbf{K}^*)\mathbf{U} = \mathbf{F}_0 \tag{19}$$

where $\mathbf{F}_0$ is the vector of external forces and $\mathbf{U}$ the vector of the unknown displacements at the nodes. Structural damping η is introduced using a complex stiffness value $\mathbf{K}^* = \mathbf{K}(1 + j\eta)$. The system given by Eq. (19) can be solved by different approaches:

DIRECT CALCULATION: The dynamic stiffness matrix $(-\omega^2\mathbf{M} + \mathbf{K}^*)$ is inverted to yield the displacements:

$$\mathbf{U} = (-\omega^2\mathbf{M} + \mathbf{K}^*)^{-1}\mathbf{F}_0 \tag{20}$$

The direct calculation gives accurate results but is time consuming. It can thus become prohibitive, in particular for industrial applications where systems can have millions of Degrees Of Freedom (DOF).

MODAL SUPERPOSITION: In order to reduce the number of DOF, the problem of Eq. (19) is solved on a reduced basis. One of the most common approach is to use the moda basis of the system. They are calculated by solving the eigenvalue problem of the conservative dynamic system:

$$\omega_n^2 \mathbf{M}\boldsymbol{\Phi}_n = \mathbf{K}\boldsymbol{\Phi}_n \tag{21}$$

Physically speaking, ω_n represent the eigenfrequencies of the system while $\boldsymbol{\Phi}_n$ are the associated mode shapes. The basis is theoretically of infinite dimension but for obvious practical reasons it must be truncated to an integer N_m. The frequency response can then be written as a linear combination of these modes:

$$\mathbf{U} = \sum_{n=1}^{N_m} a_n \boldsymbol{\Phi}_n \tag{22}$$

where a_n is called the modal amplitude and is calculated from the reduced mass and stiffness matrices, $\underline{\mathbf{M}} = \boldsymbol{\Phi}^{\mathrm{T}}\mathbf{M}\boldsymbol{\Phi}$ and $\underline{\mathbf{K}} = \boldsymbol{\Phi}^{\mathrm{T}}\mathbf{K}\boldsymbol{\Phi}$ and the reduced force $\underline{\mathbf{F}} = \boldsymbol{\Phi}^{\mathrm{T}}\mathbf{F}_0$:

$$a_n = (\underline{\mathbf{K}}^* - \omega^2 \underline{\mathbf{M}})^{-1}\underline{\mathbf{F}} \tag{23}$$

The damping can be introduced in the reduced stiffness matrix: $\underline{\mathbf{K}}^* = \underline{\mathbf{K}}(1 + \mathrm{j}\eta)$. Compared to the direct calculation, this method is much faster but has a poor convergence in some frequency bands (*i.e.* outside of resonance peaks), because of the basis truncation.

To illustrate the basis truncation, the modal amplitudes of 3 modes are plotted as a function of the frequency in Fig. 5 for an arbitrary mechanical system (a ring stiffener excited by a radial point force). It can be seen that the contribution of the modes tends towards a non-null constant value when $f \to 0$.Thus, neglecting higher modes can lead to errors at low frequency, even if their peaks are out of the frequency range.

MODAL SUPERPOSITION + RESIDUAL MODES: The residual mode shapes technique [85, 86, 87] consists in adding particular solutions in order to compensate for the basis truncation. A quasi-static mode shape $\boldsymbol{\Psi}$ (*i.e.* a particular response at a very low frequency ω_0) is calculated as follows:

$$\boldsymbol{\Psi} = (\mathbf{K} - \omega_0^2 \mathbf{M})^{-1}\mathbf{F}_0 \tag{24}$$

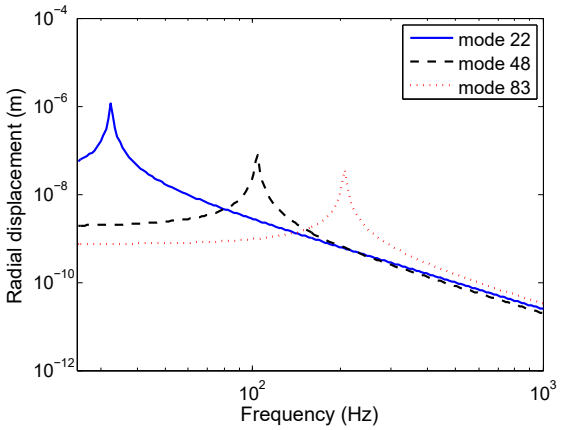

Figure 5: Modal amplitudes for 3 modes of a ring stiffener excited by a unitary radial point force.

It is added to the modal basis to define a new basis $\mathbf{P} = \{\mathbf{\Phi}_n \ \mathbf{\Psi}\}$ and to compensate for the effect of the truncation. It is worth noting that the basis $\mathbf{P}$ is generally not orthogonal and needs to be diagonalized. To do so, the following eigenvalue problem is solved:

$$\left(\underline{\mathbf{K}} - \omega_n^2 \underline{\mathbf{M}}\right) \mathbf{Q} = 0 \tag{25}$$

with $\underline{\mathbf{M}} = \mathbf{P}^{\mathrm{T}}\mathbf{M}\mathbf{P}$ and $\underline{\mathbf{K}} = \mathbf{P}^{\mathrm{T}}\mathbf{K}\mathbf{P}$. As $\left(\underline{\mathbf{K}} - \omega_n^2 \underline{\mathbf{M}}\right)$ is a positive semi-definite matrix, the eigenvectors $\mathbf{Q}$ are orthogonal. One defines new reduced mass and stiffness matrices:

$$\begin{cases} \underline{\underline{\mathbf{M}}} &= \mathbf{Q}^{\mathrm{T}}\underline{\mathbf{M}}\mathbf{Q} \\ \underline{\underline{\mathbf{K}}} &= \mathbf{Q}^{\mathrm{T}}\underline{\mathbf{K}}\mathbf{Q} \end{cases} \tag{26}$$

along with a new reduced force vector $\underline{\underline{\mathbf{F}}} = \mathbf{Q}^{\mathrm{T}}\mathbf{P}^{\mathrm{T}}\mathbf{F}_0$. Introducing again damping in the reduced stiffness matrix, one deduces the displacement using the following equations:

$$\mathbf{U} = \sum_{n=1}^{N_m} a_n (\mathbf{P}\mathbf{Q})_n \tag{27}$$

with

$$a_n = (\underline{\underline{\mathbf{K}}}^* - \omega^2 \underline{\underline{\mathbf{M}}})^{-1} \underline{\underline{\mathbf{F}}} \tag{28}$$

Comparing to the previous alternative, the convergence is greatly improved and the calculation time remains low.

However, as the mesh resolution is generally determined by a criterion based on the smallest wavelength (usually 6 or 10 elements per wavelength), the higher the frequency, the more computational effort is needed to solve the problem. That is why substructuring methods are considered here. Indeed, these methods allow dividing the system into components that are easier to study separately from a computational point of view. Besides, some substructuring methods have an interest from the industrial point of view, as the subsystems can be characterized independently by different means (numerical, analytical, experimental ...).

1.2.1.2 *Dividing the system into components*

The modal synthesis appeared in the 1960's to deal with large structures by dividing it into substructures or components described by their eigenmodes. Hurty [88] is one of the first to introduce the method under the name of component mode synthesis. At this early stage, the main problem of this method is that the modal basis, theoretically infinite, needs to be truncated for practical reasons, leading to convergence issues. To tackle this issue, different conditions are introduced at the interfaces, and it is possible to divide them into 4 main categories [20, 89]:

FIXED INTERFACES METHODS: the most widespread being probably the Craig-Bampton method [90]. For each subsystem, it consists in dividing the basis into constraint or attachment modes, and fixed constraint normal modes. The constraint modes are calculated by imposing a unitary displacement on one of the DOF at the interface, all the other DOF at the interface being fixed. The fixed constraint normal modes are the normal modes of the subsystem with fixed interfaces.

COMPONENT MODE SUBSTITUTION: it is particularly adapted to structures consisting of a main structure linked to secondary structures called branches. These methods, first developed by Gladwell [91] and then by Benfield and Hruda [92] can have fixed or free interfaces for the main structure and fixed interfaces for the branches.

FREE INTERFACES METHODS: the normal mode shapes and the natural frequencies of the subsystems with free interfaces can be used [93, 94], but have usually poor convergence. Nevertheless, it can be largely improved by using residual flexibility

components to take into account the static effect of the truncated modes. Shyu *et al.* [95] use quasi-static modes to compensate for the modal truncature and show that the convergence is greatly improved. Tournour *et al.* [96] study the convergence of the method and propose criteria on the number of modes. More recently, Rixen [97] proposes an alternative free interface approach using interface forces, being the dual of the classical Craig-Bampton approach.

HYBRID METHODS: as the one presented by MacNeal [98], some methods allow combining free and fixed interfaces. The main advantages of these methods is first that from a practical point of view it is not always possible to choose the boundary conditions at the interface for the uncoupled subsystems. Second is that the accuracy can be improved by adding static modes when the interface is fixed. Hale and Meirovitch [99, 100] can for example be cited for using a basis of admissible functions instead of the modal basis, which is usually more flexible.

1.2.2 *Substructuring approaches at mid and high frequencies*

The element based methods presented in the previous section cannot be used at mid and high frequencies for industrial applications for two main reasons. First, as mentioned previously, the computational cost can be prohibitive for large systems with several millions of DOF. Second, the systems are very sensitive to the input parameters, meaning that a slight change in one parameter can induce large dispersion in the response [101, 102]. Therefore, global methods based on the energy analysis are developed. The Statistical Energy Analysis (SEA) [103, 104, 105] is a statistical theory of sound and vibration when the number of modes is large and vibration is sufficiently disorganized. The SEA requires that the energy is equally distributed between the modes and that the internal dissipation is not too high [106]. The system is divided into several subsystems and the energy balance for each subsystem reads:

$$P_{inj,i} = P_{diss,i} + \sum_{i \neq j} P_{ij} \tag{29}$$

where $P_{inj,i}$ is the injected power in subsystem i. $P_{diss,i}$ is the dissipated power in subsystem i and is proportional to damping. P_{ij} is the exchanged power between subsystems i and j and is proportional to the difference of energy between the two sub-

systems through a coupling loss factor. In the Statistical modal Energy distribution Analysis (SmEdA), the modal energy equipartition assumption is relaxed to extend the validity of the method to mid frequencies [107, 108, 109, 110]. The energy balance stated in Eq. (29) is written to describe the energy exchanges between modes, rather than between subsystems.

Hybrid methods allow coupling any combination of deterministic methods (FEM, BEM) to SEA [111, 112, 113, 114, 115]. The coupling is based on the expression of fields as a sum of direct and reverberant fields.

The Dynamical Energy Analysis (DEA) is based on ray tracing to follow the energy flows in a structure [116, 117]. The ray dynamics depends on linear operators expressed on a basis at the boundaries.

Methods such as the Wave Based Method (WBM) [118, 119] or the Variational Theory of Complex Rays (VTCR) [120, 121, 122] belong to the family of Trefftz approaches. They can be used in mid frequencies and have good efficieny. The field variables are approximated by expansions of globally defined, exact solutions. The system is divided into convex subdomains on which a set of wave functions is chosen to solve the differential equations.

1.2.3 *The admittance approach*

The admittance method in structural dynamics is a powerful tool to subdivide structures. It is based on the mechanical continuity equations and has thus no frequency limitations. Gardonio and Brennan [123] present the origins and the development of the method, and explain that the admittance method is inspired by the laws used in the field of electricity, and was transcripted first by Firestone [124]. Hixson [125] dedicates a chapter of his book and gives examples of simple application cases. In order to investigate multiple point and multiple DOF vibration transmission, Rubin [126] introduces matrix notation. It is often used for point coupling but no clear formalism can be found in the literature. Therefore, the method is described in chapter 2. The admittance method is extended for structural-acoustic systems, for the case of weak coupling, by Kim and Brennan [127].

The mechanical admittance represents the ease of motion of a structure when subjected to harmonic point force, as illustrated in Fig. 6. For general 3-D problems, $\mathbf{U}_n^\alpha = \left[U_{n,p}^\alpha\right]_{1\leq p\leq 6}$ is the vector of the 3 translations and 3 rotations of space at the point n and $\mathbf{F}_m^\alpha = \left[F_{m,q}^\alpha\right]_{1\leq q\leq 6}$ the vector of the 3 forces and 3 moments applied at the point m. The admittance $\mathbf{Y}_{nm}^\alpha$ of a subsystem α is defined as the ratio of the displacement to the force [125]:

$$\mathbf{Y}_{nm}^\alpha = \left[\frac{U_{n,p}^\alpha}{F_{m,q}^\alpha}\right]_{1\leq p\leq 6, 1\leq q\leq 6}. \tag{30}$$

For two coupling points (n, m), the admittance $\mathbf{Y}_{nm}^\alpha$ is thus a 6×6 matrix to account for all the DOF. To link different points and different DOF, the admittance is written as a matrix [126], and 4 different types of admittances can be distinguished:

POINT OR SELF ADMITTANCE: relates a displacement and a force at the same point and on the same DOF ($n = m$ and $p = q$). It is the diagonal terms of the admittance matrix [128].

CROSS ADMITTANCE: relates a displacement and a force at the same point but on different DOF ($n = m$ and $p \neq q$). It is the extra-diagonal terms of the diagonal blocks of the admittance matrix.

TRANSFER ADMITTANCE: relates a displacement and a force at two different points but on the same DOF ($n \neq m$ and $p = q$). It is the diagonal terms of the extra-diagonal blocks of the admittance matrix.

TRANSFERRED CROSS ADMITTANCE: relates a displacement and a force at two different points and on two different DOF ($n \neq m$ and $p \neq q$). It is the extra-diagonal terms of the extra-diagonal blocks of the admittance matrix.

In literature, the mobility term, which is the ratio of the velocity to the force, or impedance, which is the inverse of the mobility can be found. In the harmonic regime at the angular frequency ω, the mobility is linked to the admittance by multiplying by $j\omega$. In the following, it is thus equivalent to use the mobility or the admittance and the latter is preferably used. When dealing with measurements on real structures, the admittance is evaluated by measuring the displacements of the structure with free boundary conditions in response to a known harmonic excitation. On the contrary,

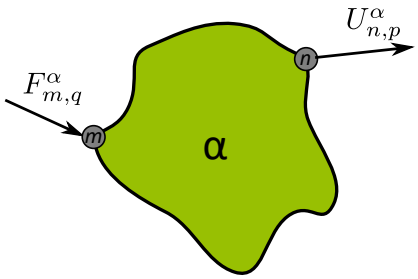

Figure 6: Displacement in n of the system α when excited by a point force in m.

the impedance is evaluated by blocking the displacements and measuring the efforts induced by a displacement imposed at a point. It is thus important to note that the two quantities do not follow the same approach and the admittance has the advantage of being estimated more easily for a mechanical structure [129].

One of the main advantage of the admittance is that it can describe the dynamic behavior of a subsystem at the interfaces with other subsystems. Petersson and Plunt [130, 131] are the first to define the concept of effective mobility, to determine if some of the extra-diagonal terms of the admittance matrix can be neglected in some cases, and can thus reduce the size of the system and improve the conditioning of the matrix. The particular case of two perpendicular plates is studied [132, 133], in order to propose an approximation method for the mobility at the intersection. Mondot and Petersson [134] define what is the source descriptor based on the mobility and which allows comparing vibratory sources independently from the receiver structure. If the receiver mobility is known, it is possible to describe the coupling between the source and the receiver. This approach leads to the study of more complex systems, where there are more coupling points and directions of excitations [135, 136]. One of the results is that the point admittance mainly depends on the geometry close to the contact, while the transfer admittance depends mainly on the structural properties between the two points.

The admittance method has been applied to couple cylindrical shells with internal structures. Wilken and Soedel [137, 138] calculate the vibroacoustic behavior of an axisymmetric cylindrical shell coupled to stiffeners. El Raheb and Wagner [139] propose a method to couple a cylindrical shell to an acoustic domain and to internal structures that are described analytically using their impedances. Nevertheless, they only apply the method to a shell without internal structures. Huang and Soedel [140, 141, 142]

study the free and forced vibrations of a cylindrical shell coupled to one or several circular plates. More recently, Chen *et al.* [143] used the admittance method to analyze a finite cylindrical shell with a conical and a spherical end.

1.2.4 *The Patch Transfer Functions (PTF) method*

As an extension of the admittance approach, Ouisse *et al.* [144] present a substructuring method to solve linear vibroacoustic problems. They divide the system into several subsystems coupled along surfaces. These surfaces, that are defined either at the interface between a structure and a fluid domain or at the interface between two fluid domains, are divided into patches. The Patch Transfer Functions (PTF) method, as it is called, consists in calculating averaged transfer functions on these patches for the uncoupled subsystems and use the admittance approach to determine the behavior of the coupled system. A convergence criterion on the patches size yields an optimum for half of a wavelength. Validation on two coupled acoustic cavities is given before applying the method on examples taken from the automotive industry. Chazot and Guyader [145] use the method to estimate the transmission loss through double panels. Aucejo *et al.* [146] focus on the coupling with heavy-fluid and improve the convergence of the method by introducing residual mode shapes in the PTF calculations. Maxit *et al.* [147] show that selecting surfaces outside the near-field of structures allows reducing the number of patches, and an example of submerged structures is given. More recently, the PTF approach has been applied to solve a vibroacoustic problem involving porous materials [148] or has been used to allow coupling between geometrical acoustics and another domain [149].

1.2.5 *The Circumferential Admittance Approach (CAA)*

The Circumferential Admittance Approach (CAA) is a substructuring approach based on the admittance principle for linear systems [124, 125]. Developed by Maxit, it is a dedicated method to estimate the vibroacoustic behavior of an axsiymmetric submerged shell periodically or non-periodically stiffened by internal frames for a point force [21]. The approach consists in partitioning the system and considering the sub-

merged shell separately from the internal frames (ring stiffeners, bulkheads, end caps). Considering cylindrical coordinates (x, r, θ), as shown in Fig. 3a, all the physical variables (*i.e.* forces, shell displacements, pressure,...) can be written as Fourier series depending on circumferential orders n:

$$f(\theta) = \sum_{n \in \mathbb{Z}} \tilde{f}(n) \mathrm{e}^{\mathrm{j}n\theta} \tag{31}$$

where $n \in \mathbb{Z}$, because the system is 2π-periodic along the circumference, and with

$$\tilde{f}(n) = \frac{1}{2\pi} \int_{-\pi}^{\pi} f(n) \mathrm{e}^{-\mathrm{j}n\theta} \, \mathrm{d}\theta \tag{32}$$

In this approach, the shell and the frames are axisymmetric and the fluid domain is infinite. Under these assumptions, the circumferential orders are independent from each other [25].

On one hand, the circumferential admittances of the fluid loaded shell are estimated using the Flügge equations of motions [2, 3] and by solving the problem in the wavenumber space, as shown in appendix A. The resolution of these equations are performed using an accelerated spectral approach, which consists in modeling the problem by a fluid-loaded plate in the high wavenumbers. It has proven very good results in terms of accuracy and calculation cost. On the other hand, different types of internal frames can be modeled using axisymmetric FEM and shell elements. The coupling forces $\tilde{\mathbf{F}}^c$ between the shell and the stiffeners are then calculated thanks to the circumferential admittances of the subsystems $\tilde{\mathbf{Y}}^{shell}$ and $\tilde{\mathbf{Y}}^{frame}$ and to the free displacements of the subsystems $\tilde{\tilde{\mathbf{U}}}^{shell}$ and $\tilde{\tilde{\mathbf{U}}}^{frame}$, by inverting the following equation:

$$\left[\tilde{\mathbf{Y}}^{shell} + \tilde{\mathbf{Y}}^{frame}\right] \tilde{\mathbf{F}}^c = \tilde{\tilde{\mathbf{U}}}^{frame} - \tilde{\tilde{\mathbf{U}}}^{shell} \tag{33}$$

If the point force is applied to the cylindrical shell, the free displacements of the shell $\tilde{\tilde{\mathbf{U}}}^{shell}$ are the displacements of the submerged cylindrical shell when it is uncoupled from the internal frames and only excited by an external point force, and $\tilde{\tilde{\mathbf{U}}}^{frame} = 0$. If the point force is applied to an internal frame, the free displacements of the frame $\tilde{\tilde{\mathbf{U}}}^{frame}$ are the displacements of the excited fram when it is uncoupled from the other subsystems, and $\tilde{\tilde{\mathbf{U}}}^{shell} = 0$. The coupling forces are finally injected in the Flügge spectral equations and a 2D inverse Fourier transform is used to deduce the shell displacements and the near-field radiated pressure. The far-field radiated pressure is calculated using the stationary phase theorem presented in Eq. (14).

The CAA is then extended to model the scattering of a submerged cylindrical shell with axisymmetric internal frames [150]. The main difference is that the free displacements are calculated from the Flügge equations using on the right hand term the blocked pressure due to the oblique plane wave of incidence ξ to the normal of the cylinder:

$$p_b(x, r, \theta) = e^{j\bar{k}_x x} \sum_{n=-\infty}^{+\infty} \bar{p}_{b,n}(r) e^{jn\theta} \tag{34}$$

where $\bar{k}_x = k_0 \sin \xi$, and:

$$\bar{p}_{b,n}(r) = p_0 j^n \left[J_n(\bar{k}_r r) - \frac{1}{\cos \xi} \frac{J_n'(\bar{k}_r R)}{H_n^{(2)'}(\bar{k}_r R)} H_n^{(2)}(\bar{k}_r r) \right] \tag{35}$$

with p_0 the amplitude of the incident pressure, $\bar{k}_r = k_0 \cos \xi$, J_n the Bessel function of first kind of order n.

1.3 VIBROACOUSTIC BEHAVIOR OF CYLINDRICAL SHELLS COUPLED TO NON-AXISYMMETRIC INTERNAL FRAMES

Models of shell with non-axisymmetric internal structures have been proposed in the past. Some of these studies have focused on the vibroacoustic behavior of non-axisymmetric cylindrical shells *in vacuo*. Peterson and Boyd [151] use the extended Rayleigh-Ritz method and the introduction of Lagrange multipliers to study a cylindrical shell with a longitudinal floor partition, as shown in Fig. 7 [151]. Langley [152] uses a similar

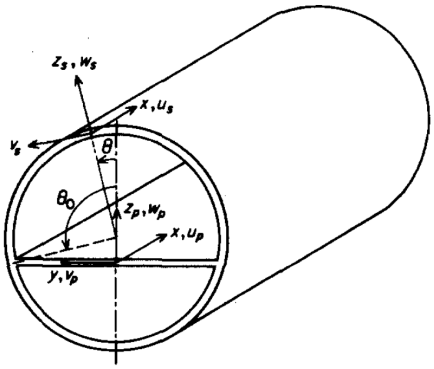

Figure 7: Cylindrical shell with floor partition.

technique for a stiffened shell with floor partition. The latter configuration is studied

by introducing artificial springs for every permitted degree of freedom uniformely distributed along the two junctions [153] or by using the admittance method [154, 155]. Besides, other studies taking into account heavy fluid loading in the shell model can be found. Rebillard *et al.* [156] use the addition of a mass-spring system in an immersed cylinder. They solve analytically the problem from the eigenmodes of the axisymmetric cylinder *in vacuo*, include a radiation impedance term to account for the fluid, and validate the results experimentally. Achenbach, Bjarnason and Igusa [157] study the influence of a non-axisymmetric substructure on a similar configuration and show that the mass-spring system can heftily modify the vibroacoustic behavior of the shell. Their method is based on a variational formulation and the introduction of Lagrange coefficients to account for the coupling forces. Depending on the frequency considered, adding such a subsystem can either increase or decrease the amplitude of the radiated sound field around the cylindrical shell. The same method is used to take into account floors and stiffeners in a 2-D problem on an infinitely long cylindrical shell [158, 159], to highlight the influence of non-axisymmetric excitations [160] and to consider the example of two longitudinal beams lying on stiffeners [161]. In the general formulation, the circumferential orders are coupled and results from the previous studies show that the coupling cannot be neglected in non-axisymmetric problems. This idea reinforces the results given by Laulagnet and Guyader [162], who break the axisymmetry of an immersed cylinder through partial masking, namely by overlaying the external surface of the cylinder by an acoustic decoupling coating. Similarly, Cuschieri and Feit [163] study the influence of the masking and notice that the coupling of the circumferential modes depends on its regularity.

The increasing complexity of the internal structures, including irregular spacing of stiffeners, non-axisymmetry and the addition of internal degrees of freedom changes some resonances, modifies the acoustic field and couples different modes [164]. To tackle these problems, for which geometry is more complex than the academic studies cited previously, experimental and numerical methods have been used. Photiadis *et al.* [61] build an experimental model of an immersed stiffened cylinder with numerous mass-spring systems attached on the stiffeners, and compare the measurements to a model without the resonators. They conclude that the internal structures induce several effects on the backscattered pressure (*i.e.* the pressure scattered back to the di-

rection of the incident wave) and in particular the attenuation of Bloch-Floquet waves. Bucaro *et al.* [165] clarify these results by modifying locally the structure admittance to account for the resonators. Because each complexity level tends to increase the level of the radiated and scattered field, it is advisable for industrial applications to keep as simple systems as possible and not to break the axisymmetry. This conclusion is equivalent to say that discontinuities tend to enhance the radiation efficiency of the structures [166]. The pressure radiated by an immersed shell with and without point masses is calculated by the FEM by Marcus and Houston [167]. In their example, they show that the coupling of the circumferential modes induces a rise in the radiation level of about 10 dB over a broad frequency range. Studies by coupled FEM-BEM give results at low frequency that highlight the crucial importance of isolating internal structures through flexible mounts [168, 169]. Li *et al.*[170] use the same technique to study the effect of the propulsion foundation and analyze the contribution of the individual modes. Ettouney *et al.* [171] solve the problem of a submerged axisymmetric shell by using the uncoupled circumferential harmonics. They use a sub-structuring approach based on the admittances to include three-dimensional systems in the axisymmetric shell while keeping the circumferential orders uncoupled. The system is thus equivalent to an axisymmetric submerged shell with internal point forces that account for the presence of the internal systems. Their method is however limited to point coupling.

1.4 CONTRIBUTION TO RESEARCH

The aim of the present work is to predict with a numerical method the vibroacoustic behavior of submerged stiffened cylindrical shells coupled to non-axisymmetric internal frames, as shown for example in Fig. 8, on a frequency range from some Hz to several kHz. The literature review shows that many works have been conducted on axisymmetric shells and that less attention has been paid to the non-axisymmetric case. Indeed, breaking the axisymmetry increases dramatically the computational cost. Analytical methods usually show their limits because of their low versatility and cannot thus meet the industrial needs. Element-based methods such as FEM can deal with the geometrical complexity, but are unadapted to industrial applications because of their high computational cost in middle and high frequencies. That is why substructur-

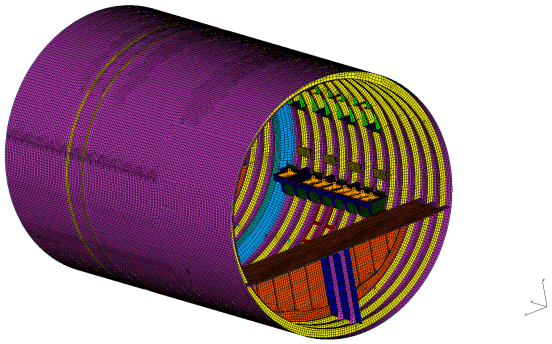

Figure 8: Example of a CAD model of a cylindrical shell with non-axisymmetric internal frame that can be met in industrial applications.

ing methods are considered to tackle such problems. However, the existing methods present some limits:

- the modal synthesis techniques or the introduction of Lagrange multipliers require the knowledge of the variational formulation or of a modal basis of each subsystem,
- the mid and high frequencies methods may either require assumptions that are not met for our case of interest (weak coupling, low modal density, convexity of the domains ...) or are not able to give local results,
- the classical admittance approach is limited to point coupling,
- the PTF method cannot deal with the interface between two thin mechanical structures,
- the CAA is limited to axisymmetric systems because of its assumptions.

Therefore, a new substructuring method, called the CTF method is developed to be able to couple along lines subsystems that are modeled by different techniques. It can be seen as an extension of the admittance method for line coupling, or as an extension of the CAA that allows non-axisymmetries.

In chapter 2, the CTF method is developed in the general case of thin mechanical structures coupled along lines. A set of orthonormal functions called condensation functions, which depend on the curvilinear abscissa along the coupling line, is considered. This set is then used as a basis for approximating and decomposing the displacements and

the applied forces at the line junctions. Thanks to the definition and calculation of CTF for each uncoupled subsystem and by using the superposition principle for passive linear systems, the behavior of the coupled subsystems can be obtained. The method is first developed and validated for plates and convergence criteria are defined in relation with the size of the basis of condensation functions. The CTF method is then applied to the case of a submerged stiffened cylindrical shell with non-axisymmetric internal frames. The system is partitioned in 3 types of subsystems: the submerged shell, the axisymmetric frames (stiffeners, bulkheads) and the non-axisymmetric frames. The submerged shell is described by a semi-analytical method based on the Flügge equations in the spectral domain. The axisymmetric frames are described by axisymmetric Finite Element models and the non-axisymmetric frames by Finite Element models. This technique allows the internal frames geometries to be more complex than usual academical systems, while keeping reasonable computational cost, and gives thus a tool to model industrial systems.

The influence of non-axisymmetric internal frames on the vibroacoustic behavior of a cylindrical shell for different excitations is examined. For a point force, test cases are presented in chapter 3 and the physical phenomena are discussed. More particularly, it can be shown that additional circumferential orders play a role in the response of the system coupled with non-axisymmetric internal frames, and the radiation efficiency tends to increase. An experimental study on a model in air is carried out to verify this trend in chapter 4. In chapter 5, the extension of the CTF method for an acoustical excitation is proposed. The influence of internal frames on the scattering from a submerged stiffened cylindrical shell is highlighted. On a test case, it is shown that the non-axisymmetric internal frames have weak influence on Bragg scattering but can modify greatly Bloch-Floquet scattering. A simplified model is built to explain how structural waves can propagate along these structures. The CTF method is finally coupled to the wavenumber-frequency approach and the reciprocity technique to study the response of a complex shell for random excitations in chapter 6, and gives thus a powerful tool to model complex structures excited by a TBL or a DSF.

2

PRINCIPLE OF THE CONDENSED TRANSFER FUNCTIONS METHOD

This chapter is based on the following articles:

- "A condensed transfer function method as a tool for solving vibroacoustic problems", published in the *Proceedings of the Institution of Mechanical Enginners, Part C: Journal of Mechanical Engineering Science* [172].
- "Prediction of the vibroacoustic behavior of a submerged shell with non-axisymmetric internal substructures by a condensed transfer function method", published in the *Journal of Sound and Vibration* [173].

It describes the principle of the Condensed Transfer Functions (CTF) method, which is presented as an extension of the classical admittance method, in the general case of thin mechanical structures coupled along a line. A discussion of the method is then carried out through a numerical study on a plate. Finally, an application to a shell is given.

2.1 CLASSICAL ADMITTANCE APPROACH FOR POINT COUPLED SUBSYSTEMS

Introduced first by Firestone [124], the admittance method has been used to calculate the harmonic response of subsystems coupled by contact points (see Fig. 9), and for an external load F_{ext}. The contacts are assumed to be perfect, without friction loss, and bilateral (meaning that the forces transmitted have the same amplitude but are of opposite sign).

For general 3-D problems, $\mathbf{U}_n^\alpha = \left[U_{n,p}^\alpha\right]_p$ is the vector of the 3 translations and 3 rotations of space at the point n and $\mathbf{F}_m^\alpha = \left[F_{m,q}^\alpha\right]_q$ the vector of the 3 forces and 3

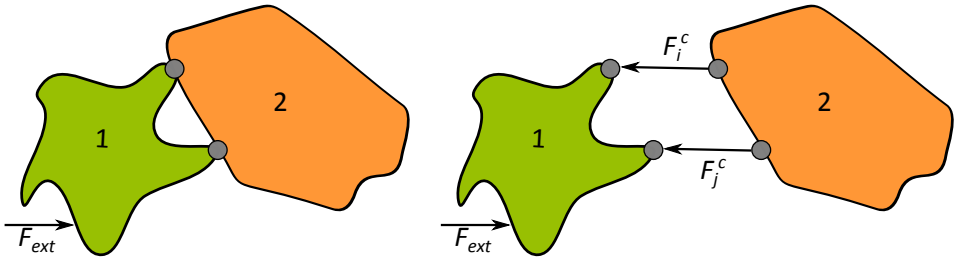

(a) (b)

Figure 9: (a) Subsystems linked by two point contacts. (b) Coupling forces between the two subsystems.

moments applied on m. The admittance $\mathbf{Y}^{\alpha}_{nm}$ of a subsystem α is defined as the ratio of the displacement at the point n over the force applied at the point m:

$$\mathbf{Y}^{\alpha}_{nm} = \left[\frac{U^{\alpha}_{n,p}}{F^{\alpha}_{m,q}}\right]_{1\leq p\leq 6, 1\leq q\leq 6}. \tag{36}$$

For two coupling points (n, m), the admittance $\mathbf{Y}^{\alpha}_{nm}$ is thus a 6×6 matrix to account for all the DOF.

Moreover, the displacement vector at point n of the uncoupled subsystems when only external loading is applied, is called *free displacement* and is written $\bar{\mathbf{U}}^{\alpha}_{n}$. Based on the superposition principle, the displacements of an uncoupled subsystem α at the contact point n can be written as:

$$\mathbf{U}^{\alpha}_{n} = \bar{\mathbf{U}}^{\alpha}_{n} + \mathbf{Y}^{\alpha}_{nn}\mathbf{F}^{\alpha}_{n} + \mathbf{Y}^{\alpha}_{nm}\mathbf{F}^{\alpha}_{m}\ , \alpha \in \{1, 2\}. \tag{37}$$

The displacements at the contact point m are simply derived from the previous equation by interchanging n and m.

The displacement continuity and force equilibrium between subsystem 1 and 2 are written for all connection points as

$$\begin{cases} \mathbf{U}^{1}_{n} = \mathbf{U}^{2}_{n} \\ \mathbf{F}^{1}_{n} = -\mathbf{F}^{2}_{n} = \mathbf{F}^{c}_{n} \end{cases}, \forall n. \tag{38}$$

Eqs. (37) and (38) yield to Eq. (39) and the coupling forces $\mathbf{F}^{c}_{n}$ at the connection points can thus be deduced by inverting the admittance term in the following equation:

$$\left(\mathbf{Y}^{1} + \mathbf{Y}^{2}\right)\mathbf{F}^{c} = \bar{\mathbf{U}}^{2} - \bar{\mathbf{U}}^{1}. \tag{39}$$

where the notation without subscripts denotes vector and matrices assembled for all connection points. In this case, as no external load is applied on subsystem 2, $\bar{\mathbf{U}}^2 = 0$.

This method can easily be extended to more than two coupling points by increasing the size of the admittance matrices and free displacement vectors [126].

2.2 EXTENSION TO LINE COUPLED SUBSYSTEMS

In industrial applications, it is likely that subsystems are coupled along lines rather than on points, as shown in Fig. 10. That is why the admittance method needs to be extended to allow line coupling. The same assumptions than in the classical admittance method are taken: the contacts are assumed to be perfect, without friction loss, and bilateral. The excitation is supposed harmonic at a pulsation ω and the time dependency $e^{j\omega t}$ is omitted in the following. A set of N functions called *condensation functions* is considered: $\{\varphi_n\}_{1\leq n\leq N}$. They are functions of the curvilinear abscissa s along the coupling line Γ. The number of transfer functions N plays a key role in the convergence of the method and its value will be discussed later in this work. The set of condensation functions is supposed to be orthonormal. For an uncoupled subsystem α, a CTF is defined as follows:

$$\mathbf{Y}^{\alpha}_{nm} = \left[\frac{\langle \hat{U}^{\alpha}_{m,q,p}, \varphi_n\rangle}{\langle F^{\alpha}_{m,q}, \varphi_m\rangle}\right]_{1\leq p\leq 6, 1\leq q\leq 6} = \left[\langle \hat{U}^{\alpha}_{m,q,p}, \varphi_n\rangle\right]_{p,q}, \tag{40}$$

where $\langle \bullet, \bullet\rangle$ is a scalar product. $\mathbf{F}^{\alpha}_{m}$ is the vector of the efforts on Γ, where the components in each direction of space is equal to φ_m. The indices p and q denote directions of space. $\hat{\mathbf{U}}^{\alpha}_{m,q}$ is the displacements vector of the junction Γ when the subsystem is excited in the direction q by a force of magnitude $F^{\alpha}_{m,q} = \varphi_m$.

It is assumed that the displacements vector $\mathbf{U}^{\alpha}$ at the junction can be written for each subsystem $\alpha \in \{1, 2\}$ as a linear combination of the condensation functions:

$$\begin{cases} \mathbf{U}^1(s) = & \sum_{n=1}^{N} \mathbf{u}^1_n \varphi_n(s) \\ \mathbf{U}^2(s) = & \sum_{n=1}^{N} \mathbf{u}^2_n \varphi_n(s) \end{cases}, \tag{41}$$

where $\mathbf{u}^{\alpha}_n$ is the condensed displacements vector of subsystem α associated with the condensation function φ_n.

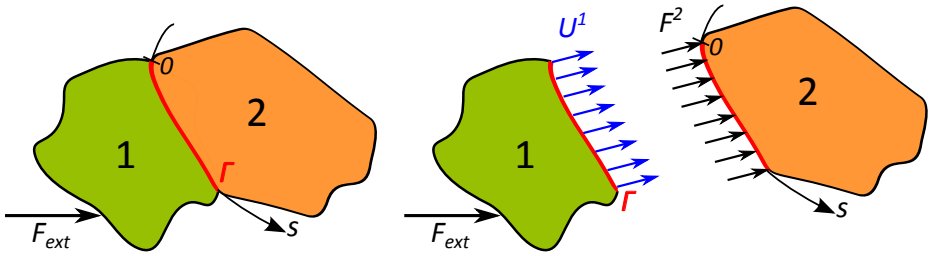

(a) (b)

Figure 10: (a) Subsystems coupled along a line Γ. (b) Uncoupled systems, forces and displacements at the junction.

Let us write $\mathbf{F}^\alpha(s) = \sum_{n=1}^{N} \mathbf{f}_n^\alpha \varphi_n(s)$ the efforts applied on the junction of the subsystem α. In response to these linear excitation forces, the superposition principle for passive linear systems enables to write the condensed displacements $\mathbf{u}_n^\alpha$ as:

$$\begin{cases} \mathbf{u}_n^1 = \bar{\mathbf{u}}_n^1 + \sum_{m=1}^{N} \mathbf{Y}_{nm}^1 \mathbf{f}_m^1 \\ \mathbf{u}_n^2 = \bar{\mathbf{u}}_n^2 + \sum_{m=1}^{N} \mathbf{Y}_{nm}^2 \mathbf{f}_m^2 \end{cases}, \forall s \in \Gamma, \forall n \in [\![1; N]\!], \tag{42}$$

where $\bar{\mathbf{u}}_n^\alpha = \left[\langle \bar{U}_p^\alpha, \varphi_n \rangle\right]_p$ are the free condensed displacements of the uncoupled subsystems. As on this example the subsystem 2 has no external load: $\bar{\mathbf{u}}_n^2 = 0, \forall n$.

Besides, the displacement continuity and force equilibrium lead to:

$$\begin{cases} \mathbf{U}^1(s) = \mathbf{U}^2(s) \\ \mathbf{F}^1(s) + \mathbf{F}^2(s) = 0 \end{cases}, \forall s \in \Gamma \tag{43}$$

The set of condensation functions being orthonormal, Eq. (43) yields:

$$\begin{cases} \mathbf{u}_n^1 = \mathbf{u}_n^2 \\ \mathbf{f}_n^1 = -\mathbf{f}_n^2 = \mathbf{f}_n^c \end{cases}, \forall n \in [\![1; N]\!] \tag{44}$$

Assembling the vectors and matrices for all the condensation functions and inserting Eq. (42) into the previous equation results in a similar formula than the classical admittance method to deduce the coupling forces between the subsystems:

$$\left(\mathbf{Y}^1 + \mathbf{Y}^2\right) \mathbf{F}^c = \bar{\mathbf{U}}^2 - \bar{\mathbf{U}}^1 \tag{45}$$

To clarify this point, the general expression for the admittance matrix and the free displacement vectors are given in the following equations:

$$\mathbf{Y}^{\alpha} = \begin{bmatrix} & \vdots & \vdots & \vdots & \\ \dots & \mathbf{Y}^{\alpha}_{nn} & \dots & \mathbf{Y}^{\alpha}_{nm} & \dots \\ & \vdots & \vdots & \vdots & \\ \dots & \mathbf{Y}^{\alpha}_{mn} & \dots & \mathbf{Y}^{\alpha}_{mm} & \dots \\ & \vdots & \vdots & \vdots & \end{bmatrix} \quad \text{and} \quad \bar{\mathbf{U}}^{\alpha} = \begin{bmatrix} \vdots \\ \bar{\mathbf{u}}^{\alpha}_{n} \\ \vdots \\ \bar{\mathbf{u}}^{\alpha}_{m} \\ \vdots \end{bmatrix} \tag{46}$$

where it is reminded that one element of the matrix $\mathbf{Y}^{\alpha}$ is a square matrix which size depends on the number of degrees of freedom (generally 6 in 3-D problems), to take into account all the possible directions of excitations and displacements. Similarly, one element of $\bar{\mathbf{U}}^{\alpha}$ is a 6 elements vector (still considering having a general 3-D problem) to calculate the response of the junction in all directions of space to the external load. The size of this system is therefore equal to the number of transfer functions multiplied by the number of degrees of freedom.

In practice, the admittance matrices are calculated by exciting each uncoupled subsystems by all the condensation functions one after the other. Indeed, as the set is orthonormal, the denominator of the admittance term is in this case equal to 1. The admittance is deduced by projecting the displacements on the condensation functions (see Eq. (40)).

Once the coupling forces have been calculated by inverting Eq. (45), one can deduce the response at any given points M_1 and M_2, respectively on subsystems 1 and 2:

$$\begin{cases} \mathbf{U}(M_1) = \bar{\mathbf{U}}^1(M_1) + \sum_{i=1}^{N} \mathbf{Y}^1_{M_1 i} \mathbf{F}^c_i \\ \mathbf{U}(M_2) = \bar{\mathbf{U}}^2(M_2) - \sum_{i=1}^{N} \mathbf{Y}^2_{M_2 i} \mathbf{F}^c_i \end{cases} \tag{47}$$

where $\mathbf{Y}^{\alpha}_{M_\alpha i}$ is the condensed transfer function at the point M_α of the uncoupled subsystem α and is defined as the response at the point M_α when the subsystem is excited by φ_i on Γ. As no external load is applied on subsystem 2, $\bar{\mathbf{U}}^2(M_2) = 0$.

The method has been presented for the case of the coupling between only two subsystems but can easily be extended to more complex systems, with more than one junction. Examples of condensation functions with their associated scalar product are given in the next section, before being applied to a plate test case.

2.3 NUMERICAL STUDY ON A PLATE

2.3.1 *Test case parameters*

To illustrate the method presented above, let us consider in this section two rectangular plates made of the same material and thickness and which characteristics and dimensions are given in Table 1. The plates lie in the $z = 0$ plane and the boundary conditions are free on all edges. The aim is to couple the two plates together along their longest edge, as shown in Fig. 11.

Table 1: Material characteristics and plates dimensions.

Parameter	Notation	Value	Unit
Young modulus	E	2.1×10^{11}	Pa
Poisson coefficient	ν	0.3	-
Density	ρ_s	7800	kg/m^3
Structural damping coeff.	η	0.02	-
Length of plate 1 & 2	L_Γ	1.5	m
Width of plate 1	l_1	1.2	m
Width of plate 2	l_2	1.3	m
Thickness	h	0.017	m

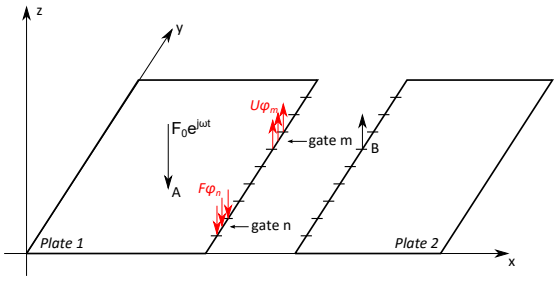

Figure 11: Two rectangular plates coupled along a line. Partition of the coupling line into 10 segments.

A reference calculation is made by the FEM on a 1.5×2.5 m^2 plate. Harmonic responses are calculated for frequencies lying between 10 Hz and 1500 Hz, with almost

400 values logarithmically spread over the domain. This choice ensures enough values to describe properly the resonances of the system regarding the value of the structural damping coefficient (see appendix B), which is accounted for as a complex factor in the stiffness matrix. One layer of quadrilateral isotropic shell elements of thickness h is chosen with a linear interpolation function. The Mindlin-Timoshenko formulation [174] is considered to take into account the effects of shear and rotational inertia. A virtual stiffness, which has no influence on the flexural waves, is added on the normal rotation in order to avoid numerical problems. The mesh is fine enough in order to respect the criterion of 6 elements per bending wavelength which is commonly used for such problems.

The two subsystems are modeled by FEM and the condensed admittances and free displacements need to be calculated for each of the two uncoupled subsystems. Thanks to its good convergence and calculation time, the frequency responses of the subsystems for different excitations are estimated by modal superposition including quasi-static modes [85]. This method consists in adding very low frequency mode shapes to the modal basis in order to compensate for the basis truncation. The basis truncation is made so that the frequency of the highest mode is at least 1.5 times higher than the highest frequency. For the case of the two plates described previously, the basis for plate 1 counts 116 modes (highest eigenfrequency at $f = 2848.6$ Hz) and 125 modes for plate 2 (highest eigenfrequency at $f = 2839.3$ Hz). Three examples of condensation functions are given in the next subsection and the results for the present test case are discussed.

2.3.2 *Three examples of condensation functions*

2.3.2.1 *Gate functions:*

The gate functions are defined according to their length as follows:

$$\varphi_n(s) = \begin{cases} \frac{1}{\sqrt{L_S}} & \text{if } (n-1)L_S \leq s < nL_S \\ 0 & \text{elsewhere} \end{cases} \quad \forall n \in [\![1; N]\!], \tag{48}$$

The scalar product associated to the gate function is defined in Eq. (49). Considering the set of piecewise continuous functions on segments $[a, b[$, it can be easily verified that the gate functions form an orthonormal set for this scalar product.

$$\langle f, g \rangle = \int_{\Gamma} f(s) g^*(s) ds \tag{49}$$

where * denotes the complex conjugate.

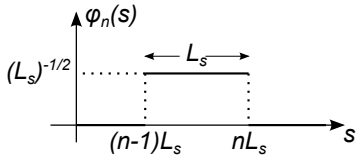

Figure 12: Gate function of length L_S.

The shape of one of these functions can be seen on the plot in Fig. 12. Building the admittance matrix of each subsystem in this case can be seen as dividing the coupling line into N segments, as shown in Fig. 11. The segments are excited one after the other, and the observation of the displacements allows obtaining a $6N \times 6N$ matrix, considering a 6 degrees of freedom problem. Each term of the free displacement vector is the result of the integral of the displacement on one segment due to the external load (point force at the point A in this case).

2.3.2.2 *Exponential functions:*

Instead of cutting the edge into segments, the idea of projecting the displacements on exponential functions is considered:

$$\varphi_n(s) = \frac{1}{\sqrt{L_\Gamma}} \exp\left(\frac{jn\pi s}{L_\Gamma}\right) \tag{50}$$

where L_Γ is the length of the junction Γ. This choice is motivated by the fact that the flexural motion of a plate can be described by trigonometric functions. The associated scalar product is defined as follows, ensuring the set to be orthonormal:

$$\langle f, g \rangle = \int_{\Gamma} f(s) g^*(s) ds \tag{51}$$

In practice, the whole line is excited by a force that varies as a complex exponential function along its curvilinear coordinate. A term of the admittance matrix is calculated by projecting the resulting displacement over an exponential function. Setting a certain i_{max}, this calculation has to be done for all the combinations $(n, m) \in [\![-i_{max}, i_{max}]\!]^2$. The free displacements are also projected on the exponential functions.

2.3.2.3 *Chebyshev polynomials:*

The Chebyshev polynomials are widely used to interpolate functions and are thus an interesting alternative for the condensation functions [175]. They can be defined recursively, and the 5 first functions are plotted in Fig. 13 with the substitution $X = \frac{2s}{L_\Gamma} - 1$:

$$\begin{cases} T_0(X) &= 1 \\ T_1(X) &= X \\ T_{n+2}(X) &= 2XT_{n+1}(X) - T_n(X) \end{cases} \tag{52}$$

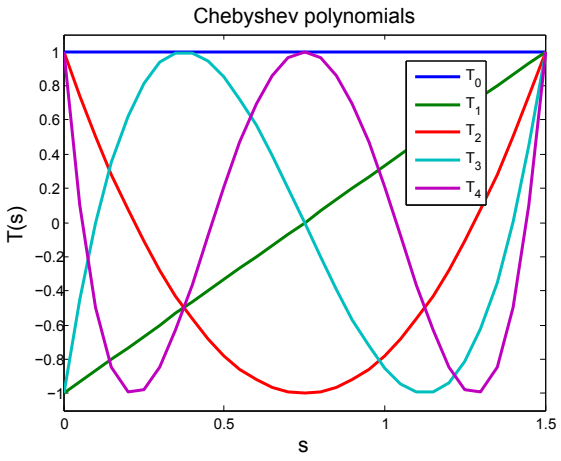

Figure 13: Chebyshev polynomials of first kind for $n \in \{0, 1, 2, 3, 4\}$.

The scalar product associated to the Chebyshev polynomials takes into account the weight function $\frac{1}{\sqrt{s(L_\Gamma - s)}}$:

$$\langle f, g \rangle = \frac{L_\Gamma}{\pi} \int_\Gamma f(s) g^*(s) \frac{1}{\sqrt{s(L_\Gamma - s)}} ds \tag{53}$$

The weight function ensures the set $\frac{T_0}{\sqrt{2}} \cup (T_n)_{n \in \mathbb{N}^*}$ to be orthonormal and reduces numerical errors by quadratically clustering the nodes at the end of the segment.

2.3.3 *Results with $N = 3$ transfer functions*

The mean quadratic transverse velocity on the surface of the two plates coupled together is calculated thanks to the CTF method with the 3 different condensation functions presented previously and is compared to a reference calculation. Considering the coordinates origin at the bottom left of plate 1, the system is excited by a transverse harmonic excitation at the point of coordinates $(0.9; 0.5)$. In Fig. 14, the responses and the relative errors are plotted as a function of the frequency in narrow band, with 3 transfer functions for the CTF methods ($N = 3$). This criterion means:

- dividing Γ in 3 segments when the condensation functions are gates;
- taking $i_{max} = 1$ for the exponential functions:

$$\varphi(s) \in \{\frac{1}{\sqrt{L_\Gamma}} \exp(\frac{-\mathrm{j}\pi s}{L_\Gamma}); \frac{1}{\sqrt{L_\Gamma}}; \frac{1}{\sqrt{L_\Gamma}} \exp(\frac{\mathrm{j}\pi s}{L_\Gamma})\}$$

- using the 3 Chebyshev polynomials T_0, T_1 and T_2;

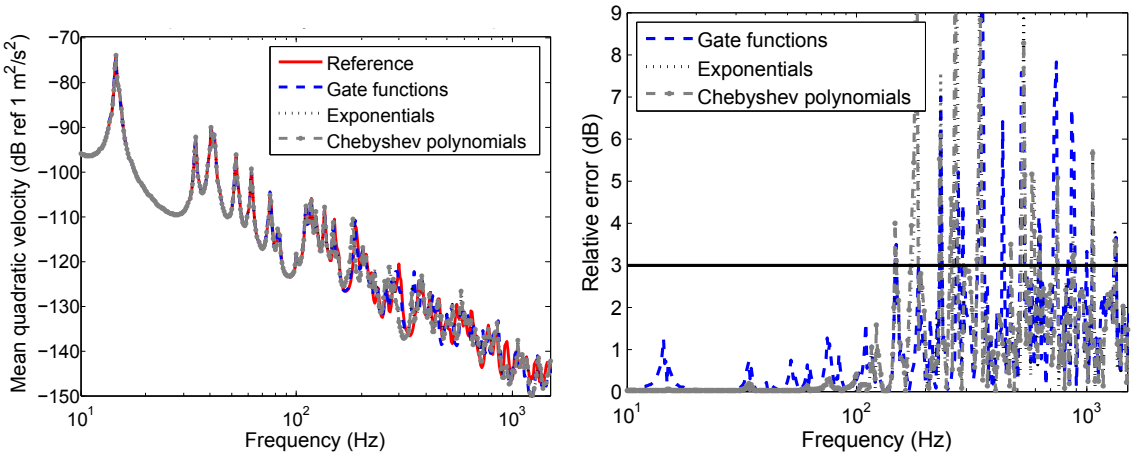

(a) (b)

Figure 14: (a) Mean quadratic transversal velocity of the system made of the two coupled plates and for a point harmonic load. Comparison between the reference and the CTF methods with $N = 3$. (b) Relative error (dB) of the mean quadratic transversal velocity in comparison to the FEM reference for the three CTF methods with $N = 3$.

Based on the observations in Fig. 14, it seems that the results fit well up to around $f_{lim} \simeq 150$ Hz. For this test case, some differences up to 1 dB can be seen at the reso-

nance frequencies for the case of the gate functions. These differences are due to a slight frequency shift in the resonance and are acceptable for industrial applications. Above this frequency, the transfer functions are not able to describe properly the phenomena. In other terms, the forces and displacements cannot be correctly interpolated by the condensation functions at higher frequencies.

2.3.4 *Convergence criteria*

Assuming that at least 2 points per wavelength are necessary to sample a signal (*cf.* Nyquist-Shannon sampling theorem [176]), one can link the number of transfer functions N with the frequency limit f_{lim} ensuring convergence of the results. Considering that λ_f is the flexural wavelength of the plate at f_{lim}, and based on the observations of the previous subsection, the convergence criteria can be written as follow:

- for gate functions, two segments are needed to describe a wavelength:

$$L_S \leq \frac{\lambda_f}{2} \tag{54}$$

- for Chebyshev polynomials, the degree of the polynomial must be at least equal to the number of points that the function needs to interpolate:

$$N_{max} \geq \frac{2L_\Gamma}{\lambda_f} - 1 \tag{55}$$

- the same reasoning can be made for exponential functions, noting that in this case i can take negative values:

$$i_{max} \geq \frac{L_\Gamma}{\lambda_f} - \frac{1}{2} \tag{56}$$

These criteria are equivalent, meaning that a frequency results in the same number of transfer functions for each condensation function. For a 17 mm thick plate, $N = 3$ leads to a frequency limit of $f_{lim} = 168$ Hz, which fits the observations of Fig. 14. Applying those criteria, $N = 10$ transfer functions are needed to ensure the convergence of the results above 1500 Hz. The convergence is moreover checked in Fig. 15 for the transversal displacements of points A and B. The coordinates of the point B are $(1.2; 0.9)$ and the point is supposed to be located on the subsystem 2 for the CTF calculation. The

plots on Fig. 15 have only been presented with the CTF method using the gate functions, but the complex exponentials and the Chebyshev polynomials show good convergence too.

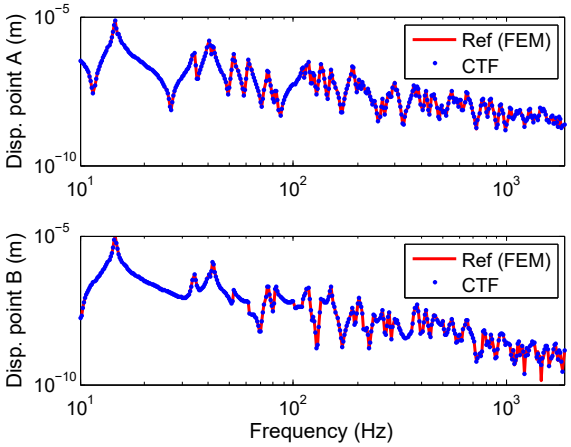

Figure 15: Transversal displacement of point A (*top*) and point B (*bottom*). Comparison between the reference and the CTF method with 10 gate functions ($L_S = 0.15$ m).

For the case of Chebyshev polynomials, the amplitude of the transverse force is plotted as a function of the frequency and the condensation functions in Fig. 16. For each frequency, the values are normalized with regard to the highest amplitude. Considering the dispersion relation for a plate, Eq. (55) yields :

$$N \geq \sqrt{\frac{2f}{\pi}} L_\Gamma \left(\frac{Eh^2}{12(1-\nu^2)\rho_p} \right)^{1/4} - 1 \tag{57}$$

N is an integer and rounded toward positive infinity. N is plotted as a function of the frequency in Fig. 16 using a white line. It clearly shows that the higher the frequency, the more Chebyshev polynomials play a role in the method. It also shows that, except for some frequency values below 55 Hz, the criterion is very well suited to properly approximate the forces at the junction.

2.3.5 *Position of the excitation point*

To check whether the method is still valid when the vibration shape at the line junction becomes more intricate, the excitation is moved to the point of coordinates $(1.2; 0.5)$ and lies thus on the edge of plate 1, at the junction with plate 2. The amplitude of the

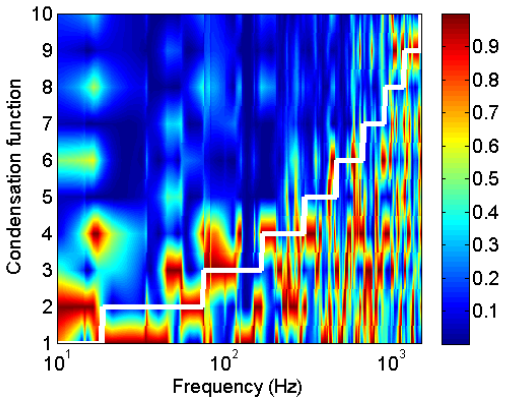

Figure 16: Normalized amplitude of the transverse force at the junction projected on the Chebyshev polynomials as a function of the frequency. The white line represents the convergence criterion.

transversal displacement is plotted as a function of the abscissa on the coupling line in Fig. 17, for the cases where the excitation is on or further away from the junction. The frequency of 1414 Hz has been chosen, because important discrepancies have been seen at this frequency for the CTF method with Chebyshev polynomials. The mesh for the finite element calculation is 5 times finer in order to have smoother curves, but the CTF calculations were still performed with the coarser mesh used previously in this paper. When the excitation point is on the junction, the vibration shape is less regular along the line than for the case where the excitation point is further from the junction. In particular, a singularity can be seen on the red solid curve at $y = 0.5$ m, corresponding to the location of the excitation point.

The relative errors of the mean quadratic velocity compared to FEM reference calculations are evaluated for the two positions of the excitation point, for the three different sets of condensation functions. The number of condensation functions are chosen accordingly to the convergence criteria. It can be seen in Fig 18a that the position of the excitation point has no influence on the convergence of the CTF method for the case of the gate and exponential functions (only plotted for exponential functions for the sake of clarity). Nevertheless, for the case of the Chebyshev polynomials, the set is not suited to describe properly the singularity on the junction and leads to more important errors, as seen on the plot in Fig. 18b.

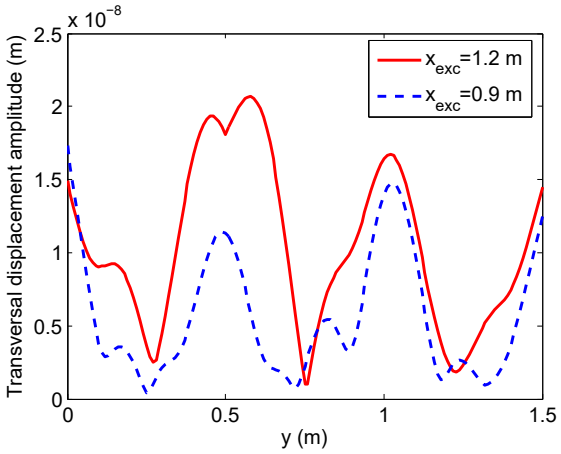

Figure 17: Amplitude of the transversal displacement along the coupling line for two different positions of the excitation point at $f = 1414$ Hz.

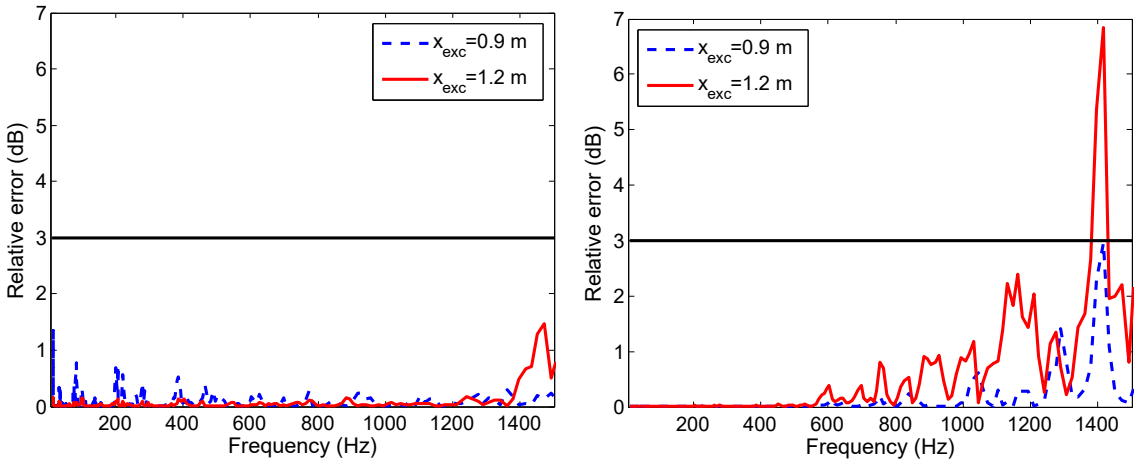

(a) (b)

Figure 18: Relative error (dB) of the mean quadratic transversal velocity in comparison to the FEM references for the CTF method with (a) $N = 11$ exponential functions. (b) $N = 10$ Chebyshev polynomials. Comparison for two positions of the excitation point.

As a general comment, it is thus advisable to avoid having singularities on the coupling line, to be able to approximate more easily the physical values at the junction. In other words, for Chebyshev polynomials at least, the coupling line should remain far enough from the excitation to get rid of the near-field effects.

2.3.6 *Influence of the cross CTF*

Similarly to the cross admittance (*i.e.* the extra-diagonal blocks of the admittance matrix: $n \neq m$), the cross CTF is defined as the extra-diagonal blocks of the CTF matrix that link different condensation functions: $n \neq m$. One can wonder if these terms play an important role and if there is a coupling between the different condensed transfer functions. The results are plotted in Fig. 19 with $N = 10$ transfer functions, to ensure good convergence on the whole frequency domain. They are given for the case of full admittance matrices, and the case where the extra-diagonal blocks are set to zero. It is clear that it poorly converges in the latter case. Thus it can be said that the cross CTF is not insignificant and cannot be neglected. The results have been shown with the gate functions only but similar results are observed with other condensation functions.

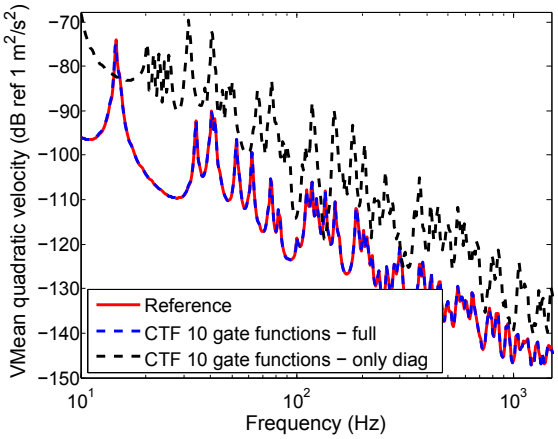

Figure 19: Influence of the cross CTF on the mean quadratic transversal velocity of the coupled system.

2.3.7 *Numerical sensitivity*

Like most of the numerical methods, it is important to check the stability of the method with regard to the input data. As seen in Eq. (45), the CTF method involves the inversion of the sum of the admittance matrices. The condition number with respect to inversion is used to check if a problem is ill-conditionned and is usually defined as the ratio of the largest singular value of the matrix to the smallest [177]. If this number is particularly high, it indicates that the problem is sensitive to numerical errors.

For the CTF methods with 10 transfer functions, the condition number is plotted as a function of the frequency in Figure 20. Although small fluctuations on the condition number at 734.6 and 1019 Hz can be seen, it can be considered that it remains around 10^8 for the gate functions and the Chebyshev polynomials on the whole frequency domain . The condition number for the exponential functions is much higher (around 10^{14}) and it can thus be said that the method is more sensitive to numerical errors in this case, even if the results show good agreement with the reference calculation.

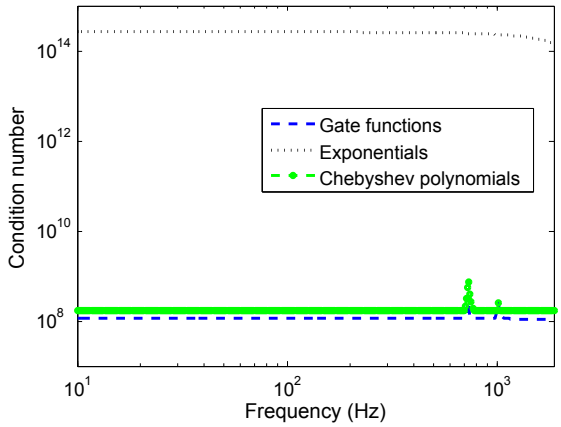

Figure 20: Condition number with respect to inversion of the sum of the admittance matrices, as a function of the frequency.

2.4 VALIDATION ON A CURVED SHELL

To show that the convergence criteria defined earlier in this paper remains valid for the case of subsystems coupled along a non-straight line connection, a curved shell as

shown in Fig. 21 is considered. It has the same dimensions and material parameters as the plate presented in the beginning of the section, but a 2.5 m curvature is imposed widthwise. The excitation is normal to the shell at the point of coordinates $(0.9; 0.5)$, the coupling line is selected at $x = 1.2$ m and the normal mean quadratic velocity on the surface of the whole plate is calculated by FEM (reference) and by the CTF method. For the sake of simplicity and because it has proven to give the best results in the previous sections, only the set of gate functions is considered for this case.

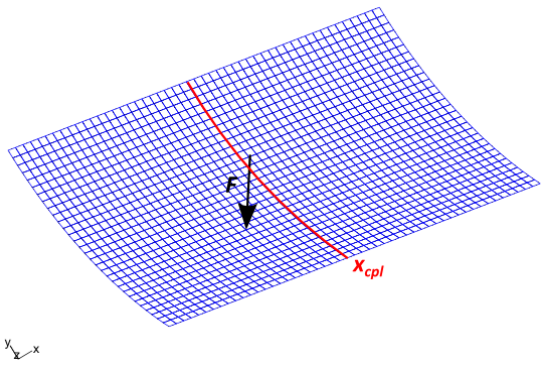

Figure 21: Mesh of a curved shell.

In Fig. 22, the response of the plate is recalled (black dotted line) and is compared to the response of the curved shell (red solid line).

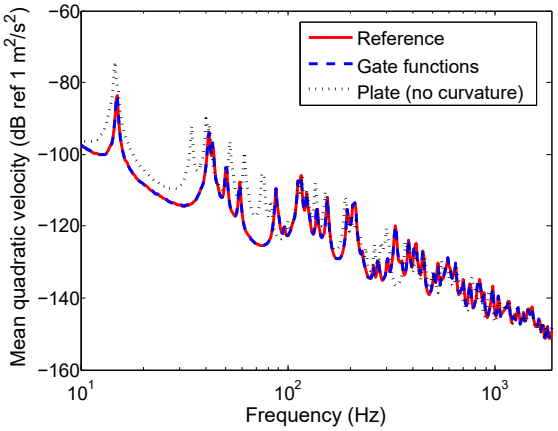

Figure 22: Mean normal quadratic transversal velocity on the system made of two curved shells and for a point harmonic load. Comparison between the reference and the CTF method with $N = 10$ gate functions.

The increase in the natural frequencies of the system shows that the curvature increases the stiffness of the structure. Thus, at a given frequency, the flexural wavelength is longer in the curved shell than in the planar structure, and could result in a less restrictive criterion (*i.e.* wider gate functions for instance). Nevertheless, as the flexural wavelength in a curved shell cannot be calculated easily, the convergence criterion is calculated from the flexural wavelength in the planar structure of same material properties and thickness. $L_S = 0.15$ m wide gate functions are accordingly considered to ensure the convergence of the method. Through this example, the plot on Fig. 22 shows that the CTF method is still valid on more complex cases with non-straight line connections.

2.5 CONCLUSIONS

A sub-structuring approach based on the mobility method has been developed to couple mechanical systems along a line junction. Efforts and displacements are condensed thanks to a set of orthonormal functions and the coupling forces between the subsystems are deduced. The method has shown good results on simple structures and convergence criteria have been highlighted. In particular, the so-called gate functions seem to be more efficient in terms of numerical sensitivity and at the same time more robust to singularities. These condensation functions can be compared to the patches used in the PTF method [144] for the coupling with acoustic domains. Unlike classical reduction methods, such as Component Mode Synthesis [90] or branch mode analysis [91], the subsystems in the CTF method do not necessarily need to be described by FEM or by projections on a modal basis. Indeed, it is sufficient to be able to evaluate the admittance at the interfaces by any mean to apply the method.

It is important to keep in mind that in the CTF method, the values at the junctions are approximations. As the method requires a matrix inversion, slight numerical errors can be introduced. The evaluation of the CTF for the uncoupled subsystems should thus be as accurate as possible and that is why residual modes are used when the response is calculated by modal superposition to increase the convergence. Besides, the convergence criterion proposed in this work needs to be respected in order to keep low errors.

The CTF method can now be further applied to the case of non-straight line connections. More particularly, it presents a great interest to add non-axisymmetric internal frames to submerged cylindrical shells: structures such as longitudinal floors or curved plates linking adjacent stiffeners can be found in industrial applications. Many studies have focused on the vibroacoustic behavior of shells immersed in water so far, but only a very few of them have considered non-axisymmetry. To tackle this issue, the idea is to couple together using CTF:

- an axisymmetric stiffened submerged shell described by the dedicated CAA [21].
- non-axisymmetric internal frames modeled by FEM to offer flexibility on their design.

Results are presented for a test case in the next chapter and the influence of the non-axisymmetric internal frames will be discussed.

3

VIBROACOUSTIC BEHAVIOR OF SUBMERGED STIFFENED CYLINDRICAL SHELLS COUPLED TO NON-AXISYMMETRIC INTERNAL FRAMES FOR A POINT FORCE

This chapter is based on the article entitled "Prediction of the vibroacoustic behavior of a submerged shell with non-axisymmetric internal substructures by a condensed transfer function method", published in the *Journal of Sound and Vibration* [173].

In order to validate the CTF method for our case of interest and to illustrate its advantages in coupling different models, it is applied to the case of an axisymmetric stiffened shell coupled to non-axisymmetric internal structures. First, the principle of the approach is described for the general case in subsection 3.1 before highlighting the procedure to calculate the condensed transfer functions from a dedicated CAA model in subsection 3.2. Then, for validation purposes, a shell *in vacuo* is considered, so that results can be easily compared with a full FEM calculation. Finally, the influence of the non-axisymmetric structures on the vibroacoustic behavior of a submerged stiffened cylindrical shell is discussed through two test cases.

3.1 PRINCIPLE OF THE CTF APPROACH FOR THE CASE OF A CYLINDRICAL SHELL

Let us consider a stiffened cylindrical shell with a non-axisymmetric internal frame, as shown on the sketch in Fig. 23a. The system is divided in two subsystems: subsystem 1 is the non-axisymmetric internal frame (see Fig. 23b), and subsystem 2 is the axisymmetric stiffened submerged shell (see Fig. 23c). The junctions between the two subsystems are supposed to be arcs at fixed x and r coordinates, and extending between θ_0 and θ_{N+1}.

On one hand, the admittances of the axisymmetric submerged stiffened shell are estimated by the CAA [21]. During this step, a numerical model of an immersed shell is coupled with Finite Element models of stiffeners and bulkheads using the admittance

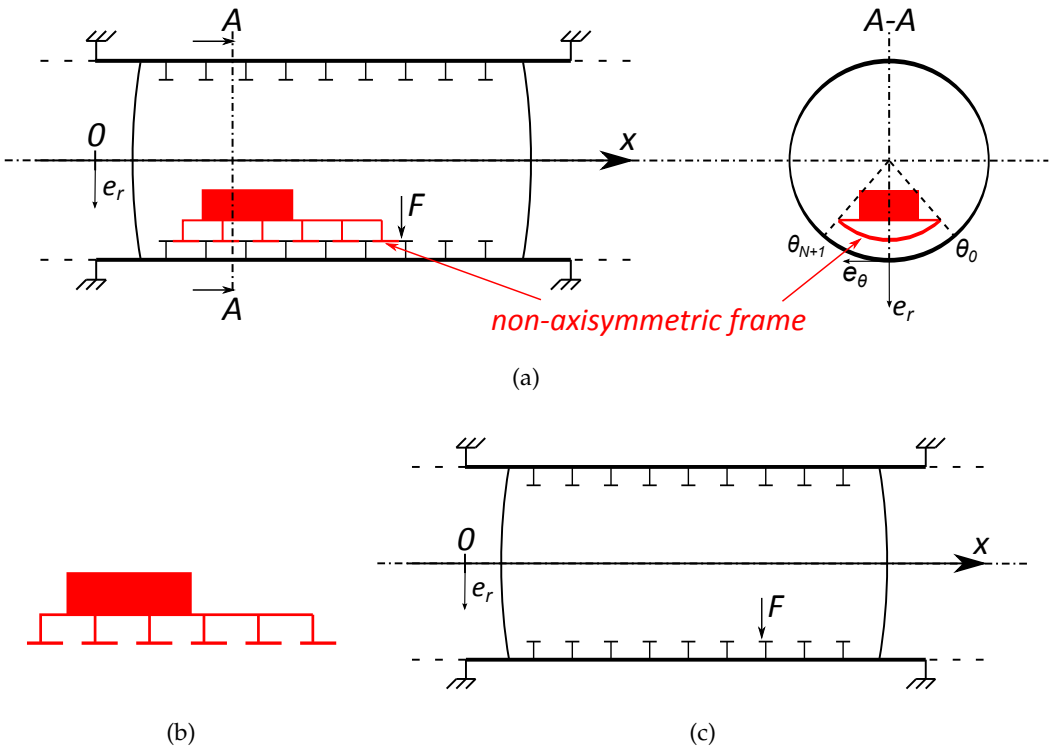

Figure 23: Sections of a stiffened cylindrical shell. (a) Including a non-axisymmetric internal frame. (b) Example of non-axisymmetric internal frame. (c) Axisymmetric partition described using CAA.

method projected on circumferential orders. The displacements and radiated pressure in the circumferential order space are then used to calculate the admittance terms needed as an input of the CTF method. This step is described in details in section 3.2.

On the other hand, the admittances of the non-axisymmetric internal frame are calculated by FEM. The frame is isolated and excited by forces equal to the condensation functions chosen for the CTF method on the junctions. Modal superposition with residual mode shapes [85] is used to calculate the displacements of the junction to these excitations. The displacements are finally projected on the condensation functions to build the CTF.

Eq. 45 is reminded here to deduce the condensed coupling forces between the two subsystems, where superscript 1 refers to the non-axisymmetric internal frame and superscript 2 refers to the axisymetric stiffened submerged shell:

$$\left(\mathbf{Y}^1 + \mathbf{Y}^2\right) \mathbf{F}^c = \bar{\mathbf{U}}^2 - \bar{\mathbf{U}}^1 \tag{58}$$

According to Eq. (47), the pressure p at a point M_f in the fluid domain (part of subsystem 2) and the displacement $\mathbf{U}$ at a point M_s on the shell are finally given by:

$$\begin{cases} p(M_f) = & \bar{p}(M_f) - \sum_{i=1}^{N} \mathbf{Y}^2_{M_f i} \mathbf{F}^c_i \\ \mathbf{U}(M_s) = & \bar{\mathbf{U}}(M_s) - \sum_{i=1}^{N} \mathbf{Y}^2_{M_s i} \mathbf{F}^c_i \end{cases} \tag{59}$$

where $\bar{p}(M_f)$ (resp. $\bar{\mathbf{U}}(M_s)$) is the pressure at the point M_f (resp. the displacement at the point M_s) in response to the external point force of the axisymmetric system.

The diagram shown in Fig. 24 summarizes the process to take into account non-axisymmetric internal frame in an immersed stiffened shell described by CAA.

3.2 CTF FROM CAA RESULTS FOR AN AXISYMMETRIC SUBMERGED STIFFENED SHELL

3.2.1 *Quantities of interest*

In this part, the Circumferential Admittance Approach (CAA) described in details by Maxit and Ginoux [21], and summarized in section 1.2.5 is used for modeling the vibroacoustic behavior of a non periodically stiffened submerged shell, and to calculate

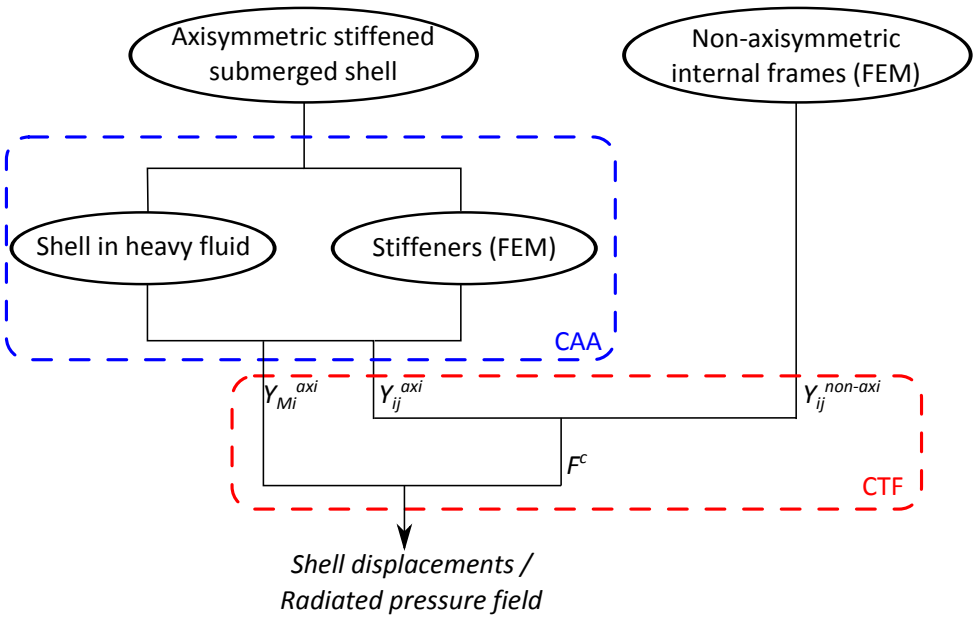

Figure 24: Sketch of the method to account for non-axisymmetric internal frames in a non periodically stiffened submerged shell.

the admittances needed as an input for the CTF approach. It is reminded that the CAA is based on the projection of the quantities on circumferential orders and that output data (displacements and radiated pressure) can be directly extracted for each circumferential order.

In order to use the CTF approach to add a non-axisymmetric internal frame, two quantities are needed from the CAA: the condensed transfer functions $\mathbf{Y}_{ij}^2$ at the junctions with the non-axisymmetric system for Eq. (58), and the transfer function $\mathbf{Y}_{Mi}^2$ between a point M and a condensation function φ_i applied on one of the junctions (see Eq. (59)). If M is a point on the cylindrical shell surface, the latter transfer function represents the displacement of the point when the axisymmetric shell is excited by the condensation function φ_i. If M is a point in the fluid domain outside the shell, $\mathbf{Y}_{Mi}^2$ represents the pressure at the point when the axisymmetric shell is excited by the condensation function φ_i.

3.2.2 *Benefit from the axisymmetric property*

This paragraph shows how the axisymmetric property of the stiffened submerged cylindrical shell is used to calculate the CTF more efficiently. As the system is axisymmetric, the response (displacement or pressure) of any point M with the coordinates (x_M, r_M, θ_M) in response to a point harmonic force on the structure at a point A with the coordinates (x_A, r_A, θ_A) can be calculated from the response to an excitation in $\theta = 0$:

$$\mathbf{Y}^2_{MA} = \mathbf{Y}^2_{M'A'} \tag{60}$$

where M' is the point with the coordinates $(x_M, r_M, \theta_M - \theta_A)$ and A' is the point with the coordinates $(x_A, r_A, 0)$. As the CAA enables to calculate any $\mathbf{Y}^2_{MA}$, let us then consider for the sake of clarity that $\theta_A = 0$. In the following, $\mathbf{Y}^2$ is written as a function of θ meaning that it is the value at the point of coordinate θ in response to an excitation in $\theta = 0$.

The displacements vector $\hat{\mathbf{U}}_j(\theta)$ in all the directions of space of a point of coordinate θ in response to a condensed force φ_j is then calculated by convolution:

$$\hat{\mathbf{U}}_j(\theta) = \int_{\theta_0}^{\theta_{N+1}} \mathbf{Y}^2(\theta - \alpha)\varphi_j(\alpha)\,\mathrm{d}\alpha \tag{61}$$

The CTF are then calculated by:

$$\begin{aligned} \mathbf{Y}^2_{ij} &= \frac{\langle \hat{\mathbf{U}}_j(\theta), \varphi_i(\theta) \rangle}{\langle \varphi_j(\theta), \varphi_j(\theta) \rangle} \\ &= \langle \int_{\theta_0}^{\theta_{N+1}} \mathbf{Y}^2(\theta - \alpha)\varphi_j(\alpha)\,\mathrm{d}\alpha, \varphi_i(\theta) \rangle \end{aligned} \tag{62}$$

$$\begin{aligned} \mathbf{Y}^2_{Mj} &= \frac{\hat{\mathbf{U}}_j(\theta)}{\langle \varphi_j(\theta), \varphi_j(\theta) \rangle} \\ &= \int_{\theta_0}^{\theta_{N+1}} \mathbf{Y}^2(\theta - \alpha)\varphi_j(\alpha)\,\mathrm{d}\alpha \end{aligned} \tag{63}$$

Eqs. (62) and (63) show that all the CTF can be calculated from the response $\mathbf{Y}^2(\theta)$ to one point force on each junction. This is valid because the system is axisymmetric and the junction is at constant x and r.

3.2.3 *Calculation using gate functions*

Eqs. (62) and (63) give the expressions to calculate the CTF for an axisymmetric system for any condensation function φ. In this work, the condensation functions chosen are the gate functions described in 2.3.2.1. Indeed, among the three condensation functions tested in chapter 2, the gate functions are the easiest to implement, as they consist in splitting the junction into segments. This section shows how the expressions of the CTF can be simplified using these condensation functions.

As the coupling lines are considered to be at fixed x and r, the gates can be considered as functions of θ (*i.e.* $\varphi_i(\theta) = 1$ between θ_1^i and θ_2^i, and $\varphi_i(\theta) = 0$ elsewhere). Writing the terms $\mathbf{Y}^2(\theta)$ as Fourier series (directly given by the CAA), Eq. (62) leads to the admittance $\mathbf{Y}^2_{ij}$ of the axisymmetric system in the physical space:

$$\begin{aligned}
\mathbf{Y}^2_{ij} &= \frac{1}{\sqrt{\theta_2^i - \theta_1^i}} \int_{\theta_1^i}^{\theta_2^i} \left(\frac{1}{\sqrt{\theta_2^j - \theta_1^j}} \int_{\theta_1^j}^{\theta_2^j} \sum_n \tilde{\mathbf{Y}}^2(n) \mathrm{e}^{\mathrm{j}n(\theta-\alpha)} \, \mathrm{d}\alpha \right) \mathrm{d}\theta \\
&= \sqrt{\theta_2^j - \theta_1^j} \sqrt{\theta_2^i - \theta_1^i} \tilde{\mathbf{Y}}^2(0) \\
&\quad + \frac{1}{\sqrt{\theta_2^i - \theta_1^i}} \frac{1}{\sqrt{\theta_2^j - \theta_1^j}} \sum_{n \neq 0} \frac{\tilde{\mathbf{Y}}^2(n)}{n^2} \left(\mathrm{e}^{-\mathrm{j}n\theta_2^j} - \mathrm{e}^{-\mathrm{j}n\theta_1^j} \right) \left(\mathrm{e}^{\mathrm{j}n\theta_2^i} - \mathrm{e}^{\mathrm{j}n\theta_1^i} \right)
\end{aligned} \tag{64}$$

with $\tilde{\mathbf{Y}}^2(n)$ the projection of the admittance on the circumferential order n. In this formula, no confusion should be made between the notation of the complex number $\mathrm{j} = \sqrt{-1}$ and the index j of a condensation function. Similarly, Eq. (63) yields:

$$\begin{aligned}
\mathbf{Y}^2_{Mj} &= \frac{1}{\sqrt{\theta_2^j - \theta_1^j}} \int_{\theta_1^j}^{\theta_2^j} \sum_n \tilde{\mathbf{Y}}^2(n) \mathrm{e}^{\mathrm{j}n(\theta-\alpha)} \, \mathrm{d}\alpha \\
&= \sqrt{\theta_2^j - \theta_1^j} \tilde{\mathbf{Y}}^2(0) + \frac{\mathrm{j}}{\sqrt{\theta_2^j - \theta_1^j}} \sum_{n \neq 0} \frac{\tilde{\mathbf{Y}}^2(n)}{n} \left(\mathrm{e}^{-\mathrm{j}n\theta_2^j} - \mathrm{e}^{-\mathrm{j}n\theta_1^j} \right) \mathrm{e}^{\mathrm{j}n\theta}
\end{aligned} \tag{65}$$

In practice, Eq. (64) and (65) are truncated to a maximal circumferential order $\bar{N}$. This number is defined considering the natural wavenumbers of the shell, the frames and the acoustic fluid, as explained in [21].

From the expression presented in Eq. (65), it is clear that $\mathbf{Y}^2_{Mj}$ can be written as Fourier series : $\mathbf{Y}^2_{Mj} = \sum_n \tilde{\mathbf{Y}}^2_{Mj}(n)$. Injecting this expression into Eq. (59) allows writing

the response of the non-axisymmetric system in Fourier series, where the contribution for a circumferential order n is given by:

$$\begin{cases} \tilde{p}_{M_f}(n) = & \tilde{\tilde{p}}_{M_f}(n) + \sum_{i=1}^{N} \tilde{\mathbf{Y}}^2_{M_f i}(n)\mathbf{F}^c_i \\ \tilde{\mathbf{U}}_{M_s}(n) = & \tilde{\tilde{\mathbf{U}}}_{M_s}(n) + \sum_{i=1}^{N} \tilde{\mathbf{Y}}^2_{M_s i}(n)\mathbf{F}^c_i \end{cases} \tag{66}$$

The examples of cylindrical shells with non-axisymmetric internal frames given all along this thesis are considered to be symmetric (the geometry, the excitations and the condensation functions). According to appendix C, Eq. (66) needs to be calculated only for $n \geq 0$ in the symmetric case. The radial response or the pressure in the physical space for any cylindrical coordinate θ can be deduced from the sum of the positive circumferential order (see Eq. (130)). The study of non-symmetric systems is however possible with this method and remains efficient. Indeed, the CAA still needs to be calculated for the positive circumferential orders only, but in that case Eq. (66) needs to be evaluated for $n \in \mathbb{Z}$.

3.3 VALIDATION ON A SHELL *in vacuo*

3.3.1 *Definition of the system*

A cylindrical shell of radius $R = 5$ m, length $L = 4$ m and wall thickness $h = 30$ mm is clamped at both ends. It is stiffened by two identical stiffeners with T cross-section at $x = 1$ and $x = 2$ m from the boundary of the shell. A T-stiffener consists of two perpendicular parts called the flange and the web (see Fig. 3b). The web is characterized by its height h_w and thickness t_w and the flange is characterized by its width w_f and thickness t_f. Both the web and the flange are modeled by shell elements. In this example, the T-stiffeners have the following dimensions: $(h_w \times t_w / w_f \times t_f) = (200 \times 15/200 \times 15)$ mm. A curved plate with a curvature radius of $R_{int} = 4.8$ m links the two stiffeners as shown in Fig. 25. The shell along with the two stiffeners will be referred to as the axisymmetric subsystem, whereas the plate is the non-axisymmetric subsystem, extending between θ_0 and θ_{N+1}, with $-\theta_0 = \theta_{N+1} = 0.2083$ rad. The dimension of the plate is thus 0.8×2 m^2 and it is 15 mm thick. An unitary external load is applied at the joint between the first

stiffener and the plate at $\theta = 0$. The shell is not immersed in heavy fluid so that a reference calculation can easily be done by FEM.

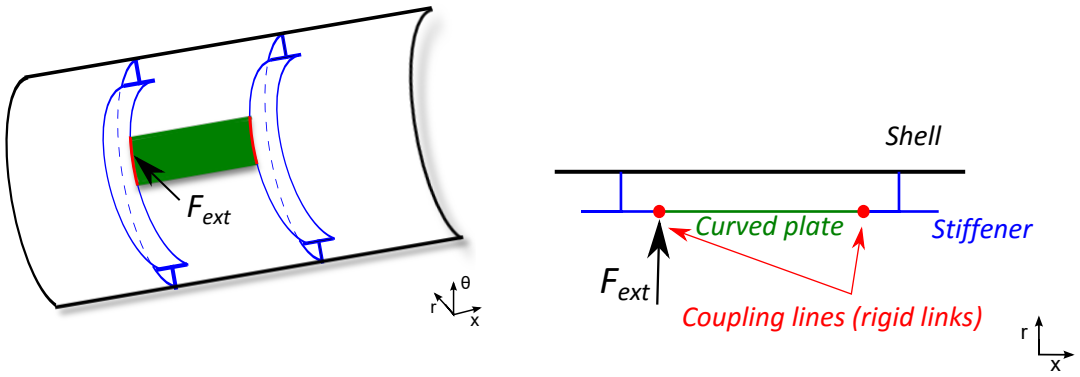

(a) (b)

Figure 25: Cylindrical stiffened shell with a non-axisymmetric internal structure. (a) 3D-view of a section. (b) Section in the plane $\theta = 0$.

The length of the gate functions used as condensation functions matches the criterion proposed in Eq. (54) up to 1 kHz. At this frequency, the flexural wavelength of a 15 mm thick plate is $\lambda_f = 0.38$ m. As the curvature increases the stiffness of the plate, the wavelength at a given frequency increases as well, and the criterion is more restrictive than it could be. The junction is on a circular arc of radius 4.8 m. Thus, 10 gates per junction, of angular length $\theta_S = 0.0417$ rad (equivalent to a curvilinear length of $L_S = 0.2$ m) are considered to ensure good convergence up to 1 kHz.

On one hand, the CTF for the axisymmetric system are calculated using CAA as explained in the previous section. On the other hand, the non-axisymmetric plate is modeled by FEM. The responses are estimated by modal superposition including residual modes and its CTF are calculated by projection on the condensation functions.

3.3.2 *Results*

The frequency response of the velocity in the radial direction at the excitation point and the mean quadratic velocity on the outer surface of the shell are given in Fig. 26. On a finite cylindrical shell, the mean quadratic velocity $< \dot{W} >$ is defined as:

$$< \dot{W} >^2 = \frac{1}{S} \int_{x=0}^{L} \int_{\theta=0}^{2\pi} |\dot{W}(x,\theta)|^2 \mathrm{d}x R \mathrm{d}\theta \tag{67}$$

with $S = 2\pi RL$ the outer surface of the cylindrical shell. The values are given as a function of frequency between 100 and 600 Hz for the reference case of the whole system calculated by FEM and for the CTF method presented here. The high frequency limit is set to 600 Hz in order to calculate the FEM reference solution more easily. The black dotted lines are the responses of the axisymmetric system (*i.e.* the stiffened shell without the plate) calculated by FEM. The blue dashed lines are the results of the CTF method that couples the stiffened shell described by CAA with the plate described by FEM. They are to compare with the references calculated by FEM and plotted in red solid lines. For the velocity plotted in Fig. 26a, a gray dotted line with cross markers represents the results of the CTF method where the stiffened shell admittances are calculated by FEM. It shows that this curve fits very well with the reference, whereas some differences can be seen with the CTF method using CAA. These differences can be explained by the fact that the CAA is, as all numerical methods, only an approximation of the physical phenomena and can lead to slight deviations. Different parameters can be tuned to refine the results (as for example the maximum number of circumferential orders or the definition of the longitudinal wavenumber space) in exchange for higher computational cost. However, these results show that the CTF method is able to get close to the reference calculation and is thus validated for this case.

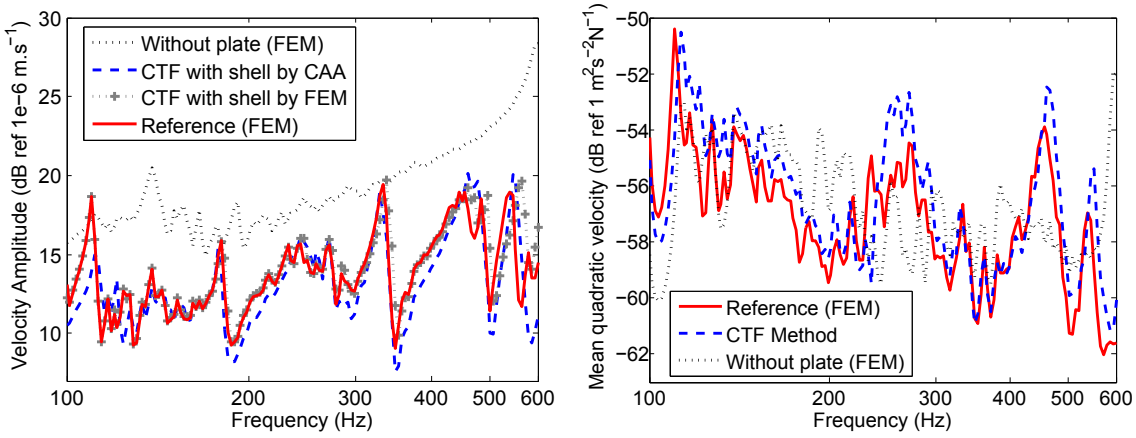

(a) (b)

Figure 26: (a) Radial velocity amplitude (dB ref 10^{-6} m.s^{-1}) of the excitation point as a function of the frequency. (b) Mean quadratic velocity (dB ref 1 m^2.s^{-2}) as a function of the frequency.

3.4 VIBROACOUSTIC BEHAVIOR OF A NON-AXISYMMETRIC SUBMERGED SHELL

3.4.1 *Description of the system*

In this section, the CTF method is applied to a submerged test case. The case considered is shown in Fig. 27 and consists of a 5 m radius, 42.3 m length and 30 mm thick cylindrical shell stiffened with 51 stiffeners and 2 spherical bulkheads (10 mm thick, 30 m curvature radius). There are three different types of stiffeners and their spacing varies between 0.6 and 1 m. The whole system is made of steel ($\eta = 0.02$) and is immersed in water. Clamped boundary conditions are used at the ends of the shell, 2 m away from the first and the last stiffeners. Non-axisymmetric internal frames are added between frames 13 and 19. They are composed of 6 identical curved plate, with the same dimensions as in section 3.3 (2 m long with a curvature radius of 4.8 m, 0.8 m wide and 15 mm thick). A point force is applied on frame 18 at the junction between the flange and the web. The plates and the excitation are chosen so that the system remains symmetric with regard to the plane $\theta = 0$.

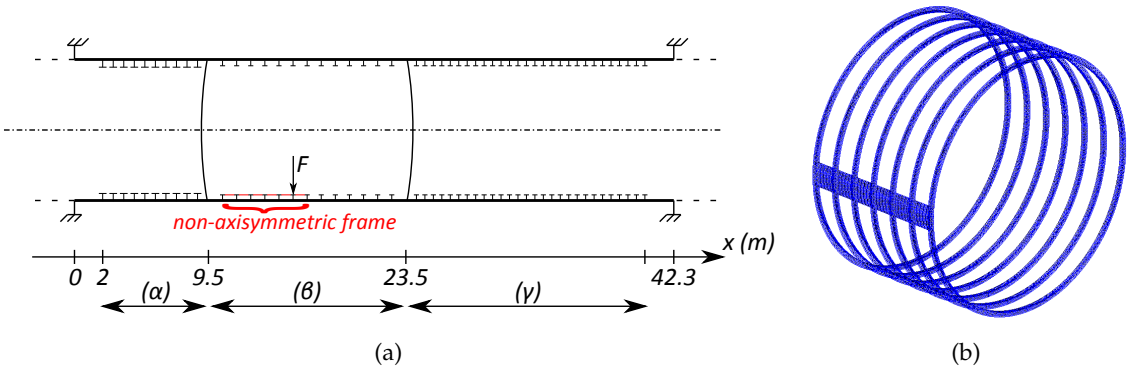

(a) (b)

Figure 27: Submerged hull. Cylindrical shell: 5 m radius, 42.3 m length, 30 mm thick. Axisymmetric stiffeners: (α) spacing 0.75 m, T-cross-section (mm): $300 \times 60/60 \times 300$; ($\beta$) spacing 1 m, T-cross-section (mm): $200 \times 15/15 \times 200$; ($\gamma$) spacing 0.6 m, T-cross-section (mm): $200 \times 25/15 \times 200$. (a) Section in the plane $\theta = 0$. (b) Non-axisymmetric part (without the cylindrical shell).

The only difference with the validation case presented in the previous subsection lies in the shell admittance calculation, which accounts, in the submerged case, for the heavy fluid loading. There are 12 line junctions, which are each divided in 10

segments, resulting in a set of 120 condensation functions. The admittances for a radial displacement in response to a radial force projected on these condensation functions are plotted in Fig. 28 at $f = 1000$ Hz. In Fig. 28a, the 12 diagonal blocks show the admittance amplitude when the displacements and forces are on the same junction, and have thus the biggest amplitudes. As there are 10 gate functions per junction, these blocks have a size of 10×10, and one of them is circled in black. Every other block of the diagonals above and below the main one also has an important amplitude, due to the fact that the junctions are on the same T-cross-section stiffener. There are 10 of these extra-diagonal blocks with a higher amplitude and one of them is circled in white. One can also see that the amplitude decreases with the distance to the excitation along the shell. In Fig. 28b, it shows that only diagonal blocks linking two consecutive junctions have non-null values because the non-axisymmetric internal frames are uncoupled one from the other.

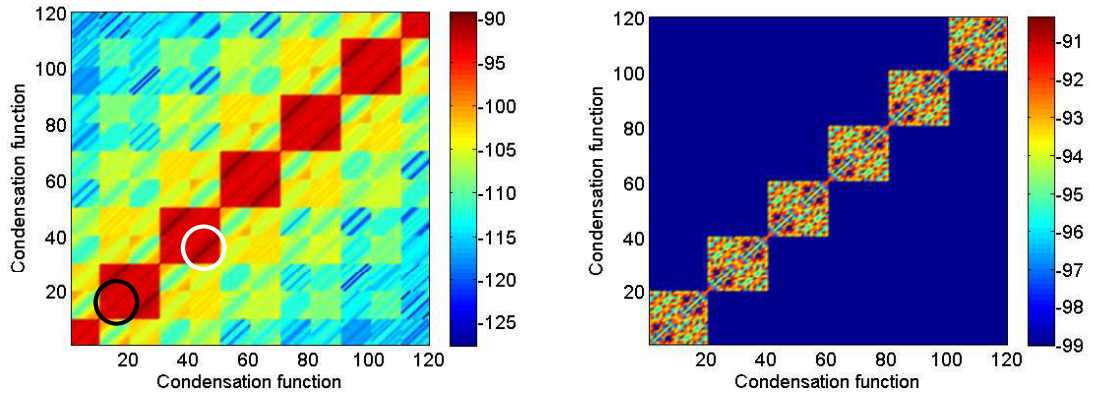

(a) (b)

Figure 28: Amplitude of the admittance (T_r, F_r) (dB ref 1) at $f = 1000$ Hz of the (a) axisymmetric shell (the black circle shows a diagonal block and the white circle shows an extra-diagonal block) and the (b) non-axisymmetric internal frames.

3.4.2 *Results and discussion*

The mean quadratic velocity averaged on the outer surface of the shell, as defined in Eq. (67), is plotted as a function of the frequency in Fig. 29a. To describe properly

the resonance peaks, 400 values are logarithmically spread over the frequency domain between 100 and 1000 Hz (see appendix B). It shows that the non-axisymmetric internal frames have a weak influence on the mean quadratic velocity. Nevertheless, it can be said that a slight apparent damping effect appears, as predicted by the theory of fuzzy internals by Soize [63]. The amplitude of the peaks of the mean quadratic velocity between 350 and 600 Hz is indeed lower in the non-axisymmetric case than in the axisymmetric case. The radiation efficiency σ, as defined in Eq. (6), is plotted on Fig. 29b.

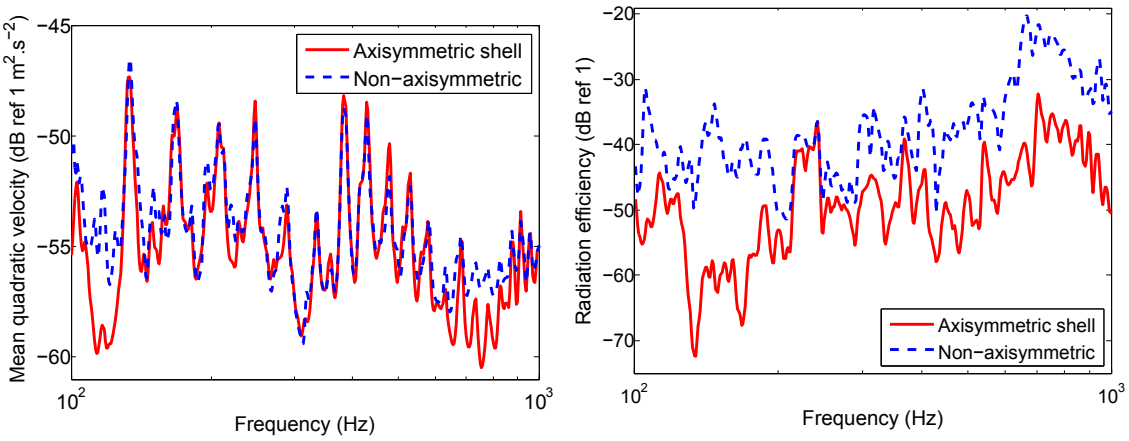

(a) (b)

Figure 29: Frequency responses of the system excited by a radial point force, with and without the non-axisymmetry: (a) Amplitude (dB ref 1 $m^2.s^{-2}$) of the mean quadratic velocity on the outer surface of the shell. (b) Radiation efficiency (dB ref 1).

To explain these differences in the radiation efficiency, although the mean quadratic velocity is only slightly changed, a wavenumber analysis is done [178]. The shell radial acceleration level at $f = 1000$ Hz is plotted in the wavenumber space in Fig. 30 for the two configurations (with and without the plates). As the problem is symmetrical, the variables are even functions of the circumferential orders and thus only the positive circumferential orders have been plotted. The white line shows the radiation circle (elliptical in Fig. 30a and c due to the plotting aspect ratio), defined by:

$$\left(\frac{n}{R}\right)^2 + k_x^2 = \left(\frac{2\pi f}{c_0}\right)^2 \tag{68}$$

The radiation circle represents the supersonic acoustic domain, in which the components radiate to the far-field for a flat plate. The radiation circle remains also a good

indicator for localizing the radiating waves of a shell having a low curvature. On the overall plot, it can be seen that adding the plates has little influence on the highest values of the acceleration spectrum in the wavenumber space (in red in Fig. 30a,c). This indicates that the most contributing waves in terms of the vibration energy propagation on the shell are globally the same for the two cases. It results in few changes on the mean quadratic velocity, as shown in Fig. 29a. Nevertheless, when zooming in on the radiation circle, one can observe that the components (which amplitudes are clearly lower than the highest values outside the circle) are significantly influenced by the plates (see Fig. 30b,d). As these components radiate sound efficiently, it explains the difference in the radiation efficiency observed in Fig. 29b. In general, an axisymmetric shell is not an efficient radiator, but it can be seen that breaking the axisymmetry by adding 3D internal structures increases the radiation efficiency. This trend can be explained by the fact that the non-axisymmetric frames couple circumferential orders together. These results are consistent with the literature [164, 167].

The radial displacements for the submerged stiffened shell, with and without added plates, are presented in Fig. 31. The results are given at 1000 Hz and the values are normalized to the highest displacement amplitude for each plot. In Fig. 31a and Fig. 31c, the excitation is radial while in Fig. 31b and Fig. 31d the excitation is in the longitudinal direction. One can see that adding non-axisymmetric internal frames modifies the vibroacoustic behavior of the stiffened submerged shell. More particularly in this case, the vibrational energy propagates easily in the longitudinal direction due to the strong stiffness of the plates in-plane motion, and is transmitted to the connected stiffeners. Thus, the high displacements are spread further from the point load in the non-axisymmetric cases, especially when the excitation is longitudinal.

In Fig. 32, the far-field sound pressure level at 100 m is plotted at 1000 Hz for the axisymmetric and non-axisymmetric shell. The same color scale is used for the two subplots. The shell is oriented in the same way as in the representation of the shell displacements in Fig. 31. First, consistently with Fig. 29, it is clear that the radiated sound level is higher for the non-axisymmetric case. Then, because of the coupling of different circumferential orders, it can be said that the non-axisymmetric internal frames alter the directivity pattern by increasing its complexity.

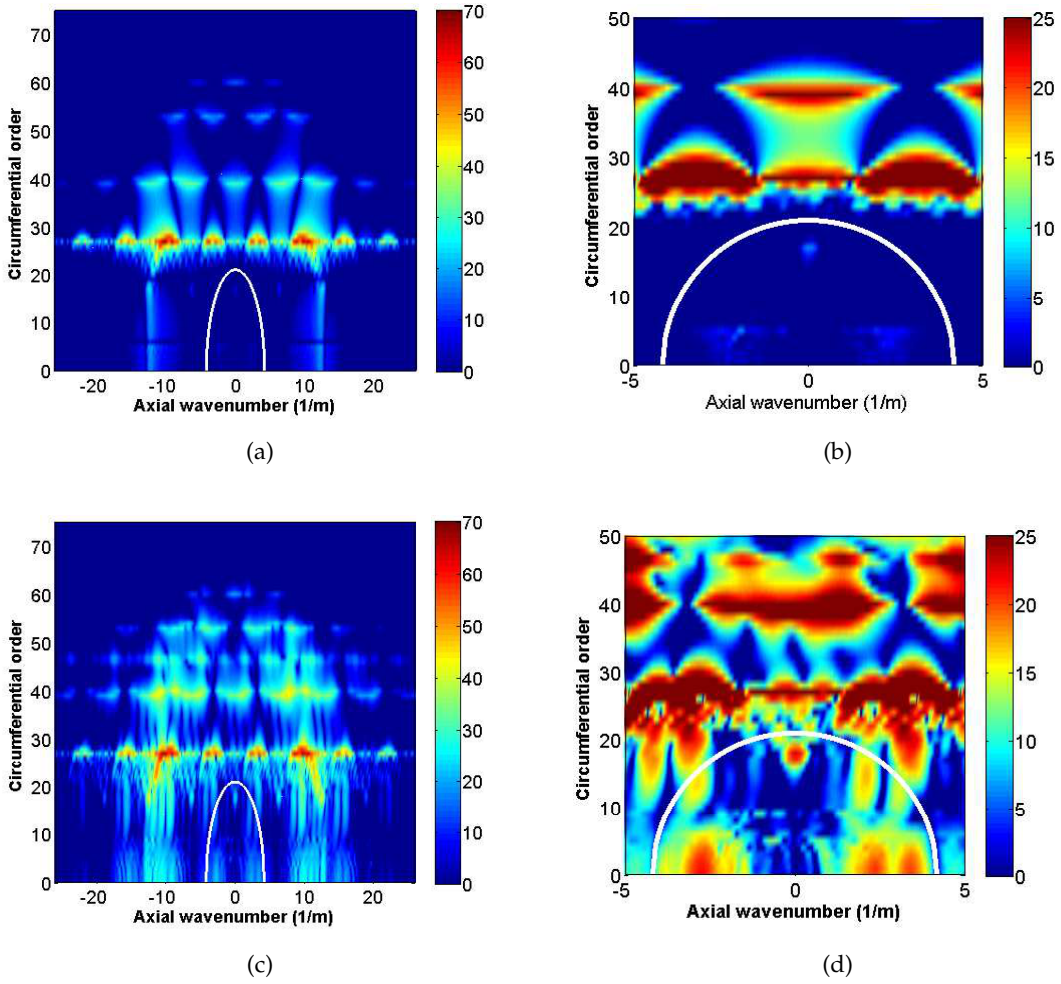

Figure 30: Radial acceleration of the shell (dB ref $10^{-6}g$) in the wavenumber space for a radial unitary force excitation at 1000 Hz. (a) Axisymmetric shell. (b) Axisymmetric shell (zoom on the radiation circle). (c) Non-axisymmetric shell. (d) Non-axisymmetric shell (zoom on the radiation circle).

From a computational point of view, adding these non-axisymmetric internal frames lengthen the calculation by about 60 % in comparison with the axisymmetric stiffened shell. Assuming that the frames admittances used in CAA were already stored in a database and did not need to be calculated again, one frequency for the axisymmetric case was performed in about 75 seconds. Adding the non-axisymmetric internal frames represents thus a difference of about 45 seconds for each frequency of calculation on the computer used for the tests (24 GB RAM, 6 core processors at 2.66 GHz). It is worth noting that the calculation time for the admittances of the non-axisymmetric internal

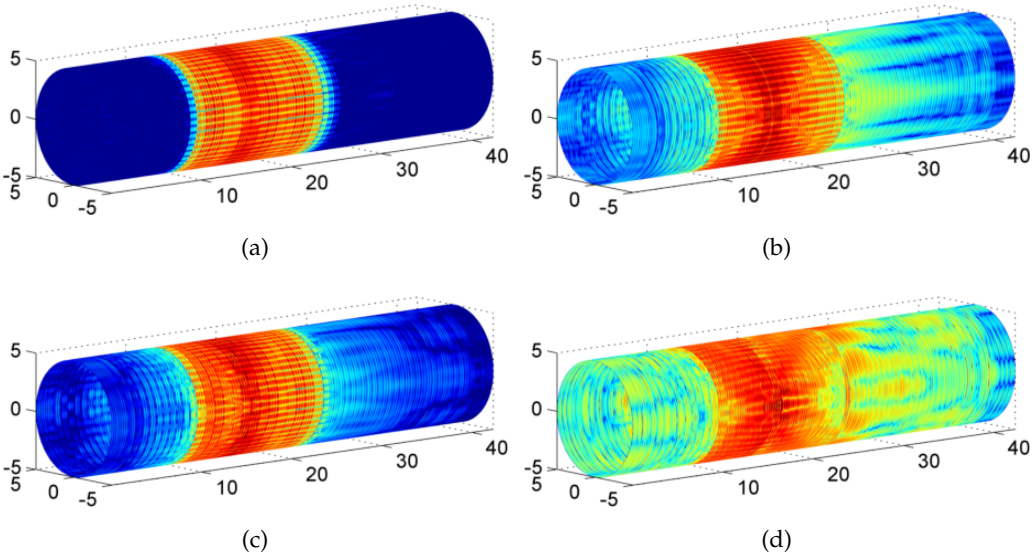

(a) (b)

(c) (d)

Figure 31: Radial displacements level (dB ref $10^{-6}g$) normalized to the maximum value (for each load case) of the cylinder to a harmonic unitary force excitation at 1000 Hz. (a) Axisymmetric shell for radial excitation. (b) Axisymmetric shell for longitudinal excitation. (c) Non-axisymmetric shell for radial excitation. (d) Non-axisymmetric shell for longitudinal excitation.

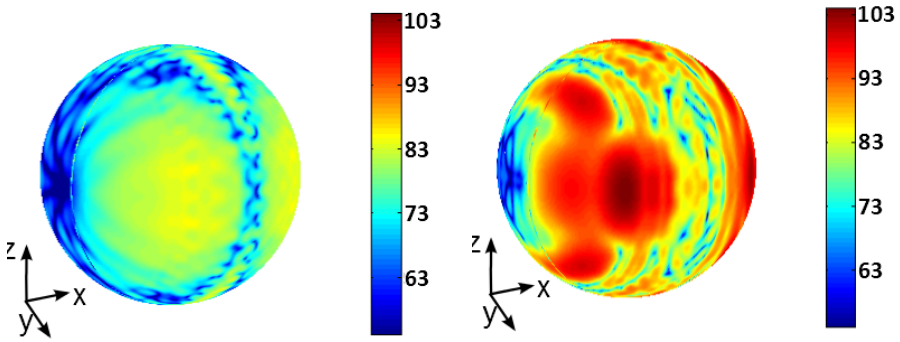

(a) (b)

Figure 32: 3D representation of the far-field sound pressure level at 100 m (dB ref 10^{-6} Pa) of the cylinder to a radial harmonic unitary force excitation at $f = 1000$ Hz. (a) Axisymmetric shell. (b) Non-axisymmetric shell.

frame is short as modal superposition with residual modes is used. It is hard to compare these results to some other numerical methods, because very few of them are able

to predict the behavior of a submerged hull in the considered frequency range, but it can be said that the computational time remains acceptable for practical applications.

3.5 ILLUSTRATION ON AN INDUSTRIAL TEST CASE

To show the versatility of the method, the test case presented in section 3.4 is considered with a different non-axisymmetric internal frame, which is more representative of an industrial application. This structure, which is called a floor, consists in an assembly of plates, made of a horizontal floor, a vertical stiffening plate and two disc sections. All the plates are 1.5 mm thick. The two disc sections are linked to the axsiymmetric submerged stiffened shell on the ring stiffeners at $x = 11.5$ and $x = 21.5$ m, as seen in Fig. 33. It is reminded that the stiffeners are modeled by shell elements, and the contact between the floor and the stiffeners are lines at the junction between the web and the flange (see Fig. 3b for the associated vocabulary).

The two subsystems are made of steel with a structural damping of $\eta = 0.02$. The response is calculated between 100 and 1000 Hz with 400 values logarithmically spread. A model of the internal structure is shown in Fig. 33b, with the colors representing the displacement magnitude of the eigenmode at 170 Hz. The Finite Element model has about 550000 DOF. A modal basis is calculated with NASTRAN in about 6000 s, resulting in 3210 modes up to 1050 Hz. Each of the two junctions between the two subsystems is split in 48 segments of length $L_S = 0.2$ m.

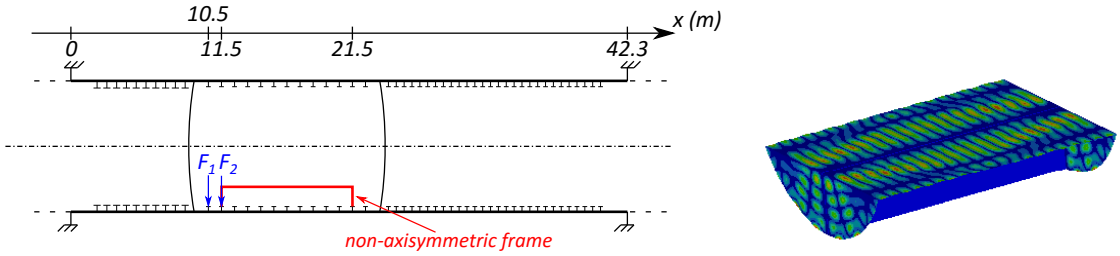

(a) (b)

Figure 33: Submerged cylindrical shell with axisymmetric stiffeners with a non-axisymmetric floor. (a) Section in the plane $\theta = 0$. (b) Mode at 170 Hz of the floor.

Two radial point forces, marked F_1 and F_2 in Fig. 33a, are considered in turns. F_1 is applied on the stiffener at $x = 10.5$ m, on the intersection between the web and

the flange, at $\theta = 0$. F_2 is applied at the junction between the floor and the stiffener at $x = 11.5$ m. The influence of the non-axisymmetric internal frames is examined for these two excitations. The mean quadratic velocities are plotted in Fig. 34. It is clearly seen that the excitation location also plays a role in the influence of the non-axisymmetric internal frame. For the case F_1, where the excitation is not on the junction with the floor, the influence on the mean quadratic velocity is weak. On the contrary, for the case F_2 the mean quadratic velocity is about 20 dB smaller in the non-axisymmetric case. This phenomena can be explained by looking at the injected power.

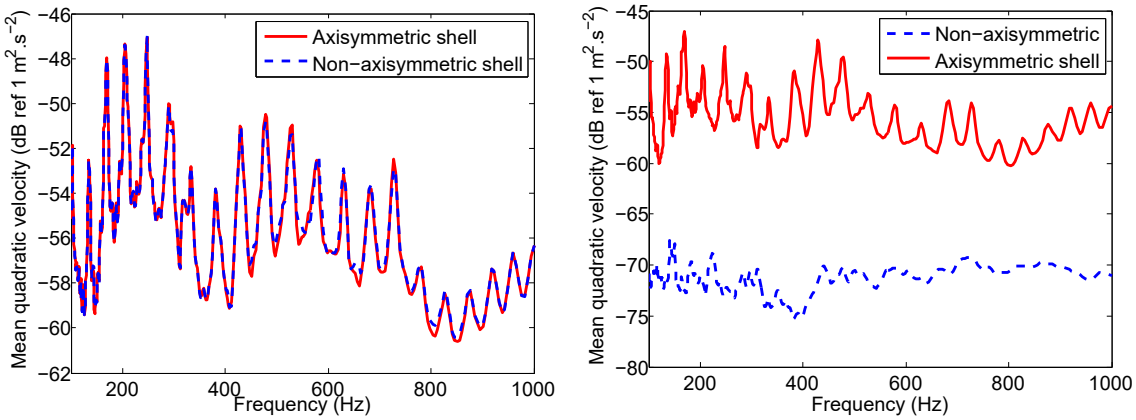

(a) (b)

Figure 34: Amplitude (dB ref 1 $m^2.s^{-2}$) of the mean quadratic velocity on the outer surface of the shell, with and without the non-axisymmetric floor: (a) radial point force F_1, (b) radial point force F_2.

The injected power P_{inj} is calculated at the excitation point as follows:

$$P_{inj} = \frac{1}{2}\Re(F\dot{W}^*) \tag{69}$$

where $\Re$ denotes the real part and F and $\dot{W}$ are respectively the complex force and velocity at the excitation point. The injected power can be expressed as a function of the self-admittance at the excitation point $Y = \frac{\dot{W}}{F}$:

$$P_{inj} = \frac{1}{2}|F|^2\Re(Y) \tag{70}$$

The injected power for all the cases is plotted as a function of the frequency on Fig. 35. It is shown that for the case of the excitation F_1, the floor has a weak influence on the injected power. However, when the excitation is at the junction with the floor, the

injected power drops dramatically. This is explained by the fact that the local stiffness is largely increased because of the floor and the velocity at this point is thus much smaller.

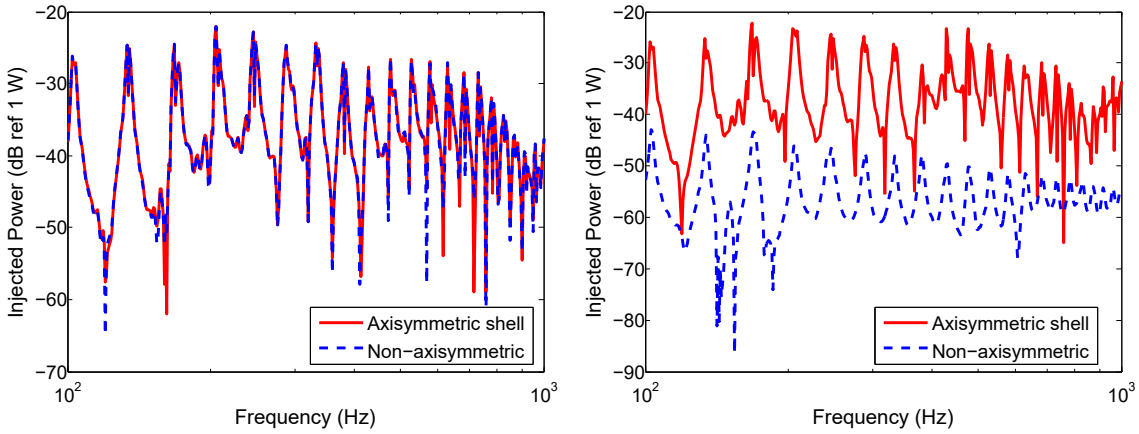

Figure 35: Injected power (dB ref 1 W) into the system with and without the non-axisymmetric floor: (a) radial point force F_1, (b) radial point force F_2.

The increase in stiffness due to the floor is illustrated in Fig. 36. The point admittance in the radial direction at the point in the middle of the first junction, *i.e* in $(x, r, \theta) = (11.5, 4.8, 0)$, is plotted as a function of the frequency for the two subsystems isolated. It shows that the floor is much stiffer than the stiffened submerged cylindrical shell. This can be explained by the fact that two perpendicular plate components of the floor have in-plane excitations in this case.

The radiation efficiency of the stiffened submerged cylindrical shell with and without the floor is plotted as a function of the frequency in Fig 37. The trend discussed previously in section 3.4 is also verified through this example: the non-axisymmetries tend to increase the radiation efficiency. It is however worth noting that the radiation efficiency is not an intrinsic value of a system and depends on the excitation point. On the present test case, it is shown that the influence of the non-axisymmetric internal frame is much bigger when the excitation is closer to it.

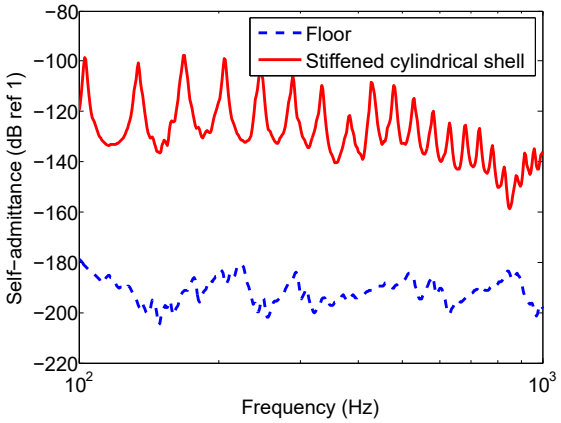

Figure 36: Amplitude of the point admittance (dB ref 1) at the first junction for $\theta = 0$ for the two isolated subsystems.

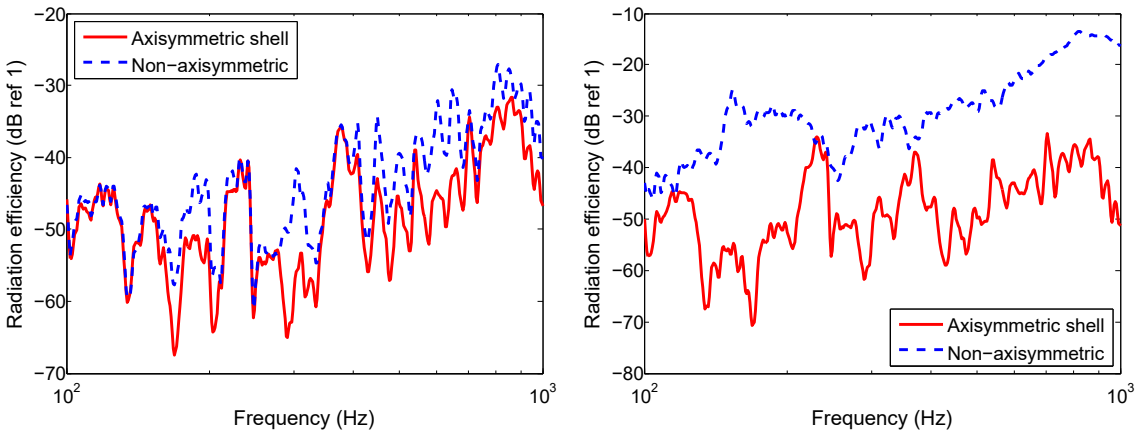

Figure 37: Radiation efficiency (dB ref 1) with and without the non-axisymmetric floor: (a) radial point force F_1, (b) radial point force F_2.

3.6 CONCLUSIONS

CTF calculations using the gate functions have been used to couple together a numerical model of an axisymmetric stiffened shell and finite element models of non-axisymmetric internal frames. An *in vacuo* test case has been considered for validation purpose. It has shown good agreement with FEM results. The proposed method has then been applied to study the influence of non-axisymmetric internal frames on the vibroacoustic behavior of a submerged stiffened shell.

The examples illustrates well the versatility and the interest of this approach for coupling different numerical models (*i.e.* CAA with FEM) and for taking the fluid loading on the cylindrical shell into account easily. From these results, as non-axisymmetries tend to couple circumferential orders together, it can be said that including non-axisymmetric internal frames can alter greatly the vibroacoustic behavior of the cylindrical shell. On these examples, it is clear that they play a key role as they tend to increase the radiation efficiency of the system and can alter the vibrational and acoustic energy distribution. These trends will be checked on an experimental model in the next chapter.

More generally, the present substructuring approach can be used to partition vibroacoustic problems into several subsystems coupled along lines, and can be applied to a wide range of practical problems. Another advantage of this approach is the ability to quickly reanalyze subsystems for optimization. For instance, if one of the subsystems properties is modified, it is not necessary to recalculate the condensed transfer functions of the other subsystems. Computation time can thus be saved by reusing a database of condensed transfer functions.

4

EXPERIMENTAL INVESTIGATION OF THE INFLUENCE OF NON-AXISYMMETRIES ON A MODEL IN AIR

This chapter is based on the article entitled "Vibrations et rayonnement acoustique des coques cylindriques raidies : Étude expérimentale de l'influence des structures internes non-axisymétriques" (in French), published in the proceedings of the *Congrès Français d'Acoustique 2016* in Le Mans, France, in April 2016 [179]

The numerical simulations presented in chapter 3 show that more circumferential orders play a role when the system is non-axisymmetric, and that the radiation efficiency tends thus to increase. The aim of this chapter is to verify this trend experimentally. The experiments are conducted in air, because of cost and time reasons compared to an experiment in water. A scanning vibrometer is used to measure the displacements on the surface of a stiffened cylindrical shell. A study in the wavenumber domain and the stationary phase theorem allow calculating the radiated power in air. The influence of a non-axisymmetric internal frame when the system is excited by a point force is highlighted. Comparison between numerical and experimental results is then discussed.

4.1 PRESENTATION OF THE MEASUREMENT SYSTEM

4.1.1 *Axisymmetric stiffened cylindrical shell*

A stiffened cylindrical shell, which geometrical characteristics are given in table 2, is shown in Fig. 38. The cylindrical shell is made of standard non-alloy steel. For calculations and simulations, common values are considered: $E = 2.1.10^{11}$ Pa, $\rho_s = 7800$ kg.m^{-3} and $\nu = 0.3$. It has 72 identical stiffeners of rectangular cross-section, which have been machined from a thicker cylinder. The cylindrical shell is divided in five sections with three different stiffeners spacings. 15 mm thick caps are screwed at the ends of the cylinder.

Table 2: Stiffened cylindrical shell dimensions (mm).

Parameter	Value
Radius	100
Length	1500
Shell thickness	1.5
Stiffeners height	5
Stiffeners width	1
Stiffeners spacing 1	24
Stiffeners spacing 2	20
Stiffeners spacing 3	17

The ring frequency, as defined in Eq. (5), yields in this case: $f_r = 8657$ Hz. The coincidence frequency defined in Eq. (7) is: $f_r = 7812$ Hz. This stiffened cylindrical shell is referred to as the axisymmetric case.

4.1.2 *Non-axisymmetric internal frame*

In a second case, a non-axisymmetric internal frame is fixed inside the cylinder previously described. As shown in Fig. 39a, it is a floor which is 869 mm long, 64.3 mm high and 170.6 mm wide. It consists in a 1.5 mm thick plate, for which the ends have been cut along a circular arc of radius 98.5 mm, before being bended to form right angles. The contact between the cylindrical shell and the floor is only on these two circular arcs. A square tube of 20 mm wide and 2mm thick in steel is glued under the horizontal part and reinforces the structure lengthwise.

Before placing this structure in the cylinder, it is hanged with flexible strings and an accelerometer is placed at an arbitrary spot in order to measure the frequency response to an impact hammer (shown in Fig. 39b). The transfer function is plotted in Fig. 40. Some of the resonance frequencies can clearly be identified, and some of them will be seen in the response of the coupled system (as for instance 213, 234 and 273 Hz). Besides, the modal damping can be estimated by measuring the peaks width at -3 dB [180]. An averaged structural damping factor of 0.5 % is deduced ($\eta = 0.005$).

(a) (b)

Figure 38: Pictures of the axisymmetric stiffened cylindrical shell: (a) hanged on an arm and (b) interior view.

The floor is placed inside the cylindrical shell, with line contacts along the circumference at $x = 0.315$ m and $x = 1.185$ m. Several constraints need to be taken into account to assemble the two subsystems:

- the displacements continuity should be verified (*i.e.* rigid connection) and no damping (*i.e.* energy dissipation) should be introduced;
- the junction should be strong enough to support the floor when the cylindrical shell is hanged;
- the access inside the cylindrical shell is difficult because of the small radius;
- the process should not damage the cylinder;
- the internal structure could be dismounted once the measurements done.

Tests are done on samples made of two steel plates perpendicularly assembled, as explained in appendix D. Several types of glue, as well as brazing are compared and an acrylic glue with activator (Loctite AA 330) is chosen for this application. A picture of the assembled system is shown in Fig. 41a. A camera is used to check the junctions, as seen in Fig. 41b.

(a) (b)

Figure 39: Picture of (a) the non-axisymmetric internal frame and (b) the impact hammer and the acquisition device.

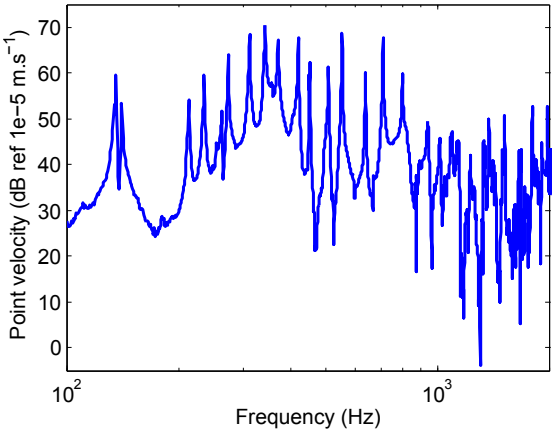

Figure 40: Transfer function between an impact point on the top of the floor and an accelerometer placed on the side.

4.1.3 *Experimental setup*

As shown in Fig. 42, the system is hanged vertically on an arm using a strap, in order to limit the transfer of vibrations. A rotating platform allows to rotate the cylindrical shell around its axis and precisely identify the angles (see Fig. 43a). A 12.5 mm diameter patch is glued on the outer surface of the cylindrical shell, and screwed to a shaker. The shaker is hanged on the rotating platform in order to excite always the same point of coordinate $(x, r, \theta) = (1.195, 0.1, 0)$ in the cylindrical system (with $x = 0$ at the bottom of the cylindrical shell). This excitation point is located at the bottom of a stiffener, and lies at 10 mm from one of the floor junctions in the non-axisymmetric configuration.

(a) (b)

Figure 41: (a) Interior view of the stiffened cylindrical shell with the non-axisymmetric internal frame. (b) Partial view of the junction between the two subsystems using a camera.

Two elements come in between the patch and the shaker: an impedance head that measures acceleration and force at the excitation point, and a threaded rod that limits the moments and allows assuming a radial excitation in the cylindrical system (see Fig. 43b).

The measurements are conducted in a semi-anechoic room (8.6 m long, 6.4 m wide, 4 m high and 80 Hz cut-off frequency). The floor is considered to be infinitely rigid and a 175 mm space separates it from the bottom of the cylinder. The laser vibrometer is placed 2.68 m far from the cylindrical shell's surface. The vibrometer scans the cylinder from down to up along a single generating line. A microphone array composed of 6 microphones with a 0.3 m spacing is placed 1 m far from the cylindrical shell's surface. The vibrometer, the cylindrical shell and the microphone array are aligned in this order, as seen in Fig. 43c. The experiment consists in keeping the vibrometer and the microphone array at fixed positions while rotating the set cylindrical shell-shaker.

The aim is to measure the radial vibrations on the outer surface of the cylindrical shell and the radiated pressure at some points, for the two configurations, that means with and without the non-axisymmetric internal frame. The measurements are made up to 16 kHz for the vibrometer and 12.8 kHz for the microphones and the impedance head. The excitation is a chirp (swept-frequency sine), and the output is the transfer function with regard to the force, calculated on 20 averages. In order to examine the

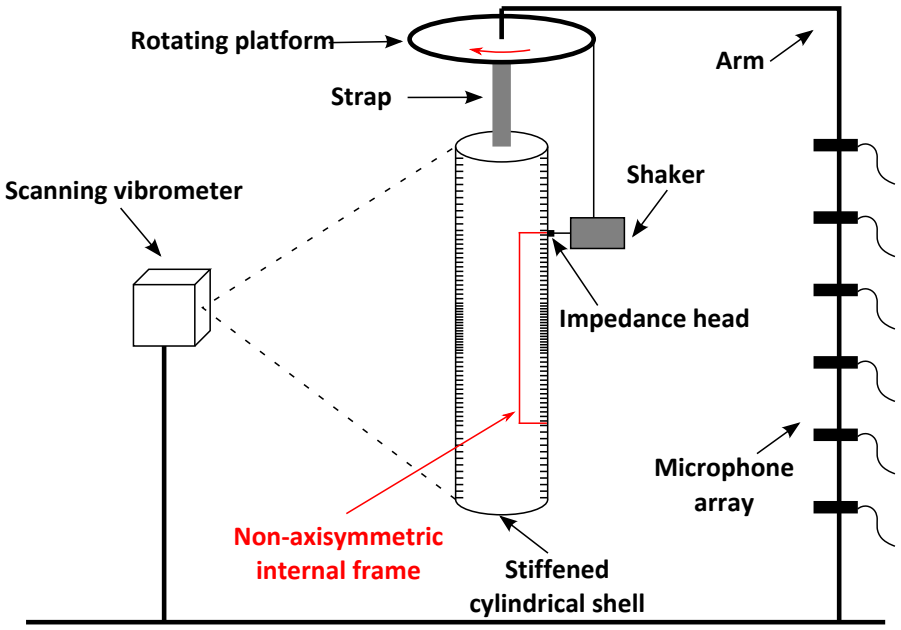

Figure 42: Sketch of the experimental setup.

vibrations results in the wavenumber domain, the scanning grid is defined as a function of the sampling wavenumber k_s, defined so that $k_s = 2k_f$, where k_f is the flexural wavenumber of an equivalent plate (in steel, of thickness $h = 1.5$ mm) at the highest frequency [8]:

$$k_f = \left(\frac{2\pi f_{lim}}{h} \sqrt{\frac{12\,(1-\nu^2)\,\rho_s}{E}} \right)^{1/2} \tag{71}$$

The maximum distance d_{max} between two consecutive measurement points is then:

$$d_{max} = \frac{2\pi}{k_s} \tag{72}$$

For $f_{lim} = 16$ kHz, the numerical application yields $d_{max} = 15$ mm. A scanning line with 101 points along the cylinder is thus defined. The maximum angle θ_{max} between two consecutive measurements is given by the same criterion:

$$\theta_{max} = \frac{2\pi}{k_s R} \tag{73}$$

The present case gives $\theta_{max} = 9°$. The system being symmetric, it is sufficient to measure between 0 and 180°. The experiment consists thus in 21 linear scans, where the system is successively rotated by 9°.

(a) (b)

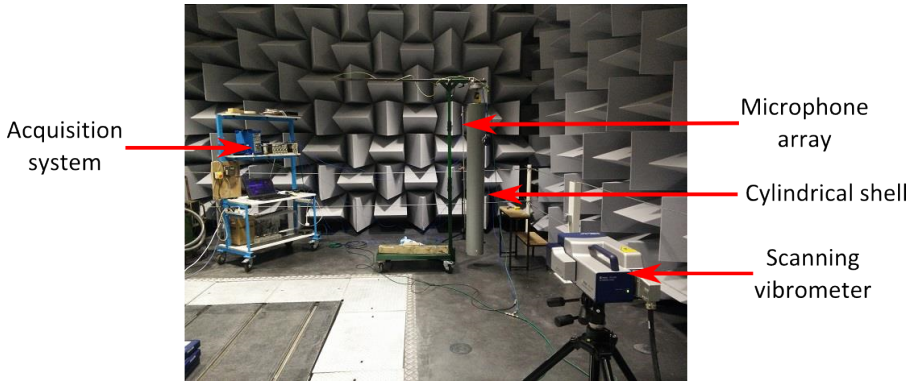

(c)

Figure 43: (a) Top view of the rotating platform. (b) Patch - impedance head - threaded rod - shaker. (c) Picture of the experimental setup

4.2 INFLUENCE OF THE INTERNAL STRUCTURE

4.2.1 *Mean quadratic velocity*

The mean quadratic velocity, as defined in Eq. (67) is plotted as a function of the frequency in Fig. 44 for the axisymmetric case. Only the frequency range between 0 and 2500 Hz is shown in this plot in order to clearly see the resonance peaks. By looking at the velocity repartition on the surface of the cylindrical shell for the resonance peaks, one can notice that the circumferential modes appear by groups. This phenomenon is linked to the fact that there is a cut-off frequency below which the circumferential orders cannot appear, as explained in [181] and on the dispersion curves in section 4.2.3.

The breathing mode $n = 0$ appears at the ring frequency, out of the frequency range shown here. The plot in Fig. 44 allows also to estimate qualitatively the number of resonances in the frequency range considered, which appears weak in comparison with the number of resonance peaks for the isolated non-axisymmetric internal frame (*cf.* Fig. 40).

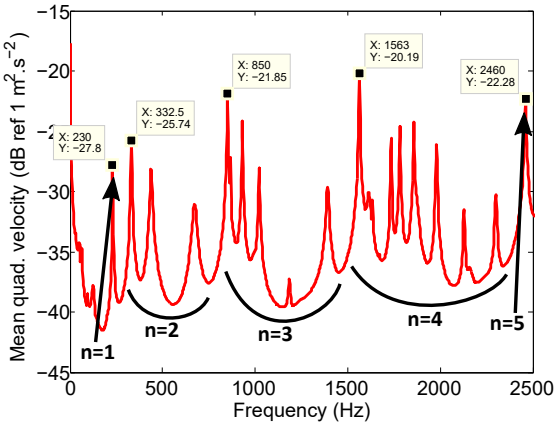

Figure 44: Mean quadratic velocity as a function of the frequency for the axisymmetric stiffened cylindrical shell.

The comparison of the mean quadratic velocities for the two configurations (with and without the non-axisymmetric internal frame) is plotted as a function of the frequency in Fig. 45. The first observation is that the vibration level is lower in the non-axisymmetric case, in particular above 500 Hz. The cylindrical shell and the internal structure have the same thickness and are made from the same material. It can thus be said that the impedance is adapted between the two subsystems. Besides, the modal density of the internal structure is higher than the one of the cylindrical shell. The combination of these two elements leads to an apparent damping effect, as explained in the fuzzy internal theory [63, 64]. Moreover, new resonance peaks can be observed, in particular between 200 and 500 Hz. The peaks frequencies are directly linked to the floor resonance (*cf.* Fig. 40).

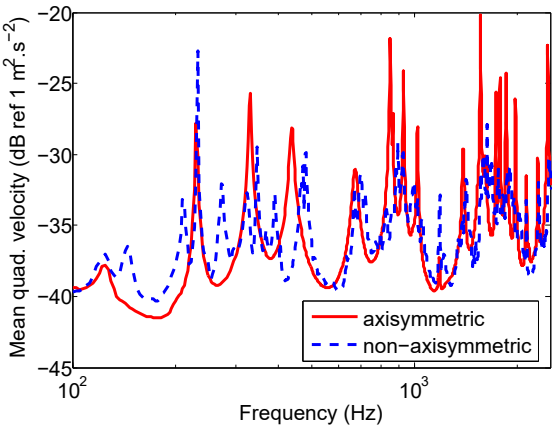

Figure 45: Comparison of the mean quadratic velocities for the two configurations.

4.2.2 *Maps of the radial vibratory field*

The velocity cartographies on the outer surface of the cylindrical shell are plotted in Fig. 46 for the two configurations, at $f = 1980$ Hz and $f = 3580$ Hz. The plots are functions of the tangential coordinate θ in abscissa and the axial coordinate x in ordinate. The excitation is placed in $\theta = 0$ and $x = 1.195$. A spot of low velocities can be seen around the excitation, because the vibrometer cannot scan the surface behind the shaker. At $f = 1980$ Hz, the mode $(m, n) = (8, 4)$ is observed for the axisymmetric case, where m is the longitudinal modal index and n the circumferential order. Adding the non-axisymmetric internal structure has two main influences on the cartography at this frequency: the amplitude decreases and the nodes of vibrations are modified.

At $f = 3580$ Hz, it can be seen that the point force mainly excites the area close to the excitation point in the axisymmetric case (Fig. 46c). One of the possible explanation is that the cylindrical shell has sections with different rib spacings. It is known that in a regularly stiffened structure, pass or stop-bands can be seen. They describe respectively frequency ranges where the structural waves are propagative or evanescent [182, 183]. In the non-axisymmetric case (Fig 46d), the energy can be transmitted through the internal structure to the other end of the cylinder, where the rib spacing is the same than in the section which is excited. The vibrations in the area in the middle of the cylinder are also modified because of the internal structure. This phenomenon can

be related to what Maidanik and Dickey called amber-bands [184, 185], which is a transition between pass-bands and stop-bands.

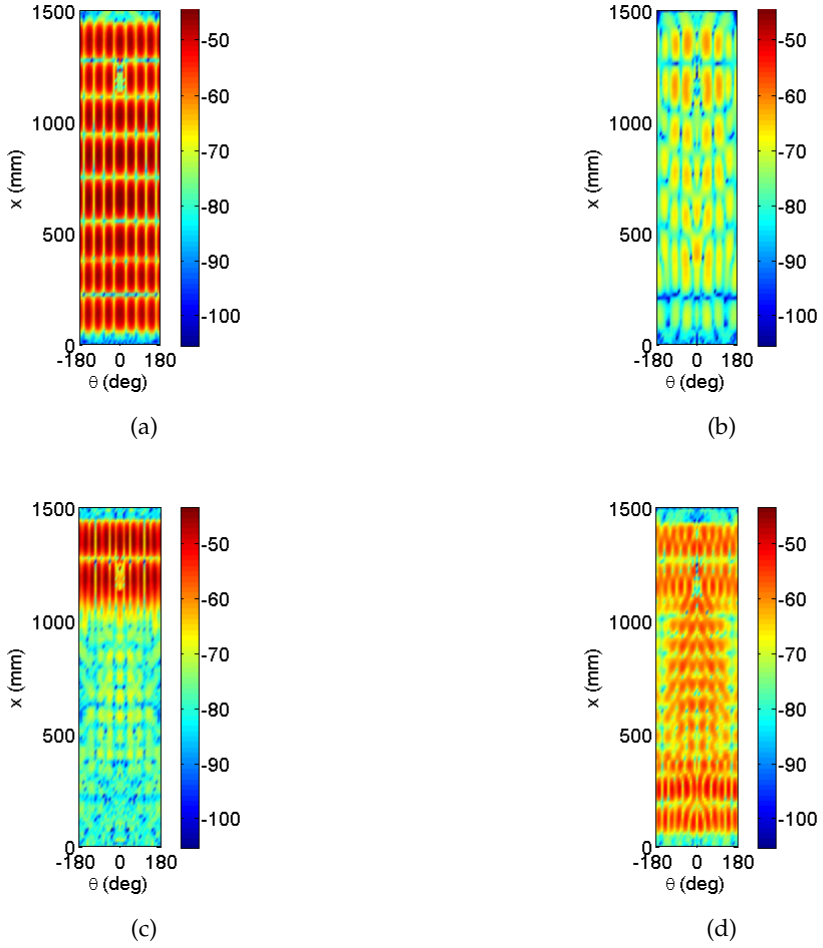

Figure 46: Map of radial velocities (dB ref 1 m.s^{-1}) on the outer surface of the cylindrical shell. (a) Axisymmetric case at $f = 1980$ Hz. (b) Non-axisymmetric at $f = 1980$ Hz. (c) Axisymmetric case at $f = 3580$ Hz. (d) Non-axisymmetric at $f = 3580$ Hz.

A 2D Fourier transform is applied to represent the velocities in the wavenumber domain. In practice, as the velocities have been measured on a grid, the integrals of Eq. (4) are proportional to the sum of all the points on the grid. The grid definition in the physical space determines the definition of the wavenumber domain [186]. We already know, thanks to Eqs. (72) and (73), that the maximal wavenumber that can be

calculated is linked to the grid resolution in the physical space. Similarly, the resolution in the wavenumber domain δk_x and δn is linked to the maxima in the physical space:

$$\delta k_x = \frac{2\pi}{L} \simeq 4.2 \tag{74}$$

$$\delta n = \frac{2\pi}{2\pi} = 1 \tag{75}$$

The system being 2π-periodic, $\tilde{\tilde{W}}(k_x, n) = 0$ if $n \notin \mathbb{Z}$. The radial velocities in the wavenumber space are plotted for the two configurations and the two frequencies in Fig. 47. In each plot, the amplitude has been normalized to the highest value in order to compare the repartition of the radial velocities in the wavenumber space. At $f = 1980$ Hz, the amplitude maxima appear in the axisymmetric case at the wavenumbers corresponding to the modal wavenumbers. The circumferential order $n = 4$ is playing a leading role in this case. In the non-axisymmetric case, more circumferential orders play a role, especially in the low circumferential orders. If the problem is decomposed on a modal basis, it is equivalent to say that the non-axisymmetry tends to couple the circumferential orders [156]. The same observations can be made at $f = 3580$ Hz in Fig. 47c and 47d.

The radiation circle (see Eq. (68)) is plotted in white on the plots in Fig. 47. The components inside this circle are the main contributors to the far-field radiated pressure [178]. It can be noticed that these components have a higher level in the non-axisymmetric case. The radiation efficiency is thus expected to increase at these frequencies, as shown in section 4.2.4.

4.2.3 *Operational dispersion curves*

Operational dispersion curves are constructed by using a spatial 2D Fourier transform of the experimental radial displacements on the surface of the cylindrical shell. For each frequency and each axial wavenumber, the maximum value of the spectral radial displacements on all circumferential orders is selected. The plots in Fig. 48 show the dispersion curves for the axisymmetric and the non-axisymmetric case. For each frequency, the amplitude is normalized to the highest value. According to Eq. (75), the axial wavenumber resolution is $\delta k_x \simeq 4.2$. However the zero-padding technique [187] is used to increase this resolution and have clearer plots. It consists in adding fictive

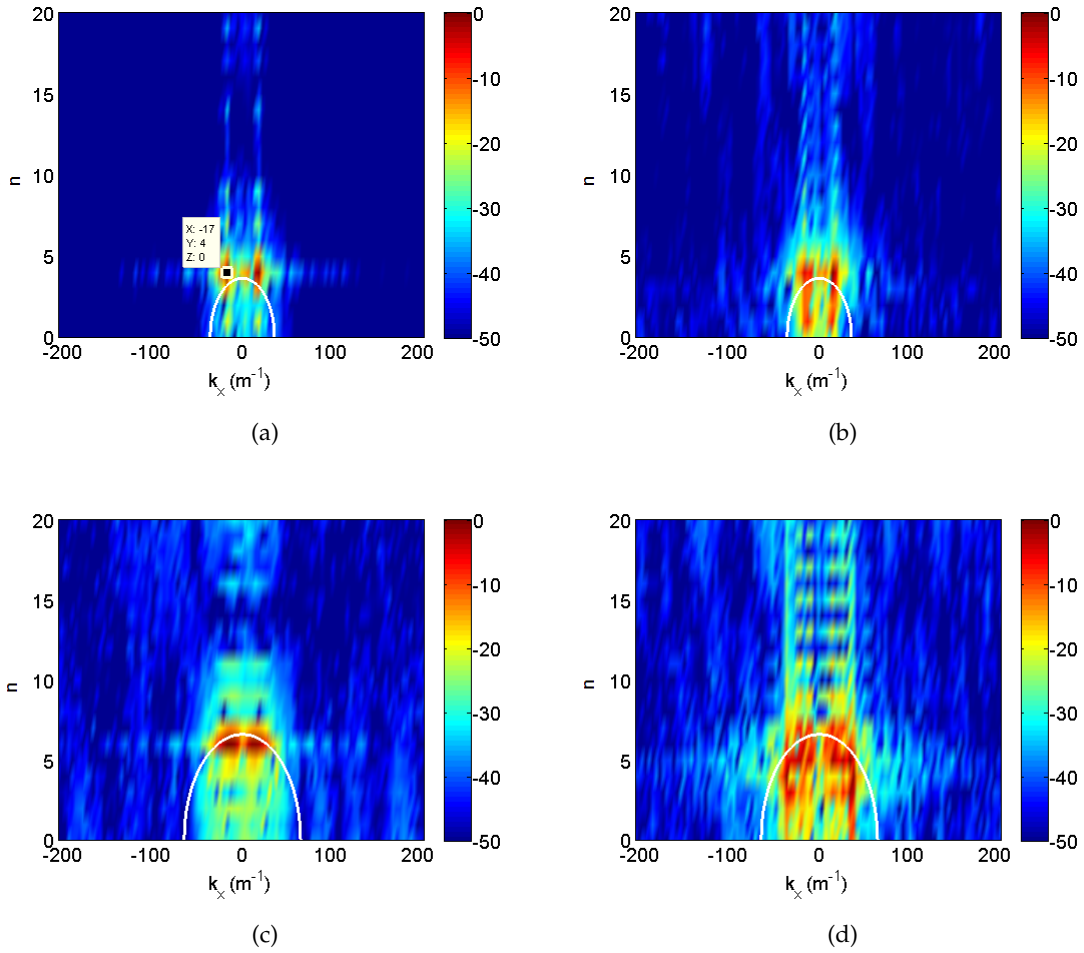

Figure 47: Map of radial velocities (dB ref 1 m.s^{-1}) in the wavenumber domain (k_x, n). (a) Axisymmetric case at $f = 1980$ Hz. (b) Non-axisymmetric at $f = 1980$ Hz. (c) Axisymmetric case at $f = 3580$ Hz. (d) Non-axisymmetric at $f = 3580$ Hz.

displacements set to zero outside the interval $[0, 1.5]$. For the plots presented here, the axial wavenumber resolution is taken equal to $\delta k_x = 1$.

Several results can be read on this curves, where each trajectory corresponds to a circumferential number [188, 189]. First of all, the ring frequency (see Eq. (5)) is represented by a vertical white solid line. It shows the limit between two domains:

- a low frequency domain where all the flexural, shear and compressional waves are coupled and the dispersion curves are S-curves;

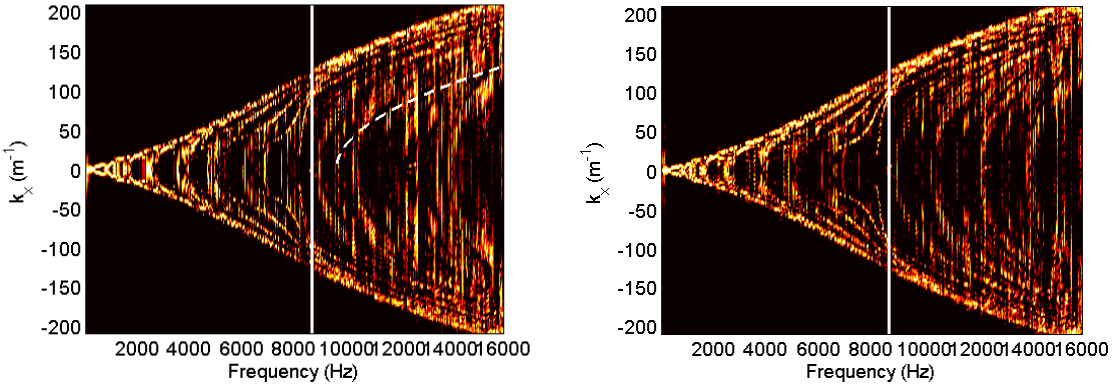

Figure 48: Operational dispersion curves plotted from the radial displacements in the (a) axisymmetric case and the (b) non-axisymmetric case.

- a high frequency domain where the effect of curvature is negligible and the flexural movements are decoupled from the shear and compressional movements. The dispersion curves are similar to the case of a plate and have a square-root shape.

Above the ring frequency, the axial wavenumber k_x can thus be linked to the flexural wavenumber k_f in an equivalent plate by the following relation:

$$k_x = \sqrt{k_f^2 - \left(\frac{n}{R}\right)^2} \tag{76}$$

k_x can be expressed as a function of the frequency using Eq. (71). It is plotted for $n = 16$ by a white dashed line in Fig. 48a. It can be seen that the behavior of the cylinder above the ring frequency is indeed similar to the one of an equivalent plate.

A cut-off frequency for the apparition of the circumferential orders can also be seen. As each curve represents a circumferential order, the lowest frequency where a circumferential order appears can thus directly be read on the plots. This is more clearly seen in Fig. 49, where the circumferential order $n = 6$ is isolated. In the axisymmetric case, the cut-off frequency for the 6^{th} circumferential order is then around 3500 Hz (represented by the white dashed line).

The differences between the axisymmetric and the non-axisymmetric case are difficult to see on the plots of Fig. 48. One of the possible reasons is that because of the curvature, the cylindrical shell is stiffer than the internal structure, especially below the

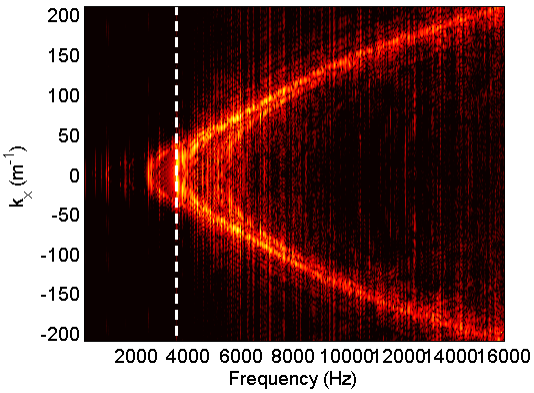

Figure 49: Experimental operational dispersion curves for $n = 6$ plotted from the radial displacements in the axisymmetric case with the cut-off frequency at around 3500 Hz (white dotted line).

ring frequency. Hence, the dispersion relation of the waves propagating in the cylindrical shell is not strongly modified. However, by taking a closer look on the $k_x = 0$ axis, it can be seen that the trajectories appear less clearly when there is the non-axisymmetric internal structure. It could be interesting to run the experiments at higher frequencies (high above the ring frequency) to see if the internal structure has more influence.

4.2.4 *Radiated pressure and power*

The microphone array measures the pressure in 6 points in the axial direction, for each angle. It is thus equivalent to a single measurement with microphones placed all around the cylindrical shell, as shown in the sketch in Fig. 50 where the microphones are marked by crosses. 3D cartographies of the radiated pressure by the microphones can thus be plotted, as seen in Fig. 51 for $f = 1980$ Hz. On these plots, the pressure is represented in dB by the colors and the distance to the axis. It is important to note that the microphones measure also the reflections on the concrete floor, located at 0.175 m from the lowest microphone. The influence of the non-axisymmetric internal frame can be seen, as the pressure level drops. However, these measurements are not satisfactory, because the axial microphone resolution is too low with regards to the acoustic wavelengths ($\lambda = \frac{c_0}{f} \simeq 0.17$ m at $f = 1980$ Hz, with $c_0 = 340\text{m.s}^{-1}$ the sound velocity in air).

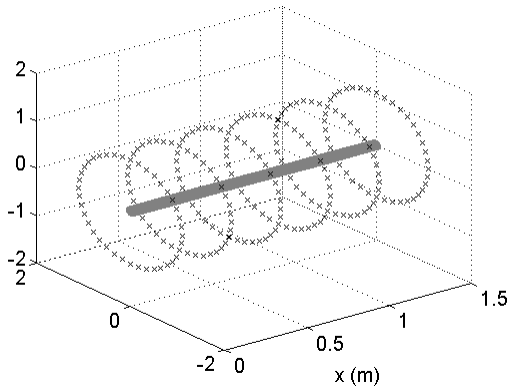

Figure 50: Microphones positions (+) around the cylindrical shell.

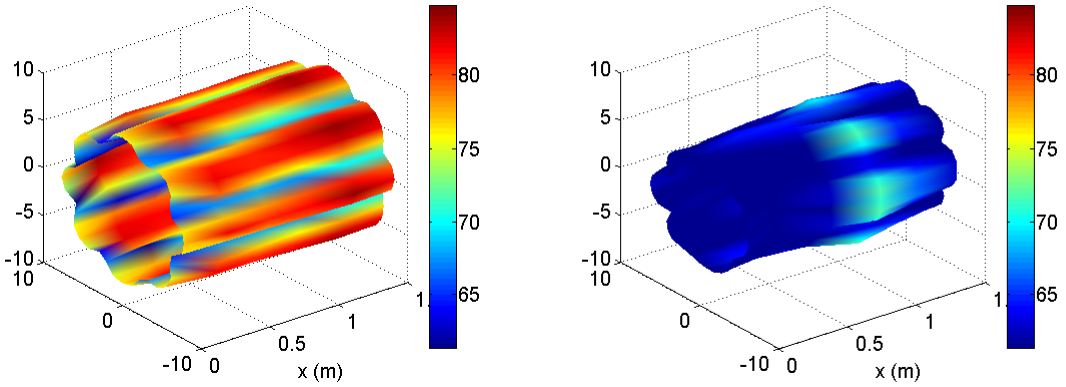

(a) (b)

Figure 51: Radiated pressure (dB ref 2e-5 Pa) measured by the microphone array at $f = 1980$ Hz. (a) Axisymmetric case. (b) Non-axisymmetric case.

The stationary phase theorem given in Eq. (14) is used to calculate the pressure radiated in the far-field using the vibrations measurements on the cylindrical shell in the wavenumbers domain. $\mathcal{R}$ is chosen equal to 1 m. The theorem is applied on the whole frequency range but it is important to bear in mind that it is only valid above around 3 kHz, in order to meet the criterion $\mathcal{R} \gg \frac{2\pi}{k_0}$. The radiated pressure field is plotted in Fig. 52 for the configurations at two frequencies. These plots allows to see more clearly the influence of the internal frame on the amplitude and the directivity of the system. More lobes can especially be seen at $f = 3580$ Hz.

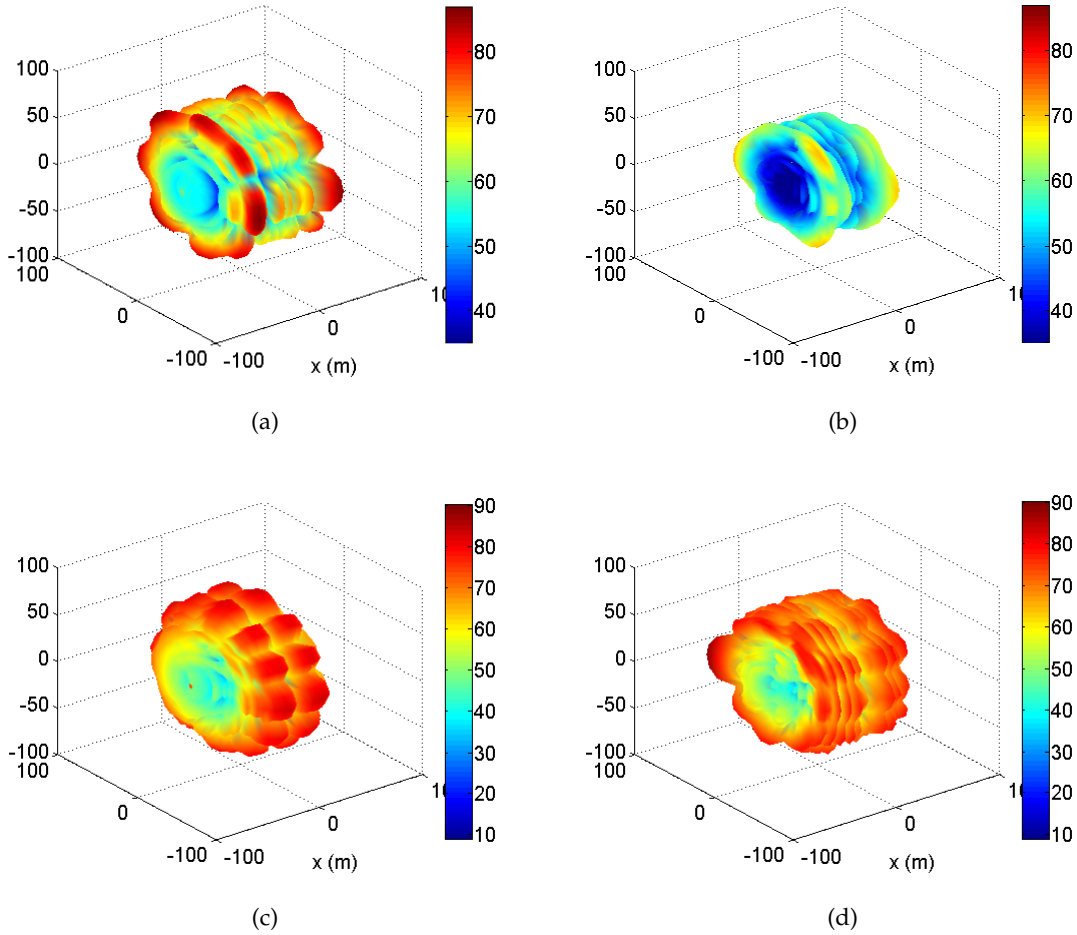

Figure 52: Radiated pressure (dB ref 2e-5 Pa) calculated by the stationary phase theorem. (a) Asymmetric case at $f = 1980$ Hz. (b) Non-axisymmetric case at $f = 1980$ Hz. (c) Asymmetric case at $f = 3580$ Hz. (d) Non-axisymmetric case at $f = 3580$ Hz.

The far-field radiated power is estimated by the two different means:

- using the microphone measurements and integrating the square of the pressure over the surface of the cylinder delimited by the $+$ in Fig. 50:

$$W_a^{exp} = \frac{1}{\rho_0 c_0} \int_{x=0}^{L} \int_{\theta=0}^{2\pi} p^2(x, \mathcal{R}, \theta) \mathrm{d}x \mathcal{R} \mathrm{d}\theta \tag{77}$$

- using the stationary phase theorem and integrating over the surface of the sphere of radius $\mathcal{R}$:

$$W_a^{th} = \frac{1}{\rho_0 c_0} \int_{\xi=0}^{\pi} \int_{\theta=0}^{2\pi} p^2(\mathcal{R}, \xi, \theta) \mathcal{R}^2 \sin\theta \mathrm{d}\xi \mathrm{d}\theta \tag{78}$$

It is clear that W_a^{exp} is only a rough estimation of the radiated power for several reasons: the axial microphone resolution is too weak to describe the pressure field, the surface for the calculation is not enclosing the volume (no microphone has been placed on the top and bottom surfaces of the virtual cylinder surrounding the system) and there are reflections on the floor. Further measurements using for instance sound intensity and measurement by scanning [190] should be conducted. Besides, the stationary phase theorem is based on the assumption of a baffled cylinder. However, W_a^{exp} and W_a^{th} are compared in Fig. 53, in narrow band and in third-octave band. Regarding the assumptions made for the two methods, it can be said that the comparison is satisfactory, with differences on sound power level in third-octave bands not bigger than 6 dB. The stationary phase theorem is then used to evaluate the influence of the non-axisymmetric internal frame on the radiated power.

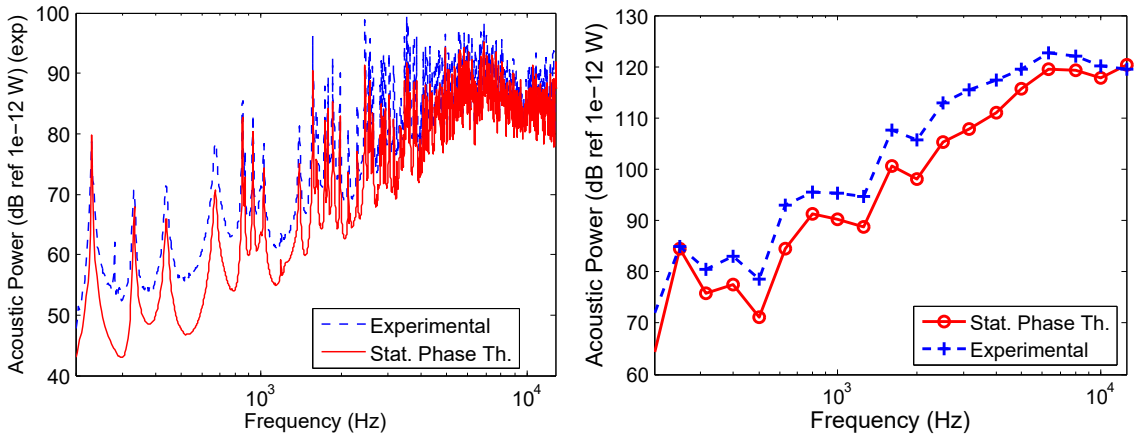

(a) (b)

Figure 53: Radiated power (dB ref 1e-12 W) as a function of the frequency estimated experimentally (blue dashed curve) and calculated with the stationary phase theorem (red solid line). (a) Narrow bands. (b) Third-octave bands.

The radiated power calculated from the spectral displacements and the stationary phase theorem is plotted as a function of the frequency for the axisymmetric and non-axisymmetric case in Fig. 54a. The radiated power is higher in the low frequencies (below 1 kHz) when there is the non-axisymmetric internal frame. At higher frequencies, it is harder to see the influence of the non-axisymmetry. The radiation efficiency (see Eq. (6)) is plotted in Fig. 54b. The coincidence frequency for the equivalent plate

($h = 1.5$ mm, in air) is plotted with a vertical dotted line. It is clear that the non-axisymmetric internal frame tends to increase the radiation efficiency below the coincidence frequency. Differences up to 10 dB can be seen at some frequencies on this configuration. This phenomenon is linked to the role played by the low circumferential orders components, as shown in Fig. 47. These results comfort the observations made in chapter 3. Above the coincidence frequency, it can be said that the structure radiates efficiently with and without the non-axisymmetry.

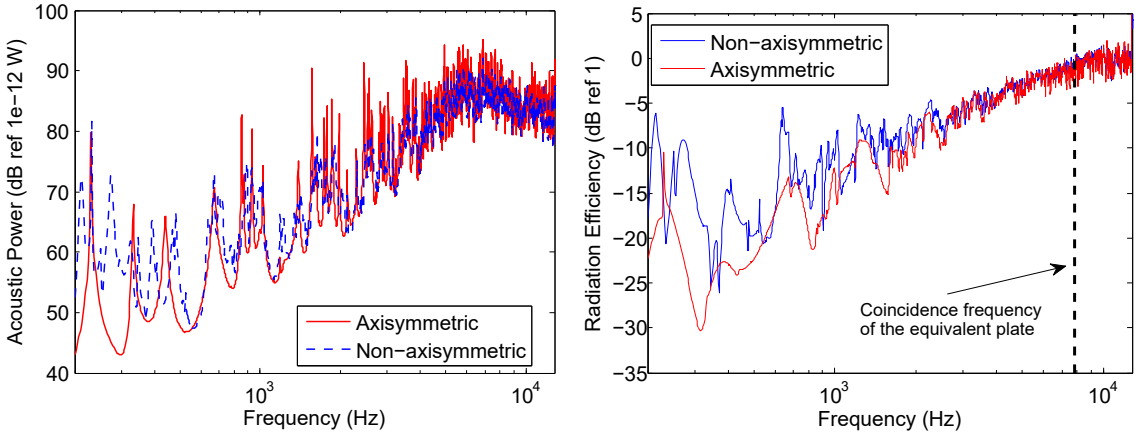

(a) (b)

Figure 54: Estimation as a function of the frequency for the two configurations using the stationary phase theorem of (a) the radiated power (dB ref 1e-12 W) and (b) the radiation efficiency (dB ref 1).

4.3 EXPERIMENTAL/NUMERICAL COMPARISON

In this section, a comparison between the experimental results and numerical simulations is made for the mean quadratic velocity on the surface of the cylindrical shell. The axisymmetric system is modeled with the CAA, which principle is described in section 1.2.5. Simply supported boundary conditions at the end of the cylindrical shell are introduced in the model. It is done by adding fictive frames which admittances are null for the radial displacements (blocked condition) and high for the other displacements (free condition). The high admittances values are chosen by multiplying by a factor 1000 the values calculated for the stiffeners used in the model. The stiffeners ad-

mittances are calculated by FEM and are modeled by shell elements. The CTF method is used to add the non-axisymmetric internal frame, which is described by FEM and shell elements and modal superposition with residual modes. The simulations are done using standard steel with a structural damping coefficient of $\eta = 0.005$, constant with regard to the frequency. The frequency range is between 200 and 12800 Hz, with 1000 values logarithmically spread.

Fig. 55 shows the comparison between the experimental and numerical results for the axisymmetric case.

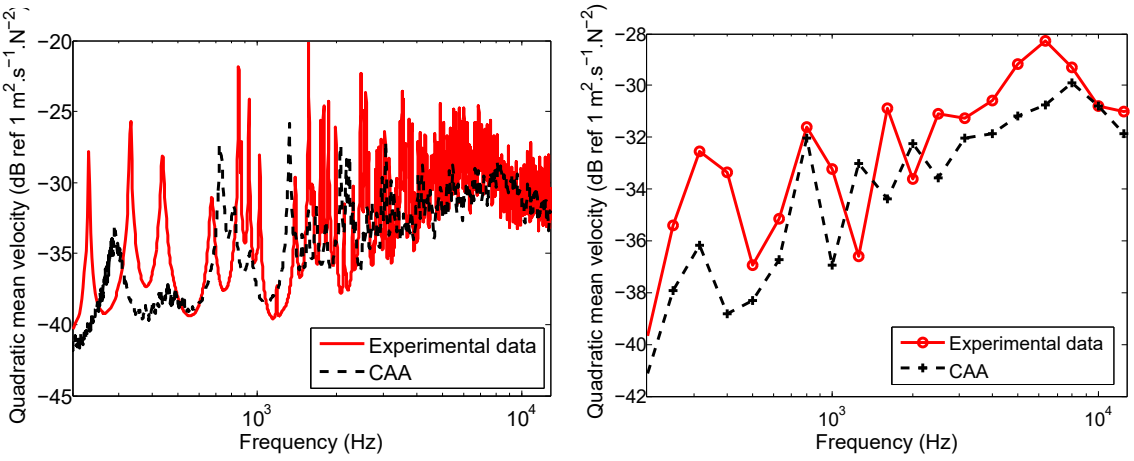

Figure 55: Comparison of the mean quadratic velocity between experimental and numerical results for the axisymmetric case. (a) Narrow band response and (b) response averaged on third-octave bands.

Discrepancies can be seen, that are mainly explained by the following points:

- the boundary conditions differ between the experimental setup and the numerical model. The end caps are massive steel parts screwed at the end of the cylinder and cannot be modeled by simple boundary conditions. This will have mainly an influence on the low frequencies and more especially on the resonance peaks loci;
- the material characteristics are not exactly known. In particular, the structural damping coefficient is difficult to estimate, and is generally in practice not a constant value over the whole frequency range;

- the system is excited by a radial point force for the numerical simulations, while in the experimental setup the force is applied over a small surface, which is glued on the cylindrical shell, and which may contain other components than the radial one.

Nevertheless, results show a good agreement between the measurements and the numerical prediction.

The comparison between experimental and numerical results for the non-axisymmetric case is shown in Fig. 56.

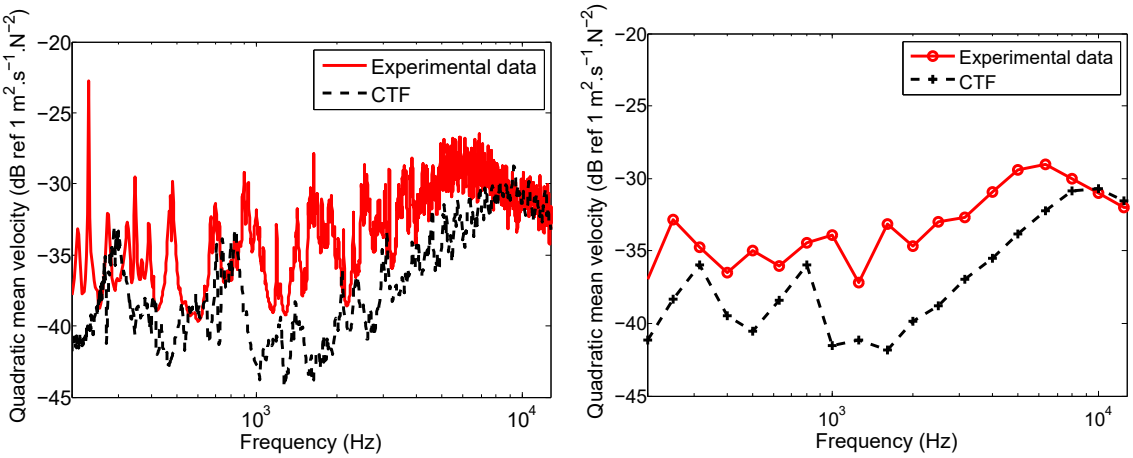

Figure 56: Comparison of the mean quadratic velocity between experimental and numerical results for the non-axisymmetric case. (a) Narrow band response and (b) response avergaed on third-octave bands.

Differences can be seen between the two curves. These differences can be explained by the same reasons pointed out for the axisymmetric case. Moreover, the numerical simulation predicts lower mean quadratic velocity level than the measurements in the middle frequency range. It can be partially explained by the fact that the non-axisymmetric frame is fixed with adhesive in the experimental setup, and even if particular care has been taken for this junction, displacement continuity cannot be perfectly achieved. The numerical model tends thus to be stiffer at this location than the experimental model, and the mean quadratic velocity drops.

In a similar manner than presented in section 4.2.3, numerical operational dispersion curves are plotted in Fig. 57.

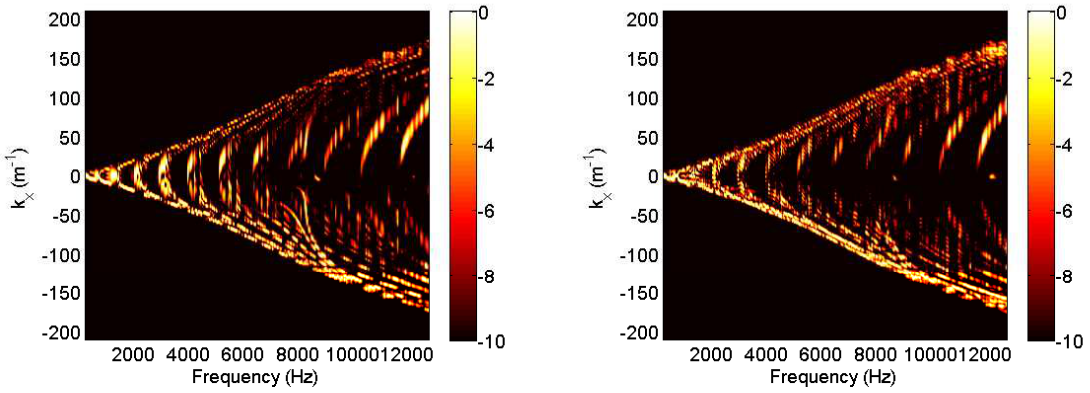

(a) (b)

Figure 57: Numerical operational dispersion curves plotted from the radial displacements in the (a) axisymmetric case and the (b) non-axisymmetric case.

These curves are to compare with the experimental ones in Fig. 48. The same phenomena can be seen in the experimental and numerical case:

- the difference in the dispersion curves trajectories below and above the ring frequency can be seen, changing from S-curves to square-root shape;
- the trajectories appear less clearly for low axial wavenumbers in the non-axisymmetric case.

From all these results and regarding to the assumptions made for the numerical model, the numerical/experimental comparison is thus satisfactory.

4.4 CONCLUSIONS

Experimental work on a model in air highlights the influence of a non-axisymmetric internal frame on the vibroacoustic behavior of a ribbed cylindrical shell. The trends observed in chapter 3 are thus verified thanks to cartographies in the physical and spectral domain, as well as frequency response of mean quadratic velocity and radiated power. Indeed, more circumferential orders play a role in the non-axsiymmetric case, tending to increase the radiation efficiency, especially below the coincidence frequency. Besides, because of the high modal density and an adapted impedance, an apparent

damping effect can be seen. A comparison with numerical results shows that the CTF approach presented in this work is suitable to study this kind of problems.

Some limits of the experimental work can be discussed. Indeed, the model considered for the measurements is about 50 times smaller than a typical system for industrial applications. A scaling factor can be used for the geometrical characteristics and for the frequencies, but the material parameters remain the same. This means that the ring frequency is much higher in the model than in real systems, and the curvature of the cylindrical shell plays an important role on a wider frequency range. Besides, structural damping tends usually to decrease with frequency [180] and will be overestimated in the model compared to a real system. Another limit for naval applications is that the experiment has been conducted in air instead of water for practical reasons. Simulations show that the influence of non-axisymmetries is similar in both cases. However, as the sound travels faster in water than in air, the coincidence frequency is about 20 times higher when the system is submerged in water. As it was shown that the non-axisymmetric internal frames have mainly an influence below the coincidence frequency, it means that they play a role on a broader frequency range when it is submerged in water. An experimental campaign could be conducted in water to check these trends, similarly to a recent study on the influence of the propeller shaft [191, 192].

5

ACOUSTIC SCATTERING FROM SUBMERGED STIFFENED CYLINDRICAL SHELLS COUPLED TO NON-AXISYMMETRIC INTERNAL STRUCTURES

This chapter is based on the following articles:

- "Scattering of a periodically stiffened submerged shell coupled to non-axisymmetric internal frames", published in the proceedings of the *ICSV22 (International Congress on Sound and Vibration)* in Florence, Italy, July 2015 [193].
- "A substructuring approach for modeling the acoustic scattering from stiffened submerged shells coupled to non-axisymmetric internal structures", published in the *Journal of the Acoustical Society of America* [201].

The CTF method is applied to the case of an acoustical excitation, in order to study the scattered pressure from a stiffened submerged shell with internal structures. A test case application is given and the physical phenomena are discussed.

5.1 EXTENSION OF THE CTF METHOD TO AN ACOUSTICAL EXCITATION

In this section, the CTF method is extended for the case of an acoustical excitation. As shown in Fig. 58, the system considered is made of an axisymmetric stiffened submerged cylindrical shell (subsystem 2), coupled to an internal non-axisymmetric frame (subsystem 1). An acoustic domain Ω is surrounding the cylindrical shell and M is a point in the fluid domain. An acoustic plane wave impinges the shell in the vertical plane $\theta = 0$, with a varying incidence ξ with regard to the normal to the shell. No fluid is considered inside the cylindrical shell.

The harmonic acoustic excitation is characterized by the blocked pressure, *i.e.* the pressure induced in the fluid when the system is considered as rigid [8]. In that case,

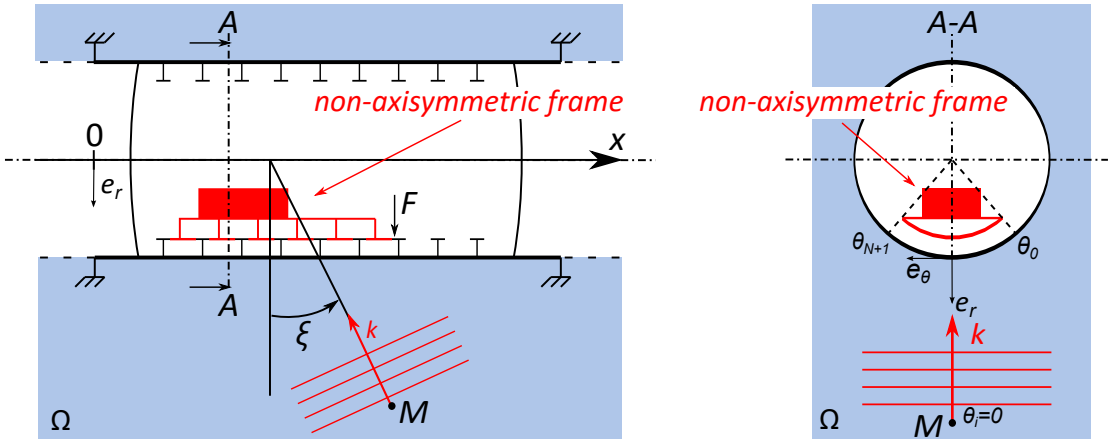

(a) (b)

Figure 58: Sections of a stiffened cylindrical shell model including a non-axisymmetric internal frame and impinged by an oblique incident wave. (a) View in the plane $\theta = 0$. (b) View in the plane $x = x_A$.

the total pressure in the fluid medium Ω can be decomposed as the sum of the blocked pressure p_b and the reradiated pressure p_{re} due to the system vibrations:

$$p = p_b + p_{re} \tag{79}$$

p_{re} is called the reradiated pressure to clearly distinguish the scattering due to the system vibrations from the scattering from the infinitely rigid body. The aim is to calculate the reradiated pressure at the point M when the two subsystems are coupled.

The fundamental equations of the CTF method, Eqs. (45) and (47), are still valid for an acoustical excitation. The only difference lies in the fact that the free condensed displacements on the right hand term of Eq. (45) needs to be calculated for the subsystems for acoustical excitation. In the example studied in this chapter, subsystem 1 has no excitation, so $\bar{\mathbf{U}}^1 = 0$. The free condensed displacements for subsystem 2 (*i.e.* the axisymmetric stiffened submerged cylindrical shell) can be calculated by the CAA from the response to an acoustical excitation [150]. The CTF calculation for each uncoupled subsystem follows the same procedure than in chapter 3.

5.2 DESCRIPTION OF A TEST CASE APPLICATION

In this section, non-axisymmetric internal frames are added to the stiffened shell as experimentally investigated by Liétard *et al.* [48], and numerically modeled by Maxit [150]. The system is modeled by a 750 mm long simply-supported cylindrical shell with a radius of $R = 50$ mm and a thickness of $h = 1$ mm. It is stiffened by 49 evenly spaced internal rings having 5 mm $\times$ 1 mm rectangular cross-sections. The stiffeners spacing is $d = 15$ mm. The system is made of steel, having the same characteristics than in [150] ($E = 2.4 \times 10^{11}$ Pa, $\rho_s = 7900$ kg.m^{-3}, $\nu = 0.3$) and immersed in water ($\rho_0 = 1000$ kg.m^{-3}, $c_0 = 1470$ m.s^{-1}). A structural damping coefficient of $\eta = 0.2\%$ is accounted for as a complex factor in the stiffness matrix.

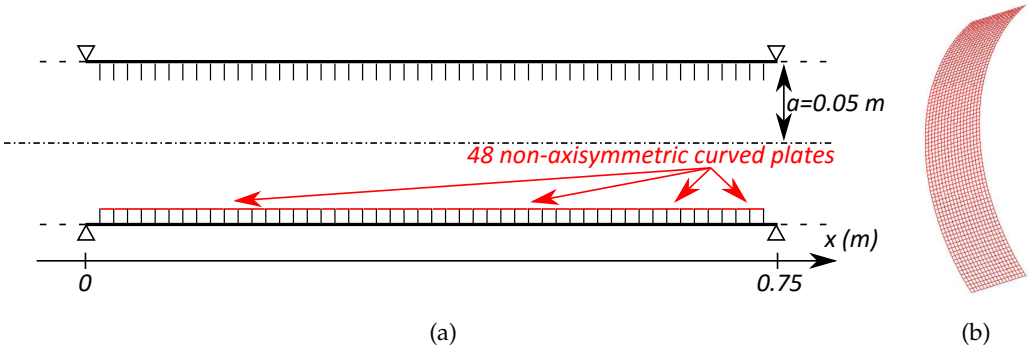

(a) (b)

Figure 59: (a) Section in the plane $\theta = 0$ of the cylindrical shell. (b) FEM model of one curved plate.

48 curved plates (15 $\times$ 73 mm^2, 1 mm thick, curvature radius of $R_{int} = 45$ mm, represented by the mesh in Fig 59b) are added at the tip of the stiffeners, on the whole length of the shell, as shown in Fig. 59a. This results in 47 junctions between one rib and two plates and 2 junctions between one rib and one plate at the ends. These plates are non-axisymmetric and extend from $\theta = -46°$ to $\theta = 46°$, covering thus approximately one fourth of the circumference. A plane wave impinges the system symmetrically (*i.e.* in the plane $\theta = 0$, coming from under the shell in Fig. 58 and 59a).

According to the convergence criterion defined in chapter 2, the length of the gate functions L_S is chosen to be shorter than half the smallest flexural wavelength in the frequency range of interest. Considering frequencies up to 200 kHz ($k_0 R \simeq 42$) this

criterion allows a maximum gate function length of 3.6 mm for the present case. As the coupling junction between a rib and the curved plates is 73 mm long, $N = 20$ condensation functions are taken into account.

The Finite Element model used for calculating the condensed transfer functions of the plates is made of quadrilateral isotropic shell elements. The mesh is fine enough to respect the criterion of 6 elements per bending wavelength at the highest frequency. As the 48 plates are identical, it is sufficient to calculate the condensed transfer functions on one plate and use them for all the junctions. Details on the parameters for the CAA calculation are found in [150]. It is worth noting that the Love's first approximations for shells are still valid at high frequencies and the shell theories can thus still be used [2].

In the previous section, the process to couple an axisymmetric shell described by CAA with non-axisymmetric internal structures described by FEM has been explained. The sketch in Fig. 60 summarizes the different steps and gives calculation times for each step for the test case used in this section. Given calculation times correspond to the frequency of 200 kHz, and for all incidence angles ξ varying between 0 and 179° with a step of 1°. The method is coded in Matlab. FEM is used to calculate the internal structures admittances: NASTRAN for the axisymmetric ribs and the Structural Dynamics Toolbox (SDT) for the non-axisymmetric internal frames. Calculations are performed on a 64 GB RAM computer. Fig. 60 shows that the calculation for the axisymmetric case takes approximately 15 minutes (the response to mechanical excitations is only necessary to calculate the condensed transfer functions for the coupling). As quantities are stored in a database, taking into account the 48 non-axisymmetric plates adds less than 32 minutes of calculation, that being three times more than the axisymmetric case. This time can however be shortened by parallelizing some steps that are independent, as for instance the response of the axisymmetric subsystem to acoustical and mechanical excitations.

No comparison can be proposed by classical numerical methods such as FEM-BEM, regarding the size of the whole system and the frequencies of interest, for which the scattering phenomena can be observed. Nevertheless, each step of the process has been previously validated. The coupling between the analytical model of a shell *in vacuo* and stiffeners has been validated by comparison with FEM [194]. Validation for the case with heavy fluid loading has then been made [21], and the introduction of plane wave

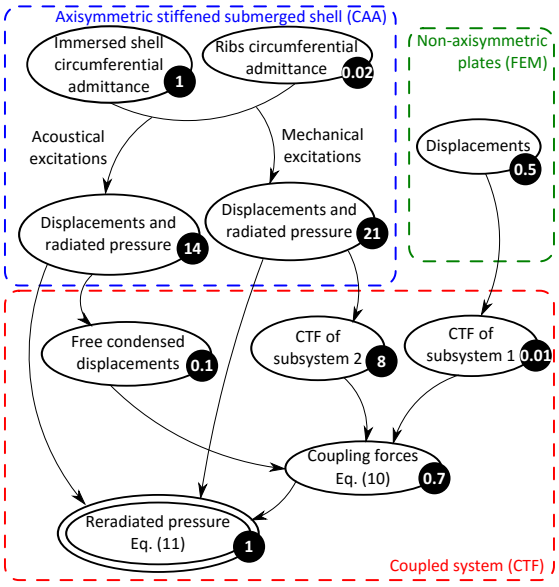

Figure 60: Sketch of the method to account for non-axisymmetric internal frames in a stiffened submerged shell, with corresponding calculation times (in minutes).

excitations has been compared to measurements [150]. Finally, the CTF method used to take into account the non-axisymmetric internal frames has been validated by FEM comparisons [172, 173], and it can thus be said that the results presented in this chapter are valid.

5.3 INFLUENCE OF THE NON-AXISYMMETRIC INTERNAL FRAMES ON THE BACKSCATTERING

The reradiated component of the backscattered pressure (*i.e.* the pressure scattered back to the direction of the incident wave) from the stiffened shell, without the non-axisymmetric internal frames, is plotted in Fig. 61a [150], as a function of the dimensionless frequency k_0R and the incidence angle ξ. Higher values of backscattered pressure are due to helical waves in the case of low incidence angles (ξ<30^o) and for $k_0R \in [0, 30]$. High values of pressure can also be seen because of Bloch-Floquet and Bragg scattering, for which the incidence angle decreases with the frequency. These two phenomenon are due to the regularly spaced ribs. Bragg scattering is the result of interferences of the geometrical reflections of the incident plane wave on the rings. Bloch-Floquet scattering

results from the quasi-flexural waves which propagates along the shell and interacts with the ribs [48].

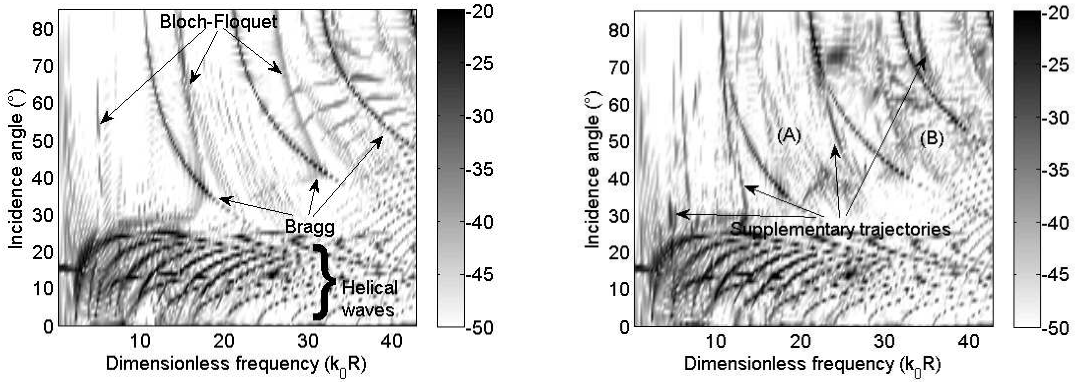

(a) (b)

Figure 61: (a) Spectrum of backscattered pressure of the axisymmetric shell. (b) Spectrum of the shell including the non-axisymmetric internal frames.

The influence of the non-axisymmetric internal frames on the backscattered pressure spectrum is evaluated using the CTF method and the results are plotted in Fig. 61b. Differences can be seen on the backscattered spectrum and the following comments can be made:

- The propagation of helical waves on the shell is not significantly affected by the presence of the internal frames.
- Similarly, as the regularly spaced ribs have not been modified, the Bragg scattering due to geometrical reflections can still be clearly seen.
- Supplementary trajectories, that can be related to Bloch-Floquet scattering, can be observed. A focus on this phenomenon is proposed in the next section. In the following, the adjective "standard" refers to the Bloch-Floquet waves seen in the axisymmetric case, whereas "supplementary" refers to the trajectories marked in Fig. 61b and that are due to the internal structures.
- In the areas marked (A) and (B), standard Bloch-Floquet waves that are visible in the axisymmetric case can no longer be clearly seen. This can be explained by the

apparition of supplementary vibration energy propagation paths that reduce the energy paths at the origin of the standard Bloch-Floquet waves.

In the CAA, the circumferential orders are calculated separately and the quantities $\bar{p}^2_{re}(M)$ and $\mathbf{Y}^2_{Mi}$ can be expressed as Fourier series. Hence, the left hand term of Eq. (59) can also be written as a Fourier serie, as seen in Eq.(66). In this sense, it is possible to isolate the contribution of a given circumferential order. For $n = 4$ for instance, only two trajectories related to helical waves can be seen for the axisymmetric case: one due to shear waves and the other one due to compressional waves, as shown in the upper part of Fig 62. This spectrum can be compared to the non-axisymmetric case in the lower part of Fig 62. The dominant trajectories corresponding to the shear and compressional helical waves are the same than in the axisymmetric case. Nevertheless, additional trajectories can be seen between the two dominant trajectories. This observation highlights that there is a coupling between the circumferential orders due to the non-axisymmetry. This result is consistent with the literature [164, 167, 173], and can also explain why the patterns are more complex in the areas marked (A) and (B) in Fig. 61b.

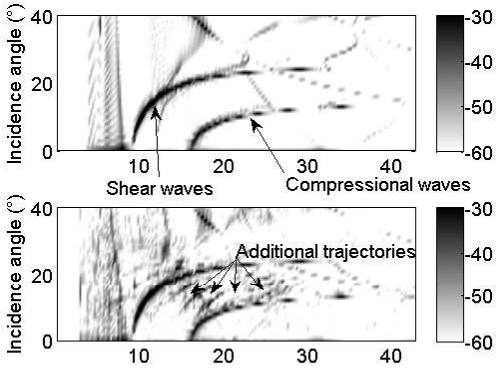

Figure 62: Spectrum of backscattered pressure for the circumferential order $n = 4$. Upper part: axisymmetric shell. Lower part: non-axisymmetric shell.

5.4 DISCUSSION ON THE SUPPLEMENTARY TRAJECTORIES

In order to take a close look on the supplementary trajectories marked in Fig. 61b, only the contribution of the circumferential order $n = 1$ is plotted in Fig. 63a. According

to their shape and to the litterature [46, 48, 49], these supplementary trajectories are related to Bloch-Floquet scattering and are marked BF (F) for the forward waves and BF (B) for the backward waves. At high incidence ($\xi \sim 80°$), the Bloch-Floquet forward waves appear at the same frequency than for Bragg scattering. This observation happens to be a simple geometrical coincidence but is helpful to check the trajectories' locations on the frequency-angle spectrum.

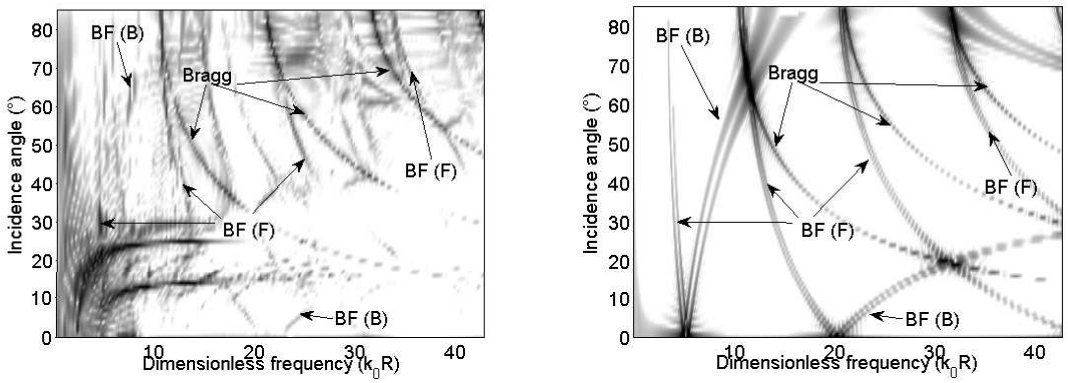

(a) (b)

Figure 63: (a) Spectrum of backscattered pressure of the non-axisymmetric shell for the circumferential order $n = 1$ only. (b) Trajectories of Bragg and Bloch-Floquet waves using the simplified interference model.

To analyze the phenomenon in more detail, a simple scattering/interference model based on the formulation given by Lietard *et al.* [48] is developed. The sketch in Fig. 64 shows that in addition to the propagation wave along the shell, the flexural waves can propagate in the internal structures. Indeed, an incoming wave impinges the shell on a stiffener q, creates structural vibration that can propagate through the stiffeners and the curved plate to finally radiate through the shell at another stiffener m. Taking into account that all the stiffeners are excited by the acoustic wave, the trajectories of this Bloch-Floquet scattering is given by the following double summation:

$$p^{BF} = p_0 \sum_{q=1}^{49} e^{\mathrm{j}2k_0(q-25)d\sin\xi} \sum_{m=1}^{49} e^{\mathrm{j}\Psi_{mq}} \tag{80}$$

with

$$\Psi_{mq} = (m-q)\left(\mathrm{sgn}(m-q)k_{xf}(2h_w+d) + k_0 d\sin\xi\right) \tag{81}$$

where $x \mapsto \mathrm{sgn}(x)$ is the sign function, h_w is the height of a stiffener, and k_{xf} is the wavenumber of the flexural waves in the internal frames, decomposed in the plane $\theta = 0$. k_{xf} depends on the circumferential order n and on the flexural wavenumber of an equivalent *in vacuo* plate k_f:

$$k_{xf}(n) = \sqrt{k_f^2 - \left(\frac{n}{R}\right)^2} \tag{82}$$

Plotting these equations for $n = \{1, 4\}$ with a normalized amplitude gives the spectrum in Fig. 63b. The standard Bloch-Floquet waves due to the waves propagating on the shell are not represented for the sake of clarity, but Bragg scattering is kept as a point of reference on the frequency-angle spectrum. The fourth circumferential order has been chosen because it might play a particular role considering that the curved plates cover one fourth of the circumference. The flexural wavenumber k_f at a frequency f is calculated using the following formula (*cf* Eq. (71)):

$$k_f = \sqrt{\frac{2\pi f}{h'}} \left(\frac{12(1-\nu^2)\rho}{E}\right)^{1/4} \tag{83}$$

where h' is a corrected thickness that accounts for the fact that the plates are stiffened by the ribs and is calculated by averaging the material added by the stiffeners along the shell, resulting in $h' \simeq 1.3$ mm.

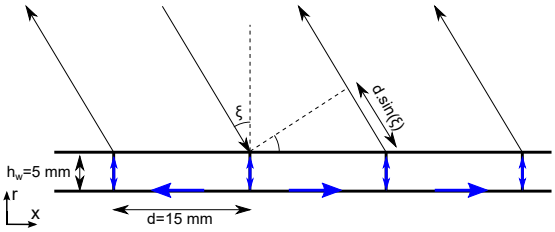

Figure 64: Sketch of the insonified shell and of the propagation of flexural waves in the internal structures.

Comparing Fig. 63a and Fig. 63b show satisfying results. Indeed, the loci of the supplementary Bloch-Floquet trajectories evaluated with the model match the ones on the numerical simulations. Slight shifts can however be observed, especially at high frequencies. This is explained by the fact that the interference model is built to give trends and is highly simplified. More precisely, the model is not able to accurately account for all the couplings between the shell, the ribs, and the internal plates.

Additional simulations have been conducted on modified geometries to check the assumptions made in this section. In each configuration, the system is the same than the one presented previously, with just one geometrical parameter changed. The spectra are presented in Fig. 65.

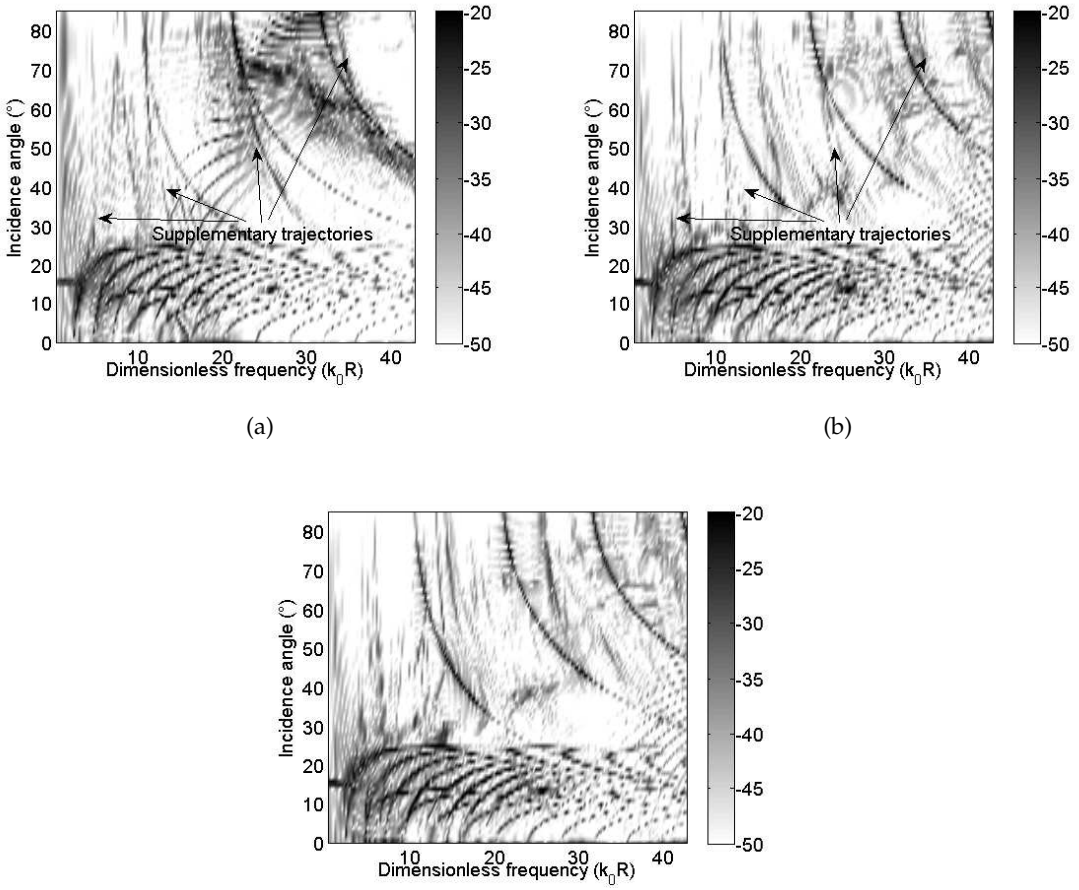

Figure 65: Spectrum of backscattered pressure of the non-axisymmetric shell with geometric modifications: (a) Shell thickness doubled, (b) plates length reduced and (c) plates thickness doubled.

The following comments prove that the supplementary trajectories depend on the geometrical parameters of the internal structures only:

- If the shell thickness is doubled, the supplementary Bloch-Floquet trajectories are not modified. Bragg scattering is also unchanged but the locations of the standard Bloch-Floquet waves traveling on the shell are changed. (Fig. 65a)

- If the plates length is reduced (covering only one eight of the circumference for instance), the supplementary Bloch-Floquet trajectories are the same but can be seen less clearly. (Fig. 65b)
- If the internal plates thickness is changed, the supplementary trajectories are no longer visible. In this case, the plates thickness is no longer the same than the ribs thickness. Hence, there is an impedance mismatch between the stiffened shell and the internal structures, and the waves cannot propagate easily. (Fig. 65c)

5.5 CONCLUSIONS

The substructuring CTF method has been applied to predict numerically the scattering from a stiffened submerged shell with non-axisymmetric internal frames. As only condensed transfer functions at the junctions between the subsystems are needed, one of the main advantages of this method is that it is able to couple subsystems that are described by different approaches. In this chapter, the stiffened shell has been described by the CAA while the internal frames have been modeled by the FEM. As the FEM offers great flexibility on the geometrical design, any non-axisymmetric internal frame coupled along a line junction can be taken into account by the CTF method. The method is however more efficient for junctions where the axial and radial coordinates remain constant in order to benefit from the axisymmetric properties of the stiffened shell. Two other advantages of the CTF approach is that it can reach high frequencies ($k_0 R > 40$) and that the results can be directly investigated in the wavenumber space.

Through a particular example of an immersed shell with internal plates joining adjacent stiffeners all along the shell, it has been shown that the non-axisymmetric frames have an influence on the backscattered spectrum. Indeed, the Bloch-Floquet scattering is more difficult to identify than in the axisymmetric case. Moreover, supplementary trajectories related to Bloch-Floquet scattering, for which waves propagate through the non-axisymmetric internal structures, have been pointed out and explained through a simple interference model. These trajectories highly depend on the geometry of the internal structures, but it shows that scattering due to flexural waves traveling inside the shell can be seen in the far-field. As the developed model presents high versatiliy concerning the design of the internal structures, further work consists in modeling

cases of internal structures taken from industrial applications and investigate their effect on the scattered pressure field. Moreover, as the modeling of the internal structure is carried out independantly from the stiffened shell modeling for the calculation of the CTF, this approach is well adapted to optimize internal structures with regard to the backscattered pressure.

6

VIBROACOUSTIC MODELING OF SUBMERGED STIFFENED CYLINDRICAL SHELLS WITH INTERNAL STRUCTURES FOR RANDOM EXCITATIONS

This chapter is based on the article entitled "Vibroacoustic modeling of submerged stiffened cylindrical shells with internal structures under random excitations", published in the proceedings of *Inter-noise 2016* in Hamburg, Germany, in August 2016 [195].

The aim of this chapter is to study the problem of a ribbed cylindrical shell coupled to internal structures and excited by random pressure fields. The proposed modeling is based on the combination of the wavenumber-point (k, M) reciprocity technique and the CTF method. The first one estimates the sensitivity functions at point M of the system from its vibratory velocity field induced by a point excitation at M. This velocity field is estimated with the second method. A numerical example of a submerged stiffened cylindrical shell excited by random pressure fields will be given and the influence of the internal frames will be discussed.

6.1 THE WAVENUMBER-POINT (k, M) RECIPROCITY TECHNIQUE

This section is based on the wavenumber-frequency formulation which can be found in the literature [81, 186, 67]. The wavenumber-point (k, M) reciprocity technique has been presented in details by Maxit and Denis [84] and the general outline is briefly described in this section.

Let us consider a vibroacoustic system made of a structure coupled to a fluid domain. The surface Σ_p is excited by a random pressure field characterized by its second order moment $S_{p_b p_b}\left(\check{\mathbf{x}}, \check{\check{\mathbf{x}}}, f\right)$. The space Fourier transform of $S_{p_b p_b}\left(\check{\mathbf{x}}, \check{\check{\mathbf{x}}}, f\right)$ can be written as a function of the wavenumber-frequency spectrum of the wall pressure $\phi_{pp}(\mathbf{k}, f)$:

$$S_{p_b p_b}\left(\check{\mathbf{x}}, \check{\check{\mathbf{x}}}, f\right) = \frac{1}{(2\pi)^2} \iint_{-\infty}^{+\infty} \phi_{pp}(\mathbf{k}, f) e^{-\mathrm{j}\mathbf{k}(\check{\check{\mathbf{x}}}-\check{\mathbf{x}})} \mathrm{d}^2\mathbf{k} \tag{84}$$

$\phi_{pp}(\mathbf{k}, f)$ is a Power Spectrum Density (PSD) that characterizes the excitation and is supposed to be known. This value is expressed in $Pa^2.s$ and is defined for positive frequencies only.

Let us define the sensitivity function $\tilde{\tilde{H}}_W(\mathbf{x}, \mathbf{k}, f)$ as the frequency response at point $\mathbf{x}$ when the system is excited by a plane wave with wavevector $\mathbf{k}$:

$$\tilde{\tilde{H}}_W(\mathbf{x}, \mathbf{k}, f) = \frac{1}{(2\pi)^2} \int_{\Sigma_p} H_W(\mathbf{x}, \check{\mathbf{x}}, f)\, e^{-j\mathbf{k}\check{\mathbf{x}}} d\check{\mathbf{x}} \tag{85}$$

where $H_W(\mathbf{x}, \check{\mathbf{x}}, t)$ is the impulse response of the system at point $\mathbf{x}$ when excited by an impulse unitary force at point $\check{\mathbf{x}}$. It should be noted that the plane wave $\mathbf{k}$ can be either propagating either evanescent, depending on its value compared to the acoustic wavenumber $k_0 = \frac{2\pi f}{c_0}$. Thus, injecting Eq. (84) into Eq. (17) and using Eq. (85), the space-frequency spectrum of displacement can be written finally as:

$$S_{WW}(\mathbf{x}, \check{\mathbf{x}}, f) = \frac{1}{4\pi^2} \iint_{-\infty}^{+\infty} \tilde{\tilde{H}}_W^*(\mathbf{x}, \mathbf{k}, f) \phi_{pp}(\mathbf{k}, f) \tilde{\tilde{H}}_W(\check{\mathbf{x}}, \mathbf{k}, f) d^2\mathbf{k} \tag{86}$$

If one is interested only in the PSD of the displacement at point $\mathbf{x}$ (*i.e.* $\mathbf{x} = \check{\mathbf{x}}$), Eq. (86) can be written as follows:

$$S_{WW}(\mathbf{x}, f) = \frac{1}{4\pi^2} \iint_{-\infty}^{+\infty} |\tilde{\tilde{H}}_W(\mathbf{x}, \mathbf{k}, f)|^2 \phi_{pp}(\mathbf{k}, f) d^2\mathbf{k} \tag{87}$$

The same developments can be made for the spectral power density of the pressure at point $\mathbf{z}$. The sensitivity function $\tilde{\tilde{H}}_p(\mathbf{z}, \mathbf{k}, f)$ is defined as the frequency response at point $\mathbf{z}$ when the system is excited by a plane wave with wavevector $\mathbf{k}$:

$$\tilde{\tilde{H}}_p(\mathbf{z}, \mathbf{k}, f) = \frac{1}{(2\pi)^2} \int_{\Sigma_p} H_p(\mathbf{z}, \check{\mathbf{x}}, f)\, e^{-j\mathbf{k}\check{\mathbf{x}}} d\check{\mathbf{x}} \tag{88}$$

where $H_p(\mathbf{z}, \check{\mathbf{x}}, t)$ is the impulse response of the system at point $\mathbf{z}$ when excited by an impulse unitary force at point $\check{\mathbf{x}}$. Injecting Eq. (84) into Eq. (18) and using Eq. (88) yields:

$$S_{pp}(\mathbf{z}, f) = \frac{1}{4\pi^2} \iint_{-\infty}^{+\infty} |\tilde{\tilde{H}}_p(\mathbf{z}, \mathbf{k}, f)|^2 \phi_{pp}(\mathbf{k}, f) d^2\mathbf{k} \tag{89}$$

When solving a problem numerically, integrals over infinite domains such as in Eqs. (87) and (89) are an issue. However, it can be shown on systems such as plates or shells that the sensitivity functions $\tilde{\tilde{H}}_W(\mathbf{x}, \mathbf{k}, f)$ and $\tilde{\tilde{H}}_p(\mathbf{z}, \mathbf{k}, f)$ tend to 0 when $|\mathbf{k}| \to \infty$. Thus, a cutoff wavenumber $\mathbf{N_k}$ based on the response function of the system along the

wavenumbers can be defined [84], allowing the integration domain to be truncated. The difficulty now lies in the calculation of the sensitivity functions over the integration domain. In practice, it consists in determining the displacement at location $\mathbf{x}$ or the pressure at location $\mathbf{z}$ when the system is excited by all the wavenumbers included in the integration domain. This number of excitations can be large and can lead to prohibitive computation time. To tackle this issue, the use of the Lyamshev reciprocity principle is proposed [196]. It consists in exploiting the property that the transfer function between two points remains the same if the observation and excitation point are exchanged:

$$H_W\left(\mathbf{x}, \check{\mathbf{x}}, f\right) = H_W\left(\check{\mathbf{x}}, \mathbf{x}, f\right) \tag{90}$$

Eq. (85) can be written as follows:

$$\tilde{\tilde{H}}_W(\mathbf{x}, \mathbf{k}, f) = \frac{1}{(2\pi)^2} \int_{\Sigma_p} H_W\left(\check{\mathbf{x}}, \mathbf{x}, f\right) e^{-\mathrm{j}\mathbf{k}\check{\mathbf{x}}} \mathrm{d}\check{\mathbf{x}} \tag{91}$$

This equivalence is called the wavenumber-point (k, M) reciprocity principle. It means that the PSD of the displacement of the system at point $\mathbf{x}$ can be calculated using Eq. (87), knowing the vibratory field of the system excited by a point force at point $\mathbf{x}$. Similarly, the Lyamshev reciprocity principle is also valid for a point $\mathbf{z}$ in the fluid domain. The pressure at point $\mathbf{z}$ for a point force at $\check{\mathbf{x}}$ is equal to the displacement at point $\check{\mathbf{x}}$ when the system is excited by an acoustic monopole at point $\mathbf{z}$. Eq. (88) can be written:

$$\tilde{\tilde{H}}_p(\mathbf{z}, \mathbf{k}, f) = \frac{1}{(2\pi)^2} \int_{\Sigma_p} H_p\left(\check{\mathbf{x}}, \mathbf{z}, f\right) e^{-\mathrm{j}\mathbf{k}\check{\mathbf{x}}} \mathrm{d}\check{\mathbf{x}} \tag{92}$$

Hence, the PSD of the pressure at point $\mathbf{z}$ can be determined using Eq. (89), knowing the vibratory field of the system excited by a monopole in $\mathbf{z}$.

The reciprocity technique is illustrated for a stiffened submerged cylindrical shell in Fig. 66. In this case, the calculation of the sensitivity functions for a point force $\tilde{\tilde{H}}_W(\mathbf{x}, \mathbf{k}, f)$ and a monopole excitation $\tilde{\tilde{H}}_p(\mathbf{z}, \mathbf{k}, f)$ used in Eq. (87) and (89) is not straightforward. Therefore, the CTF method is used to tackle this issue. $\tilde{\tilde{H}}_W(\mathbf{x}, \mathbf{k}, f)$ is calculated with the procedure explained in chapter 3 for a system under a point force, and with the results given in the wavenumbers space. In order to estimate $\tilde{\tilde{H}}_p(\mathbf{x}, \mathbf{k}, f)$, some developments need however to be done to calculate the response of the system for a monopole excitation.

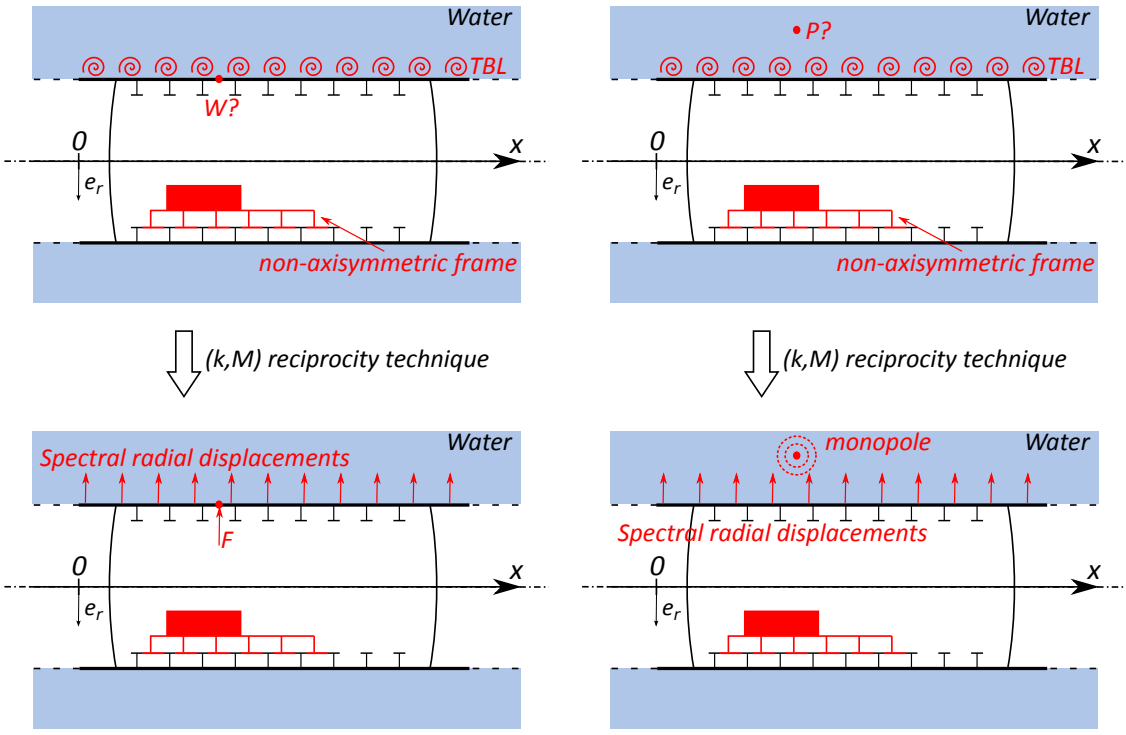

Figure 66: The (k, M) reciprocity technique applied to a stiffened submerged cylindrical shell with internal structures to evaluate (a) the displacement at a point on the shell surface or (b) the pressure at a point in the fluid domain.

6.2 APPLICATION OF THE CTF METHOD FOR A SYSTEM FOR A MONOPOLE EXCITATION

In order to calculate the PSD of the pressure $S_{pp}(\mathbf{z}, f)$ using the wavenumber-point (k, M) reciprocity technique presented previously, the CTF method is used to calculate $\tilde{H}_p(\mathbf{z}, \mathbf{k}, f)$. Therefore, the CTF method needs to be extended to take into account a monopole excitation at the location $\mathbf{z}$, as shown in Fig. 67. Similarly than in chapter 5, the only difference with the CTF method for a point force lies in the calculation of the free displacements in Eqs. (45) and (47). In this case, the external load is only applied on the cylindrical shell, using a blocked pressure term in the right-hand side of the Flügge equations (see Eq. (8)).

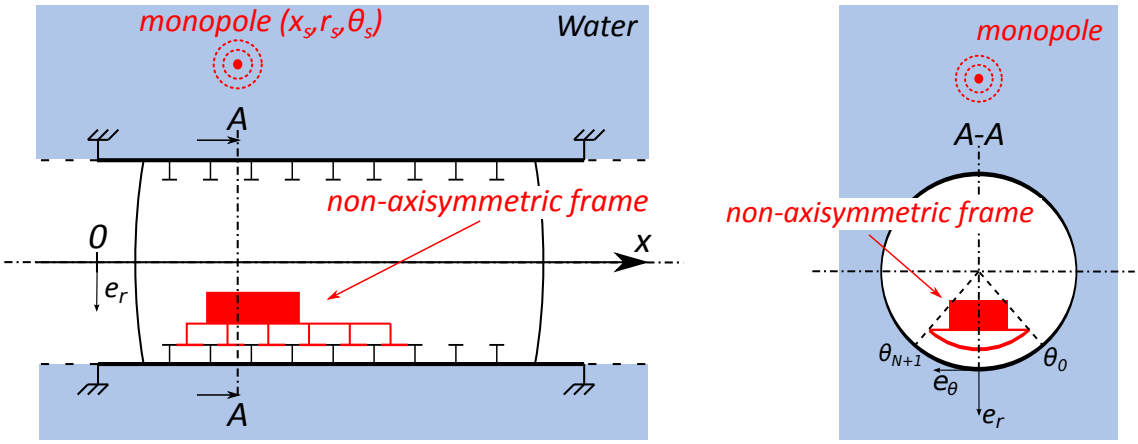

(a) (b)

Figure 67: Model of a stiffened cylindrical shell including a non-axisymmetric internal frame and an acoustic monopole in the fluid domain. (a) View in the plane $\theta = 0$. (b) View in the plane $x = x_A$.

The blocked pressure $p_b(x, r, \theta)$ is solution of the non-homogeneous Helmholtz equation:

$$\Delta p_b(x, r, \theta) + k_0^2 p_b(x, r, \theta) = q_{exc}(x, r, \theta) \tag{93}$$

where q_{exc} is the source term due to the monopole. The rigid boundary condition (Neumann) on the shell surface is written thanks to Euler's relation:

$$\frac{\partial p_b}{\partial r}(x, R, \theta) = 0 \tag{94}$$

The blocked pressure p_b is the sum of the incident pressure p_i and the scattered pressure p_s: $p_b = p_i + p_s$. The incident pressure is known and the scattered pressure needs to be calculated. From the previous equations, one can write:

$$\Delta p_s(x, r, \theta) + k_0^2 p_s(x, r, \theta) = 0 \tag{95}$$

and

$$\frac{\partial}{\partial r} p_s(x, R, \theta) = -\frac{\partial}{\partial r} p_i(x, R, \theta) \tag{96}$$

Applying a 2D Fourier transform along the axial and tangential coordinates to Eq. (95) and (96) yields:

$$\frac{\partial^2}{\partial r^2} \tilde{\tilde{p}}_s(k_x, r, n) + \frac{1}{r} \frac{\partial}{\partial r} \tilde{\tilde{p}}_s(k_x, r, n) + \left(k_r^2 - \frac{n^2}{r^2} \right) \tilde{\tilde{p}}_s(k_x, r, n) = 0 \tag{97}$$

$$\frac{\partial}{\partial r} \tilde{\tilde{p}}_s(k_x, R, n) = -\frac{\partial}{\partial r} \tilde{\tilde{p}}_i(k_x, R, n) \tag{98}$$

where $\tilde{\tilde{p}}_s$ is the 2D Fourier transform of the scattered pressure, and $k_r^2 = k_0^2 - k_x^2$. For a given k_x and n, Eq. (97) corresponds to Bessel's differential equation, which solutions can be written with Hankel's functions of the first and second kind of order n, $H_n^{(1)}$ and $H_n^{(2)}$ respectively:

$$\tilde{\tilde{p}}_s(k_x, r, n) = A_r H_n^{(1)}(k_r r) + B_r H_n^{(2)}(k_r r) \tag{99}$$

The constant A_r and B_r are calculated thanks to the Sommerfeld's radiation condition and the Euler's equation:

$$\begin{cases} A_r = & 0 \\ B_r = & -\frac{1}{k_r H_n^{(2)'}(k_r R)} \frac{\partial}{\partial r} \tilde{\tilde{p}}_i(k_x, R, n) \end{cases} \tag{100}$$

The incident pressure field for a monopole in (x_s, r_s, θ_s) can be expressed by:

$$p_i = p_0 \frac{e^{\mathrm{j}k_0 d}}{d_s} \tag{101}$$

with p_0 the source intensity and d_s the distance between the source and the observation point. Applying a 2D Fourier transform yields [197]:

$$\tilde{\tilde{p}}_i(k_x, r, n) = \mathrm{j}\pi p_0 H_n^{(2)}(k_r r_s) J_n(k_r r) e^{-\mathrm{j}(n\theta_s + k_x x_s)} \quad \text{for } r < r_s \tag{102}$$

Injecting Eq. (102) in Eq. (100) and then in Eq. (99) yields:

$$\tilde{\tilde{p}}_s(k_x, r, n) = -\mathrm{j}\pi p_0 \frac{H_n^{(2)}(k_r r_s) J_n'(k_r R)}{H_n^{(2)'}(k_r R)} H_n^{(2)}(k_r r) e^{-\mathrm{j}(n\theta_s + k_x x_s)} \tag{103}$$

The blocked pressure is deduced by summing the incident and scattered pressure:

$$\tilde{\tilde{p}}_b(k_x, R, n) = \mathrm{j}\pi p_0 \left(J_n(k_r R) - \frac{H_n^{(2)}(k_r R) J_n'(k_r R)}{H_n^{(2)'}(k_r R)} \right) H_n^{(2)}(k_r r_s) e^{-\mathrm{j}(n\theta_s + k_x x_s)} \tag{104}$$

Using that $J_n(z) H_n^{(2)'}(z) - J_n'(z) H_n^{(2)}(z) = -\frac{2\mathrm{j}}{\pi z}$, Eq. (104) can finally be written as:

$$\tilde{\tilde{p}}_b(k_x, R, n) = \frac{2p_0}{k_r R} \frac{H_n^{(2)}(k_r r_s)}{H_n^{(2)'}(k_r R)} e^{-\mathrm{j}(n\theta_s + k_x x_s)} \tag{105}$$

This expression can be used in the right-hand side term of Eq. (8) to determine the free displacements of the shell for a monopole excitation. This method is applied in the next section to discuss the influence of the internal structures on the vibroacoustic behavior of a submerged shell for a random excitation.

6.3 TEST CASE APPLICATION

6.3.1 *Description of the system*

The system presented in section 3.5 is considered for this study. It consists in a 5 m radius, 42.3 m length and 30 mm thick cylindrical shell including 51 stiffeners and 2 spherical bulkheads (10 mm thick, 30 m curvature radius), as shown in Fig. 68. There are three different types of stiffeners and their spacing varies between 0.6 and 1 m. The whole system is made of steel ($\eta = 0.02$) and is immersed in water. Clamped boundary conditions are used at the ends of the shell, 2 m away from the first and the last stiffeners. A non-axisymmetric frame is linking the two stiffeners at $x = 11.5$ m and $x = 21.5$ m. A model of this internal structure is shown in Fig. 33b, with the colors representing the displacement magnitude of the eigenmode at 170 Hz. It consists in a plate assembly made of a horizontal floor, a vertical stiffening plate and two disc sections that are linked to the stiffeners. Displacements continuity is assumed at all the junctions.

In order to use the reciprocity principle, a point force is applied on the surface of the cylindrical shell at the point M_1 of coordinates $(x, r, \theta) = (11.5, 5, 0)$. Similarily, a monopole excitation is defined at the point M_2 of coordinates $(x, r, \theta) = (11.5, 500, 0)$. The response of the system is calculated using the CTF method for both excitations separately, and thanks to the reciprocity principle, the sensitivity functions are given by the response in the wavenumber-frequency space.

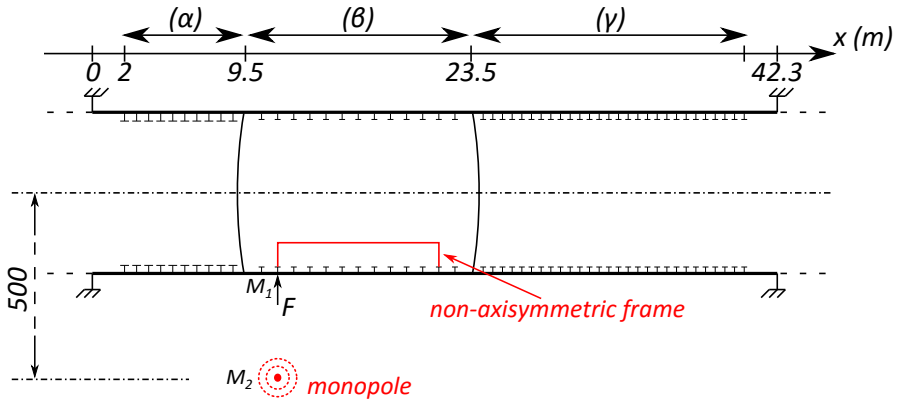

Figure 68: Section in the plane $\theta = 0$ of a submerged cylindrical shell with axisymmetric stiffeners and a non-axisymmetric frame: (α) spacing 0.75 m, T-cross-section (mm): $300 \times 60/60 \times 300$; ($\beta$) spacing 1 m, T-cross-section (mm): $200 \times 15/15 \times 200$; ($\gamma$) spacing 0.6 m, T-cross-section (mm): $200 \times 25/15 \times 200$.

6.3.2 *Examples of sensitivity functions*

Sensitivity functions, *i.e.* accelerations of the shell in the wavenumber space, are calculated thanks to the CTF method for the point force and for the monopole excitation. The results are plotted in Fig. 69 for the point force at $f = 207$ Hz and in Fig. 70 for the monopole excitation at $f = 568$ Hz.

These frequencies are chosen because differences can be clearly seen in the spectra. Indeed, more circumferential orders tend to play a role in the response of the structure when there is a non-axisymmetry [167, 173]. In Fig. 70, the white line represents the radiation circle. The spectral components inside this circle are the main contributors to the pressure radiated in the far-field [178]. No clear difference can be seen inside the

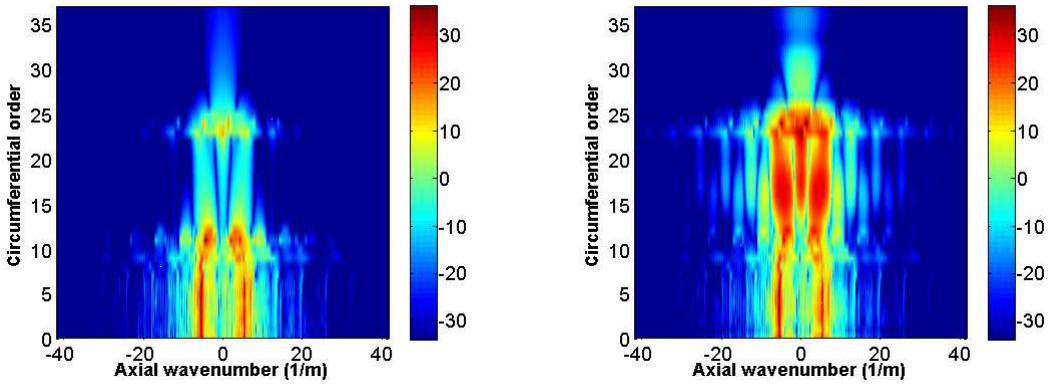

(a) (b)

Figure 69: Sensitivity function (acceleration in dB ref $g\mu m.s^{-2}$) in the wavenumber space for a point force at M_1 at $f = 207$ Hz. (a) Axisymmetric case. (b) Non-axisymmetric case.

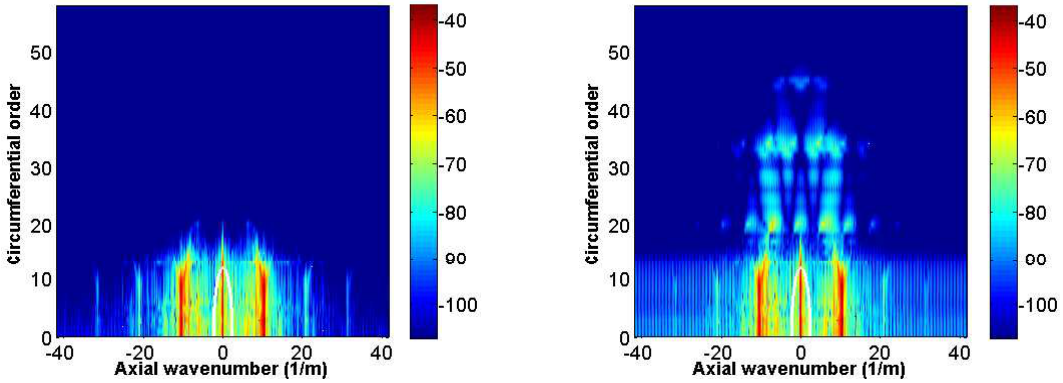

(a) (b)

Figure 70: Sensitivity function (acceleration in dB ref $g\mu m.s^{-2}$) in the wavenumber space for a monopole at M_2 at $f = 568$ Hz. (a) Axisymmetric case. (b) Non-axisymmetric case.

radiation circle at this frequency, so no large difference is expected in the PSD of the pressure at M_2.

6.3.3 *Diffuse Sound Field excitation*

As the radius of curvature of the shell is large compared with the wavelength, the expression of a DSF for a plate in the wavenumber-frequency space is taken [198]:

$$\phi_{pp}(k_x, k_y, f) = \begin{cases} \frac{\pi}{k_0^{in}} \frac{S_{pp}(f)}{\sqrt{(k_0^{in})^2 - (k_x^2 + k_y^2)}} & \text{if } \sqrt{k_x^2 + k_y^2} < k_0^{in} \\ 0 & \text{if } \sqrt{k_x^2 + k_y^2} \geq k_0^{in} \end{cases} \tag{106}$$

where k_y is linked to the circumferential order n by $k_y = \frac{n}{R}$. S_{pp} is the frequency spectral density, taken constant equal to 1 $Pa^2.s$ in this example. $k_0^{in} = \frac{2\pi f}{c_0^{in}}$ is the acoustic wavenumber. Air is considered inside the cylindrical shell (with weak coupling only) and the sound velocity is taken equal to $c_0^{in} = 340$ $m.s^{-1}$. ϕ_{pp} is plotted in the wavenumbers space for $f = 207$ Hz in Fig. 71a. Maxima can be seen for wavenumbers close to the acoustic wavenumber k_0^{in}. These maxima are represented by the black line and are added to the plot in Fig. 69b to yield Fig. 71b. It is clear that the non-axisymmetric frame plays a role at this frequency and for this excitation, especially close to $(k_x, n) = (0, 20)$.

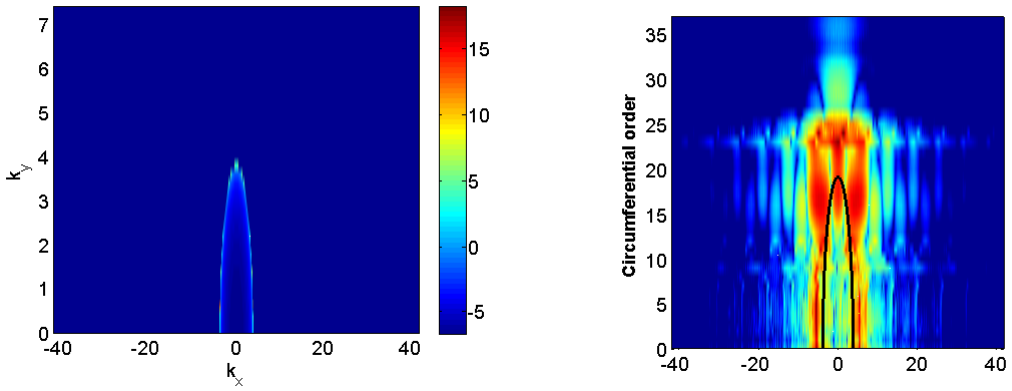

(a) (b)

Figure 71: (a) PSD for a DSF at $f = 207$ Hz. (b) Sensitivity function for a point force at M_1 for the non-axisymmetric case at $f = 207$ Hz.

In this example, the DSF excites only the cylinder on the section between the two bulkheads at $x = 9.5$ and $x = 23.5$ m. According to the reciprocity principle and to Eq. (91) (respectively Eq. (92)) , it consists in calculating the spectral displacements of the structure for a point force at $\mathbf{x}$ (resp. for a monopole excitation at $\mathbf{z}$) only on $\check{\mathbf{x}} \in \Sigma_p$.

Fig. 72 shows the PSD of the radial acceleration at M_1 and pressure at M_2 as a function of the frequency with and without the non-axisymmetric internal frame. The red solid line shows the results for the case of the axisymmetric stiffened shell (*i.e.* the stiffened submerged shell without the internal frame) and the blue dashed line shows the case where the non-axisymmetric frame is taken into account. It can be said that the non-

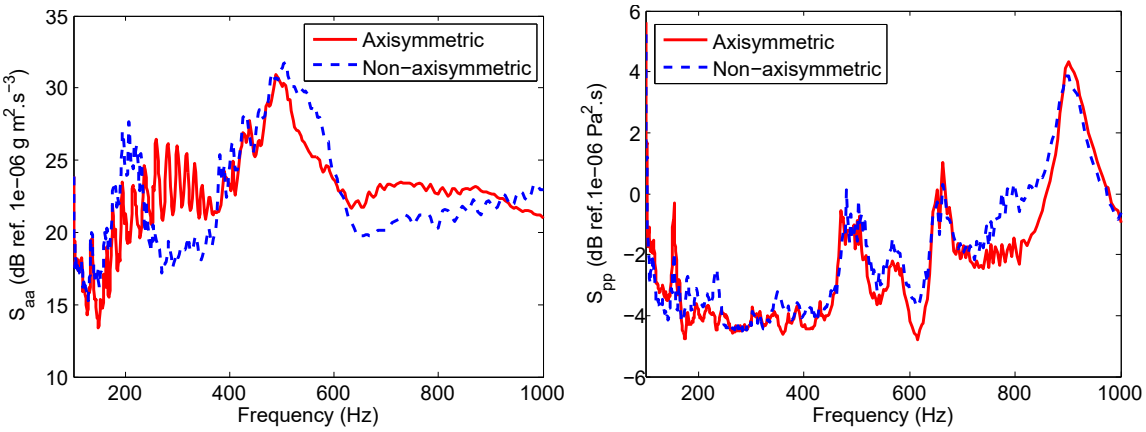

(a) (b)

Figure 72: PSD of the system excited by a DSF with and without the non-axisymmetric internal structure as a function of the frequency of the (a) radial acceleration at M_1 and (b) pressure at M_2.

axisymmetric internal frame has an influence on the response of the structure when it is excited by the DSF. For the acceleration at M_1, the PSD tends to decrease except for some frequency ranges. The decrease can be explained from the reciprocity principle, by saying that the amplitude of displacement is on average lower in the non-axisymmetric case [173, 179]. The increases can be explained by looking at the sensity functions shown in Fig. 69 and 71b where more circumfenential orders play a role in the non-axisymmetric case. For the PSD of pressure at M_2, an increase smaller than 2 dB can be seen.

6.3.4 *Turbulent Boundary Layer excitation*

A structure immersed in a flow can be excited by a TBL which is characterized by the parameters shown in Table 3 [199]. These parameters can be calculated using Computational Fluid Dynamics (CFD) calculations. This is however not the aim of the present work and the values have thus been arbitrarily chosen for naval applications, and used in simple models to calculate the wavenumber-frequency spectrum of the wall pressure ϕ_{pp}.

Table 3: Turbulent Boundary Layer parameters

Parameter	Notation	Value
Flow speed	U_∞	15 m.s^{-1}
Friction velocity	U_T	1 m.s^{-1}
Thickness	δ_L	0.01 m
Kinematic viscosity (at 20°C)	ν_0	1.005 μ Pa.s
Fluid density	ρ_0	1000 kg.m^{-3}

The strongest pressure fluctuations occur at the convective wavenumber k_c and the acoustic wavenumber k_0 defined by:

$$k_c = \frac{2\pi f}{U_c} \text{ and } k_0 = \frac{2\pi f}{c_0} \tag{107}$$

where U_c is the convection speed taken as $U_c = 0.6U_\infty$ [199, 76] and $c_0 = 1500$ m.s^{-1}. The acoustic, convective and flexural wavenumbers are plotted as a function of the frequency up to 1000 Hz in Fig. 73a. The flexural wavenumber k_f is calculated for a $h = 0.03$ m thick plate made of steel (density $\rho_s = 7800$ kg.m^{-3}, Young modulus $E = 210$ GPa and Poisson coefficient $\nu = 0.3$) using Eq. (71). It can be seen in Fig. 73a that the convective wavenumber is much bigger than the acoustic and flexural wavenumbers for the parameters chosen for this study. On the other hand, the radial accelerations of a cylinder above the ring frequency (see Eq. (5)) present generally maxima for wavenumbers around the flexural wavenumber and then decreases when the wavenumber increases. Fig. 73b shows the module of the radial acceleration as a func-

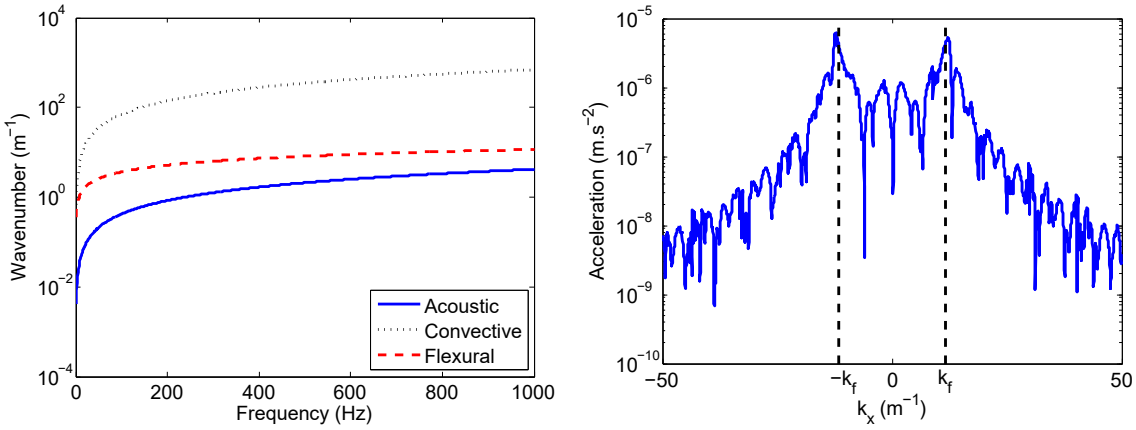

(a) (b)

Figure 73: (a) Acoustic (blue solid line), convective (black dotted line) and flexural (red dashed line) wavenumbers as a function of the frequency. (b) Radial acceleration as a function of the axial wavenumber k_x at 1000 Hz for the circumferential order $n = 0$ and for a point force at M_1

tion of the axial wavenumber for the circumferential order $n = 0$ at the frequency $f = 1000$ Hz. It clearly shows that the amplitude is maximum at the flexural wavenumber k_f, and then drops dramatically. It can thus be said that the structure acts as a filter on the high wavenumbers and that the vibrations are mainly due to the acoustic components of the TBL. As mentioned at the end of section 6.1, a cutoff wavenumber $\mathbf{N_k}$ can be defined from the flexural wavenumber and a margin coefficient to numerically calculate the integrals of Eqs. (87) and (89). In this example, the margin coefficients are taken equal to 4 for the axial wavenumbers and 1.2 for the circumferential orders.

In the present study, the wavenumber-frequency spectrum of the wall pressure $\phi_{pp}(k_x, k_y, f)$ is expressed as:

$$\phi_{pp}(k_x, k_y, f) = S_{pp}^{TBL}(f)\Psi_{pp}(k_x, k_y, f) \tag{108}$$

An empirical model proposed by Goody [200] is used for the frequency spectral density $S_{pp}^{TBL}(f)$:

$$S_{pp}^{TBL}(f) = \frac{4\pi C_2 \tau_w^2 (2\pi f)^2 \delta_L^3}{U_\infty^3 \left(\left[C_1 + \left(\frac{2\pi f \delta_L}{U_\infty} \right)^{0.75} \right]^{3.7} + \left[C_3 R_T^{-0.57} \left(\frac{2\pi f \delta_L}{U_\infty} \right) \right]^7 \right)} \tag{109}$$

where C_1, C_2 and C_3 are respectively 0.5, 1.5 and 1.1. $R_T = \frac{U_T^2 \delta_L}{\nu_0 U_\infty}$ is the Reynolds' number that takes into account the ratio of intertial forces to viscous forces. $\tau_w = \rho_0 U_T^2$ is the shear constraint at the wall. The cross-spectrum $\Psi_{pp}(k_x, k_y, f)$ is deduced from a spatial Fourier transform of the expression given by Corcos [72] and yields:

$$\Psi_{pp}(k_x, k_y, f) = \frac{4\alpha\beta}{\left[\left(k_x - \frac{2\pi f}{U_c}\right)^2 + \left(\frac{2\pi f \alpha}{Uc}\right)^2\right]\left[k_y^2 + \left(\frac{2\pi f \beta}{Uc}\right)^2\right]} \tag{110}$$

with $\alpha = 0.11$ and $\beta = 0.77$ empirical values.

The PSD of the acceleration at M_1 and of the pressure at M_2 are plotted as a function of the frequency in Fig. 74a and 74b respectively. Similarily to the results from the DSF, it

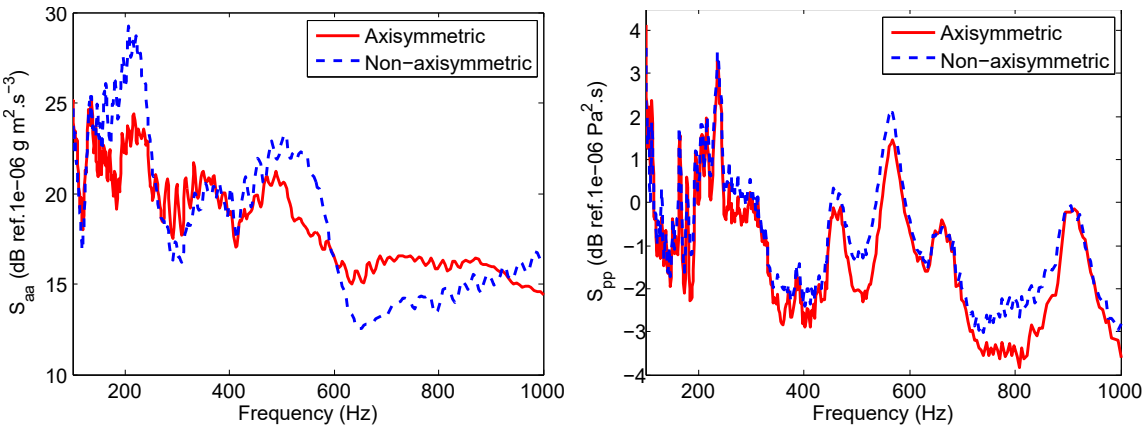

(a) (b)

Figure 74: PSD of the system excited by a TBL with and without the non-axisymmetric internal structure as a function of the frequency of the (a) radial acceleration at M_1 and (b) pressure at M_2.

can be said that the non-axisymmetric internal frame has an influence on the response of the system when it is excited by a TBL. Differences up to 6 dB can be seen in Fig. 74a for the PSD of acceleration at M_1 between the axisymmetric and non-axisymmetric cases. For the PSD of pressure at M_2 shown in Fig. 74b, the differences between the two cases are smaller. No clear difference can be seen below 250 Hz, and the non-axisymmetric case is between 1 and 2 dB higher in the rest of the frequency range.

6.4 CONCLUSIONS

A powerful tool has been developed to calculate the response of a submerged stiffened cylindrical shell with non-axisymmetric internal frames for random excitations. For this purpose, the wavenumber-point (k, M) reciprocity technique has been presented and is based on sensitivity functions, that are the result of deterministic calculations of the system for a point force or a monopole, estimated with the CTF method. One of the main advantage of this approach is that once the sensitivity functions are stored in a database, it is easy to change the excitation by modifying the expression of the wall pressure spectrum ϕ_{pp}. Random mechanical excitations could be included using the same technique.

An application on a test case taken from the naval industry for different random excitations (DSF, TBL) shows the versatility of the method. From the results it can be said that the non-axisymmetric internal frames can have an influence on the response of the system for random excitations. As more circumferential orders tend to play a role when the system is non-axisymmetric, the response tends to be higher in this case. The method can now be used to further investigate physical phenomena (Bloch-Floquet waves propagation for instance) involved in a stiffened submerged cylindrical shell for random excitations.

GENERAL CONCLUSIONS AND FURTHER WORK

This work has focused on the vibroacoustic modeling of a cylindrical shell with heavy fluid loading and coupled to internal structures. A substructuring approach has been developed for thin mechanical structures coupled along lines. It consists in projecting the displacements and forces at the junction on a set of orthonormal condensation functions to yield CTF of the uncoupled subsystems. The superposition principle, the force equilibrium and the displacement continuity allow writing the coupling between the subsystems in order to deduce the vibroacoustic behavior of the entire system. A criterion has been defined on the size of the condensation functions set to ensure good convergence of the method. Providing that the forces and displacements are properly approximated by the set of condensation functions, the CTF method is based on continuity equations and has thus no frequency limitation, as long as the mechanical systems can be described by shell elements and the junctions considered as lines.

The CTF approach has the advantage of being able to couple together subsystems that are described by different methods. In this work, more attention has been paid to the case of a submerged cylindrical shell described by a semi-analytical method, coupled to internal frames described by the FEM, allowing complex geometries. Examples were given to show the interest of the tool for industrial applications. It gives the possibility to study subsystems that are characterized by different methods (numerical, analytical, experimental ...) before assembling them, according to an industrial organizational process. Moreover, when the system is submerged in water, the mid frequency range (up to $k_0 R \simeq 40$) has been reached at reasonable computational cost (*i.e.* a few minutes for a single frequency on a working station). Besides, the versatility of the method has been illustrated: several non-axisymmetric internal frames have been considered, and several excitations have been successively taken into account. In this work, the systems were symmetric and the coupling line were at constant radial and axial coordinates. It is clear that the CTF method is still valid in non-symmetric configurations and with any junctions between subsystems. More computational effort is however required, as non-symmetries imply that the negative circumferential orders need also to be calculated,

and the axisymmetric properties of the stiffened shell cannot be used if the junction is not along the circumference.

The CTF method has been used to point out physical phenomena involved in the vibroacoustic behavior of a complex submerged cylindrical shell. More particularly, attention has been paid to the influence of non-axisymmetric internal frames on the vibroacoustic behavior of the system. First, for the case of a point force, it was shown that more circumferential orders play a role in the response of the cylindrical shell. More especially, the low circumferential orders contribute to the far-field radiated pressure and the radiation efficiency tends thus to increase when there are non-axisymmetries. Besides, the addition of a large number of internal DOF and the impedance match between the subsystems can lead to an apparent damping effect. Experiments have been conducted on a model in air. The trends observed in the numerical simulations have been verified below the coincidence frequency. Then, acoustical excitation has been considered for the case of a stiffened submerged cylindrical shell impinged by a plane wave. The scattering phenomena from this system can be modified by the internal frames. Indeed, it was shown that structural waves can propagate in the internal frames and give rise to additional interference phenomena. Finally, a tool to study the response of a complex system under random pressure fields has been presented. Based on the wavenumber-point (k, M) reciprocity technique, it requires the expression of the PSD of the excitation pressure field and the knowledge of sensitivity functions of the structure. The CTF method has been used for the calculation of the sensitivity functions and the influence of the non-axisymmetric internal frames has been discussed.

The method described in this work presents however some limitations. Indeed, the semi-analytical method used to describe the submerged cylindrical shell is based on the Flügge equations for an infinitely long cylinder. Clamped boundary conditions can be added at the ends of the system by introducing fictive frames with null admittances in order to model the finite length of the cylinder. Nevertheless, it means that the shell has a constant thickness, that the cylinder is baffled and that no radiation can be considered from the end caps. Even if the effect of the baffle is supposed to be small on the far-field radiated pressure [26], it would be interesting to investigate the influence of the end caps.

Several perspectives are now considered. First of all, the CTF method should be implemented in a ready-to-use software in order to be applied on the design process of industrial systems. Several geometries of internal structures could thus be tested in order to evaluate their influence and to see their impact on the noise and vibrations requirements. One of the advantages of the substructuring approach is that intermediate results (the CTF of the axisymmetric shell for instance) can be stored in a database, allowing reanalysis at low computational cost.

The experimental campaign started in chapter 4 could be conducted further. Indeed, the laser vibrometer being able to measure at very high frequencies, it could be interesting to check the influence of the non-axisymmetric internal frame well above the ring frequency. If besides the model is submerged in water, the frequency range between the ring frequency and the coincidence frequency is wider than in air, and it is more likely to see the effect of the internal frame on the vibroacoustic behavior of the shell.

As a perspective of chapter 5, an experimental campaign should be led to measure the scattering from a target with non-axisymmetric internal frames. The model with the internal plates could be investigated in a water tank, with particular attention paid to the observation of the supplementary Bloch-Floquet trajectories highlighted in the numerical models.

The tool presented in chapter 6 should be used to study the influence of the structural complexity of a shell under random excitations. Indeed, little attention has been paid to the influence of the periodic stiffeners on the response of a shell under spatially distributed and random excitations. One can wonder if phenomena such as pass- and stop-bands plays a significant role on the radiated pressure of periodically stiffened shell under this type of excitation. Moreover, the influence of non-axisymmetric frames on the pass- and stop-band phenomena can be investigated.

The formalism of the CTF method could be extended to deal with surface coupling between two mechanical structures, by defining two variables condensation functions. If the coupling surfaces are divided in patches, a parallel with the PTF approach, which is so far limited to interfaces with acoustic medium, can be done. This could be used for instance to take into account masking or anechoic coating on the shell.

A

FLÜGGE EQUATIONS IN THE WAVENUMBER DOMAIN

The spectral Flügge equations are derived in this appendix. Solutions are first given for the *in vacuo* case A.1, and then taking heavy fluid loading into account A.2.

A.1 EQUATIONS *in vacuo*

A 2D-Fourier transform is applied to the Flügge equations (1a)-(1c) and yields:

$$\begin{bmatrix} \tilde{\tilde{Z}}_{UU} & \tilde{\tilde{Z}}_{UV} & \tilde{\tilde{Z}}_{UW} \\ \tilde{\tilde{Z}}_{UV} & \tilde{\tilde{Z}}_{VV} & \tilde{\tilde{Z}}_{VW} \\ \tilde{\tilde{Z}}_{UW} & \tilde{\tilde{Z}}_{VW} & \tilde{\tilde{Z}}_{WW} \end{bmatrix} \begin{bmatrix} \tilde{\tilde{U}} \\ \tilde{\tilde{V}} \\ \tilde{\tilde{W}} \end{bmatrix} = \frac{(1-\nu^2)R^2}{Eh} \begin{bmatrix} -\tilde{\tilde{L}}_f \\ -\tilde{\tilde{T}} \\ \tilde{\tilde{F}} + \mathrm{j}k_x \tilde{\tilde{M}}_T \end{bmatrix} \tag{111}$$

where

$$\begin{aligned} \tilde{\tilde{Z}}_{UU} &= -R^2k_x^2 - k_\theta^2 \frac{1-\nu}{2}(1+\beta^2) + R^2k_l^2 \\ \tilde{\tilde{Z}}_{UV} &= -R\frac{1+\nu}{2}k_\theta k_x \\ \tilde{\tilde{Z}}_{UW} &= \mathrm{j}k_x \left(R\nu + \beta^2 R^3 k_x^2 - \beta^2 R \frac{1-\nu}{2} k_\theta^2 \right) \\ \tilde{\tilde{Z}}_{VV} &= -R^2k_x^2 \frac{1-\nu}{2}(1+3\beta^2) - k_\theta^2 + R^2k_l^2 \\ \tilde{\tilde{Z}}_{VW} &= \mathrm{j}k_\theta \left(1 + \beta^2 R^2 \frac{3-\nu}{2} k_x^2 \right) \\ \tilde{\tilde{Z}}_{WW} &= 1 + \beta^2 \left(R^4k_x^4 + k_\theta^2(2R^2k_x^2+2) + k_\theta^4 + 1 \right) - R^2k_l^2 \end{aligned} \tag{112}$$

It is reminded that $\beta = \frac{h}{R\sqrt{12}}$ and $k_l = \omega\sqrt{\frac{\rho_s(1-\nu^2)}{E}}$. The solutions for the spectral displacements $\tilde{U}$, $\tilde{V}$ and $\tilde{W}$ are:

$$\begin{aligned} \tilde{U} &= -\gamma \frac{\tilde{\tilde{Z}}_{VV}\tilde{\tilde{Z}}_{WW} - \tilde{\tilde{Z}}_{VW}^2}{\tilde{\tilde{\Delta}}_v} \tilde{\tilde{L}}_f \\ &\quad -\gamma \frac{\tilde{\tilde{Z}}_{UV}\tilde{\tilde{Z}}_{UW} - \tilde{\tilde{Z}}_{UU}\tilde{\tilde{Z}}_{VW}}{\tilde{\tilde{\Delta}}_v} \tilde{\tilde{T}} \\ &\quad +\gamma \frac{\tilde{\tilde{Z}}_{UV}\tilde{\tilde{Z}}_{VW} - \tilde{\tilde{Z}}_{VV}\tilde{\tilde{Z}}_{UW}}{\tilde{\tilde{\Delta}}_v} (\tilde{\tilde{F}} + \mathrm{j}k_x \tilde{\tilde{M}}_T) \end{aligned} \tag{113}$$

$$\begin{aligned}\tilde{\tilde{V}} &= -\gamma\frac{\tilde{\tilde{Z}}_{VW}\tilde{\tilde{Z}}_{UW}-\tilde{\tilde{Z}}_{WW}\tilde{\tilde{Z}}_{UV}}{\tilde{\tilde{\Delta}}_v}\tilde{L}_f \\ &\quad -\gamma\frac{\tilde{\tilde{Z}}_{UU}\tilde{\tilde{Z}}_{WW}-\tilde{\tilde{Z}}_{UW}^2}{\tilde{\tilde{\Delta}}_v}\tilde{T} \\ &\quad +\gamma\frac{\tilde{\tilde{Z}}_{UW}\tilde{\tilde{Z}}_{UV}-\tilde{\tilde{Z}}_{UU}\tilde{\tilde{Z}}_{VW}}{\tilde{\tilde{\Delta}}_v}(\tilde{\tilde{F}}+\mathrm{j}k_x\tilde{\tilde{M}}_T)\end{aligned} \tag{114}$$

$$\begin{aligned}\tilde{\tilde{W}} &= -\gamma\frac{\tilde{\tilde{Z}}_{UV}\tilde{\tilde{Z}}_{VW}-\tilde{\tilde{Z}}_{UW}\tilde{\tilde{Z}}_{VV}}{\tilde{\tilde{\Delta}}_v}\tilde{L}_f \\ &\quad -\gamma\frac{\tilde{\tilde{Z}}_{UW}\tilde{\tilde{Z}}_{UV}-\tilde{\tilde{Z}}_{VW}\tilde{\tilde{Z}}_{UU}}{\tilde{\tilde{\Delta}}_v}\tilde{T} \\ &\quad +\gamma\frac{\tilde{\tilde{Z}}_{UU}\tilde{\tilde{Z}}_{VV}-\tilde{\tilde{Z}}_{UV}^2}{\tilde{\tilde{\Delta}}_v}(\tilde{\tilde{F}}+\mathrm{j}k_x\tilde{\tilde{M}}_T)\end{aligned} \tag{115}$$

where

$$\gamma=\frac{(1-\nu^2)R^2}{Eh} \tag{116}$$

and

$$\begin{aligned}\tilde{\tilde{\Delta}}_v &= \tilde{\tilde{Z}}_{UW}(\tilde{\tilde{Z}}_{UV}\tilde{\tilde{Z}}_{VW}-\tilde{\tilde{Z}}_{VV}\tilde{\tilde{Z}}_{UW})+\tilde{\tilde{Z}}_{VW}(\tilde{\tilde{Z}}_{UW}\tilde{\tilde{Z}}_{UV}-\tilde{\tilde{Z}}_{VW}\tilde{\tilde{Z}}_{UU}) \\ &\quad +\tilde{\tilde{Z}}_{WW}(\tilde{\tilde{Z}}_{UU}\tilde{\tilde{Z}}_{VV}-\tilde{\tilde{Z}}_{UV}^2)\end{aligned} \tag{117}$$

The spectral tangential rotation $\tilde{\varphi}$ is deduced from the 2D Fourier transform of $\varphi=\frac{\partial W}{\partial x}$:

$$\tilde{\varphi}=\mathrm{j}k_x\tilde{W} \tag{118}$$

A.2 EQUATIONS WITH HEAVY FLUID LOADING

The fluid loading is added in the Flügge equation governing the radial component (Eq. (8)). The spectral form of the system (1a)-(1b)-(8) can be written with a spectral pressure term $\tilde{p}$ in the right-hand term [21]:

$$\begin{bmatrix}\tilde{\tilde{Z}}_{UU} & \tilde{\tilde{Z}}_{UV} & \tilde{\tilde{Z}}_{UW}\\ \tilde{\tilde{Z}}_{UV} & \tilde{\tilde{Z}}_{VV} & \tilde{\tilde{Z}}_{VW}\\ \tilde{\tilde{Z}}_{UW} & \tilde{\tilde{Z}}_{VW} & \tilde{\tilde{Z}}_{WW}\end{bmatrix}\begin{bmatrix}\tilde{U}\\ \tilde{V}\\ \tilde{W}\end{bmatrix}=\frac{(1-\nu^2)R^2}{Eh}\begin{bmatrix}-\tilde{L}_f\\ -\tilde{T}\\ \tilde{F}+\mathrm{j}k_x\tilde{M}_T\end{bmatrix}-\frac{(1-\nu^2)R^2}{Eh}\begin{bmatrix}0\\ 0\\ \tilde{p}\end{bmatrix}$$

(119)

where $\tilde{\tilde{Z}}_{uu}$, $\tilde{\tilde{Z}}_{uv}$, $\tilde{\tilde{Z}}_{uw}$, $\tilde{\tilde{Z}}_{vv}$, $\tilde{\tilde{Z}}_{vw}$ and $\tilde{\tilde{Z}}_{ww}$ are the same than in Eqs. (112).

Injecting Eq. (11) into Eq. (119) yields a linear system which solutions for the spectral displacements $\tilde{U}$, $\tilde{V}$ and $\tilde{W}$ are:

$$\begin{aligned}\tilde{U} &= -\gamma\frac{\tilde{\tilde{Z}}_{vv}(\tilde{\tilde{Z}}_{ww}+\gamma\tilde{\tilde{Z}}_f)-\tilde{\tilde{Z}}_{vw}^2}{\tilde{\tilde{\Delta}}}\tilde{\tilde{L}}_f \\ &\quad -\gamma\frac{\tilde{\tilde{Z}}_{uv}\tilde{\tilde{Z}}_{uw}-\tilde{\tilde{Z}}_{uu}\tilde{\tilde{Z}}_{vw}}{\tilde{\tilde{\Delta}}}\tilde{\tilde{T}} \\ &\quad +\gamma\frac{\tilde{\tilde{Z}}_{uv}\tilde{\tilde{Z}}_{vw}-\tilde{\tilde{Z}}_{vv}\tilde{\tilde{Z}}_{uw}}{\tilde{\tilde{\Delta}}}(\tilde{\tilde{F}}+\mathrm{j}k_x\tilde{\tilde{M}}_T)\end{aligned} \tag{120}$$

$$\begin{aligned}\tilde{V} &= -\gamma\frac{\tilde{\tilde{Z}}_{vw}\tilde{\tilde{Z}}_{uw}-(\tilde{\tilde{Z}}_{ww}+\gamma\tilde{\tilde{Z}}_f)\tilde{\tilde{Z}}_{uv}}{\tilde{\tilde{\Delta}}}\tilde{\tilde{L}}_f \\ &\quad -\gamma\frac{\tilde{\tilde{Z}}_{uu}(\tilde{\tilde{Z}}_{ww}+\gamma\tilde{\tilde{Z}}_f)-\tilde{\tilde{Z}}_{uw}^2}{\tilde{\tilde{\Delta}}}\tilde{\tilde{T}} \\ &\quad +\gamma\frac{\tilde{\tilde{Z}}_{uw}\tilde{\tilde{Z}}_{uv}-\tilde{\tilde{Z}}_{uu}\tilde{\tilde{Z}}_{vw}}{\tilde{\tilde{\Delta}}}(\tilde{\tilde{F}}+\mathrm{j}k_x\tilde{\tilde{M}}_T)\end{aligned} \tag{121}$$

$$\begin{aligned}\tilde{W} &= -\gamma\frac{\tilde{\tilde{Z}}_{uv}\tilde{\tilde{Z}}_{vw}-\tilde{\tilde{Z}}_{uw}\tilde{\tilde{Z}}_{vv}}{\tilde{\tilde{\Delta}}}\tilde{\tilde{L}}_f \\ &\quad -\gamma\frac{\tilde{\tilde{Z}}_{uw}\tilde{\tilde{Z}}_{uv}-\tilde{\tilde{Z}}_{vw}\tilde{\tilde{Z}}_{uu}}{\tilde{\tilde{\Delta}}}\tilde{\tilde{T}} \\ &\quad +\gamma\frac{\tilde{\tilde{Z}}_{uu}\tilde{\tilde{Z}}_{vv}-\tilde{\tilde{Z}}_{uv}^2}{\tilde{\tilde{\Delta}}}(\tilde{\tilde{F}}+\mathrm{j}k_x\tilde{\tilde{M}}_T)\end{aligned} \tag{122}$$

with

$$\begin{aligned}\tilde{\tilde{\Delta}} &= \tilde{\tilde{Z}}_{uw}(\tilde{\tilde{Z}}_{uv}\tilde{\tilde{Z}}_{vw}-\tilde{\tilde{Z}}_{vv}\tilde{\tilde{Z}}_{uw})+\tilde{\tilde{Z}}_{vw}(\tilde{\tilde{Z}}_{uw}\tilde{\tilde{Z}}_{uv}-\tilde{\tilde{Z}}_{vw}\tilde{\tilde{Z}}_{uu}) \\ &\quad +(\tilde{\tilde{Z}}_{ww}+\gamma\tilde{\tilde{Z}}_f)(\tilde{\tilde{Z}}_{uu}\tilde{\tilde{Z}}_{vv}-\tilde{\tilde{Z}}_{uv}^2)\end{aligned} \tag{123}$$

The spectral tangential rotation $\tilde{\tilde{\varphi}}$ is:

$$\tilde{\tilde{\varphi}} = \mathrm{j}k_x\tilde{W} \tag{124}$$

B

FREQUENCY RANGE CALCULATION

In a frequency response, the width $\Delta f(f_0)$ at -3 dB of a resonance peak at f_0 is linked to the structural damping η as follows [180]:

$$\frac{\Delta f}{f_0} = \eta. \tag{125}$$

Besides, the Matlab command `freq=logspace(`a, b, N_f`)` yields a vector of N_f logarithmically spaced values between 10^a and 10^b. The ratio between two consecutive values is thus given by:

$$\frac{f_{i+1}}{f_i} = 10^{\frac{b-a}{N}}, \forall i \in [\![1; N_f - 1]\!]. \tag{126}$$

To ensure to describe properly the peaks, at least two points should be taken in the band around the resonance:

$$\frac{f_{i+1} - f_i}{f_i} < \frac{1}{2}\frac{\Delta f(f_i)}{f_i} = \frac{\eta}{2}. \tag{127}$$

Injecting Eq. 126 in Eq. 127 yields:

$$N_f > \frac{b-a}{\log_{10}\left(1 + \frac{\eta}{2}\right)}. \tag{128}$$

Taking for instance $a = 1$ (10 Hz), $b = 3.18$ (1500 Hz) and $\eta = 0.02$ gives $N_f > 253$.

C

PROPERTIES OF FOURIER SERIES FOR SYMMETRICAL SYSTEMS

Let us consider a symmetric system in the cylindrical coordinates, as shown for a fixed coordinate x in Fig. 75. The axis going through the center of the cylinder and through the excitation point is the symmetry or anti-symmetry axis, depending on the direction of the excitation. If the system is excited by a radial or axial force or by a tangential moment, the radial response is symmetric with regard to this axis. Similarly, if the system is excited by a tangential force or by a radial or axial moment, the radial response is anti-symmetric.

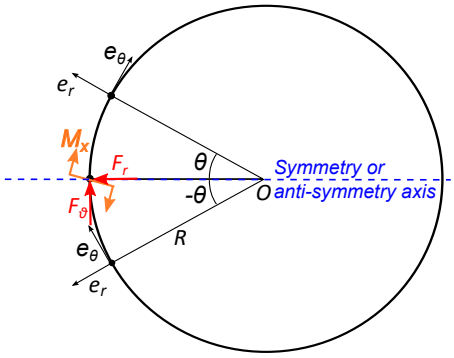

Figure 75: Symmetry and antisymmetry on a system under a point force or moment.

In terms of Fourier coefficients, this means for a symmetric configuration:

$$\begin{aligned}
\tilde{Y}^2(-n) &= \frac{1}{2\pi}\int_{-\pi}^{\pi} Y^2(\theta)e^{-\mathrm{j}n\theta}d\theta \\
&= -\frac{1}{2\pi}\int_{\pi}^{-\pi} Y^2(-\theta)e^{-\mathrm{j}n(-\theta)}d\theta \\
&= \frac{1}{2\pi}\int_{-\pi}^{\pi} Y^2(\theta)e^{-\mathrm{j}(-n)\theta}d\theta \\
&= \tilde{Y}^2(n)
\end{aligned} \tag{129}$$

The Fourier series can thus be expressed with:

$$\begin{aligned} Y^2(\theta) &= \sum_{n=-\infty}^{+\infty} \tilde{Y}^2(n) e^{\mathrm{j}n\theta} \\ &= \sum_{n=-\infty}^{-1} \tilde{Y}^2(n) e^{\mathrm{j}n\theta} + \tilde{Y}^2(0) + \sum_{n=1}^{+\infty} \tilde{Y}^2(n) e^{\mathrm{j}n\theta} \\ &= \tilde{Y}^2(0) + \sum_{n=1}^{+\infty} \tilde{Y}^2(n) (e^{\mathrm{j}n\theta} + e^{-\mathrm{j}n\theta}) \\ &= \tilde{Y}^2(0) + 2 \sum_{n=1}^{+\infty} \tilde{Y}^2(n) \cos(n\theta) \end{aligned} \tag{130}$$

In a similar manner, for an anti-symmetric configuration:

$$\tilde{Y}^2(-n) = -\tilde{Y}^2(n) \tag{131}$$

Consequently, $\tilde{Y}^2(0) = 0$, and the Fourier series yield:

$$Y^2(\theta) = 2\mathrm{j} \sum_{n=1}^{+\infty} \tilde{Y}^2(n) \sin(n\theta) \tag{132}$$

These equations allow to calculate the response of a symmetric system through its Fourier series by knowing only the Fourier coefficients for $n \in \mathbb{N}$.

D

EXPERIMENTAL WORK: ASSEMBLING TWO PLATES PERPENDICULARLY

In the frame of the experimental work presented in chapter 4, the question on how to assemble two thin mechanical structures arises. Several requirements need to be met:

- the displacements continuity should be verified (*i.e.* rigid connection) and no damping should be introduced;
- the junction should be strong enough to resist to the subsystems weight;
- the assembly should be possible even if the access to one of the subsystems is difficult;
- the process should not damage the subsystems;
- the assembly could be unmounted once the measurements done.

D.1 PRESENTATION OF THE TEST SAMPLES

Let us consider two square plates (side $a_p = 100$ mm) made of steel. Plate 1 is $h_1 = 1.5$ mm thick and plate 2 is $h_2 = 1$ mm thick. A sample is defined as the assembly of the two plates. They are placed perpendicularly so that the plate 2 is at the center of one side of plate 1, as shown in Fig. 76. Different solutions are considered to assemble the two plates:

- Soldering (using stain-lead alloy at around 200°C)
- Brazing (using silver alloy at around 600°C)
- Structural adhesive Loctite AA330 (acrylic with activator)
- Structural adhesive SCIGRIP SG5000-06 (two-part methacrylate)

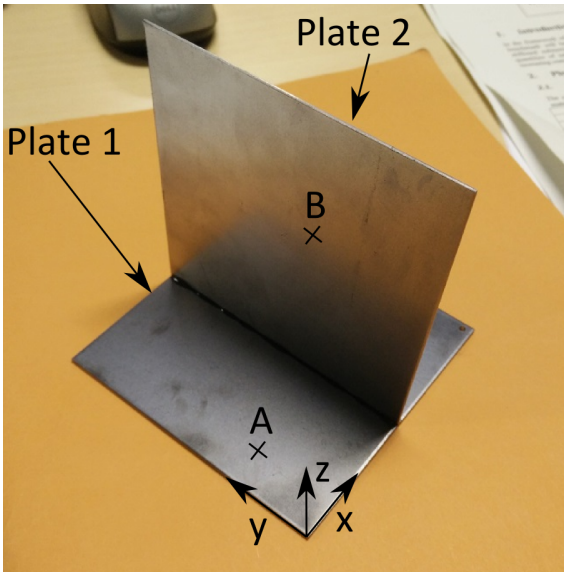

Figure 76: Picture of a sample made of two plates perpendicularly assembled.

- Loctite 454 Prism Instant Adhesive Gel (cyano)

The soldering can immediately be excluded because the junction is too fragile and cannot withstand efforts. The other solutions do not go through resistance test rigs but can be manipulated without breaking. However, the first sample using the adhesive Loctite AA330 broke. The assembly process has then been changed by putting weights in order to keep an effort at the junction while the adhesive dries. The visual aspect of the brazing and the adhesive is compared in Fig 77. It can be said that the brazing harms the structure because of the high temperature and is thus not adapted to the problem. Moreover, brazing is not easily conducted when the junction is not easily accessible.

A Cartesian system (x, y, z) with the origin at the bottom corner of plate 1 (see Fig. 76) is defined. Plate 1 lies thus in the plane $z = 0$ and plate 2 in the plane $x = 50$ (in mm). Three points are defined on the plate:

$$\text{A}: \ (x, y, z) = (10, 20, 0)$$

$$\text{B}: \ (x, y, z) = (50, 30, 60)$$

$$\text{C}: \ (x, y, z) = (80, 60, 0)$$

Two holes (2 mm diameter) are drilled in two corners of plate 1 in order to hang the structure by a thread and consider free boundary conditions. An impact hammer is

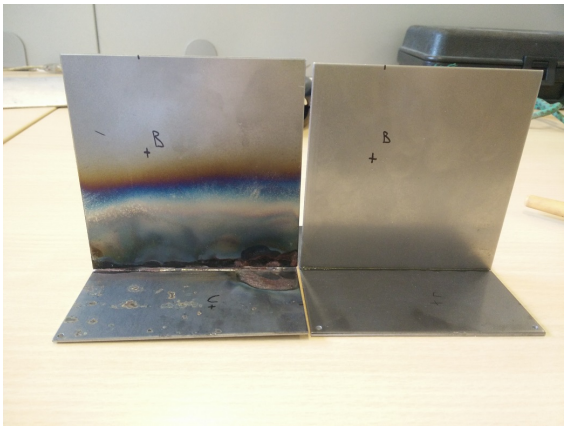

Figure 77: Comparison between brazing and adhesive Loctite AA330.

used to excite the system at the point A in the z direction. An accelerometer is placed successively in B and C to measure the acceleration in the x and z direction, respectively. The transfer function B/A allows to check if the vibrations of plate 1 are transmitted to plate 2 through the junction, and the transfer function C/A allows to check is the influence of plate 2 is taken into account on the behavior of plate 1.

D.2 TRANSFER FUNCTIONS

The transfer functions are plotted in this section as a function of frequency to compare the different solutions considered. As the soldering and brazing are not suitable because of practical reasons, only the three adhesive processes are compared to a numerical model. The numerical model is created with HyperMesh and solved with Nastran. It is made of shell elements, and the elements are smaller than $\lambda/8$ at 20 kHz for plate 2 (more restrictive than plate 1 because of the thickness). Displacements continuity is assumed between the two plates in the numerical model.

The transfer functions B/A and C/A are plotted as functions of the frequency on Figs. 78 and 78 respectively. Below 12 kHz, the three adhesive have a similar behavior. Nevertheless, discrepancies with the numerical simulations can be seen. The differences are explained by the fact that the material characteristics are not exactly known, and that uncertainties can be linked to the plate thicknesses. Besides, the adhesives do not provide perfect displacements continuity at the junction and damping can be introduced. Above 12 kHz, there is a drop in the level measured on the samples. However

this study shows satisfactory overall results and the adhesives can be used to assemble a structure. For practical reasons, the Loctite AA330 is chosen because it is made of two components: the acrylic adhesive is applied on one subsystem and the activator is put on the other one, giving time to adjust the assembly.

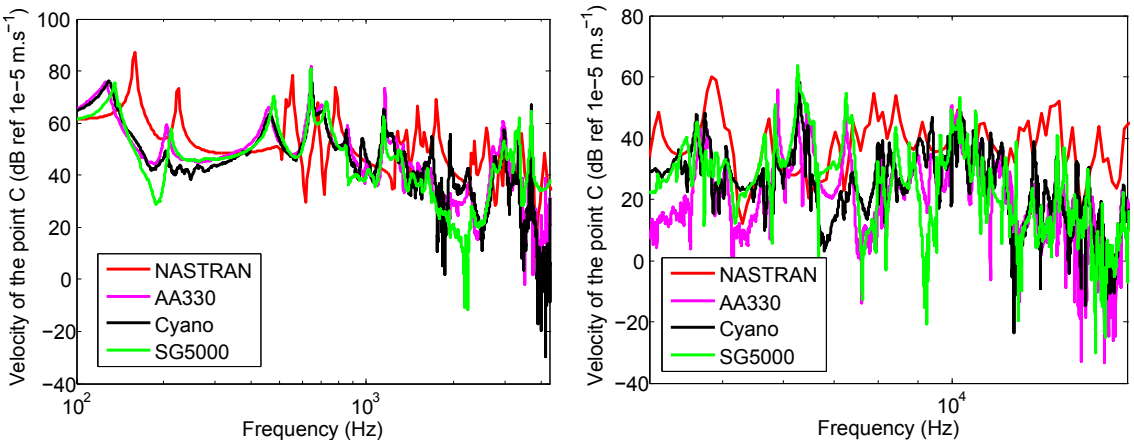

Figure 78: Comparison of the transfer function B/A for three adhesives and a numerical model. (a) Between 100 and 4300 Hz. (b) Between 4 and 17 kHz

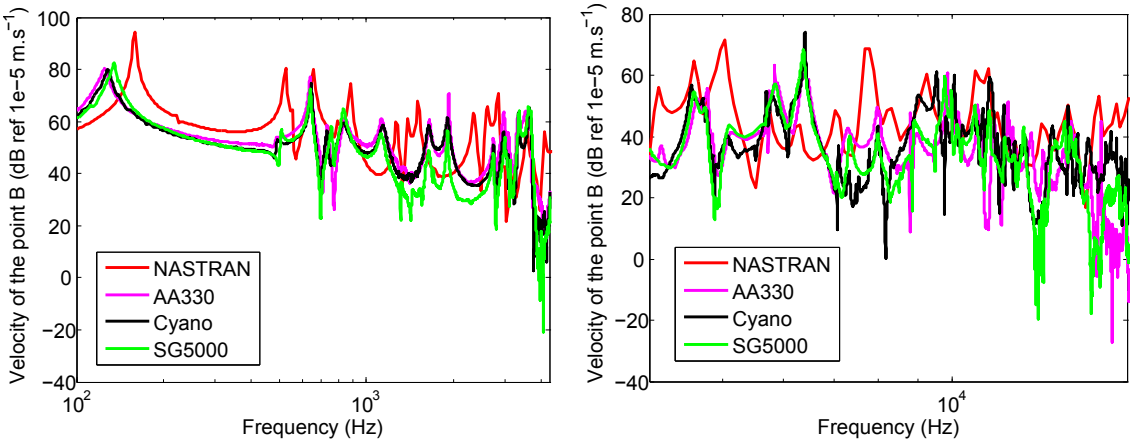

Figure 79: Comparison of the transfer function C/A for three adhesives and a numerical model. (a) Between 100 and 4300 Hz. (b) Between 4 and 17 kHz

E

RÉSUMÉ ÉTENDU EN FRANÇAIS

E.1 CONTEXTE DE L'ÉTUDE

Ces travaux s'inscrivent dans un contexte industriel, où la simulation numérique est aujourd'hui primordiale afin de pouvoir prédire les caractéristiques d'un système avant sa production. En effet, pour des raisons de coût et de délai, il est nécessaire de prendre en compte des exigences sur le bruit et les vibrations d'un produit dès sa phase de conception. Cette étude s'intéresse plus particulièrement à la modélisation de coques cylindriques raidies, très utilisées dans le domaine aéronautique ou naval pour décrire par exemple le fuselage d'un avion ou la coque épaisse d'un véhicule sous-marin (voir Fig. 1). C'est pourquoi de nombreux éléments peuvent être trouvés dans la littérature concernant l'étude du comportement vibro-acoustique d'une coque raidie axisymétrique, avec un éventuel couplage à un fluide lourd. Cependant, on remarque que les systèmes industriels comportent parfois des structures internes non-axisymétriques, qui peuvent avoir une influence sur le comportement vibro-acoustique de la coque cylindrique. D'une part, certaines études analytiques permettent de prendre en compte des plaques ou des systèmes masse-ressort, mais sont en général peu représentatives de la réalité industrielle. D'autre part, les méthodes de discrétisation telle que la méthode des éléments finis permettent de prendre en compte la complexité structurelle du système, mais l'inclusion de non-axisymétries engendre une augmentation considérable des coûts de calcul, et ne permet pas d'obtenir aisément des résultats à moyennes et hautes fréquences.

C'est pourquoi une approche par sous-structuration est développée dans cette thèse. Le but est de prédire numériquement le comportement vibro-acoustique d'une coque cylindrique raidie immergée, couplée à des structures internes non-axisymétriques, tel que représenté sur la Fig. 8. On souhaite connaitre la réponse harmonique sur une gamme fréquentielle allant de quelques Hz à plusieurs kHz pour une application in-

dustrielle (c'est-à-dire pour un rayon de l'ordre de quelques mètres et une longueur de quelques dizaines de mètres). L'idée de la méthode de sous-structuration est de diviser le système en plusieurs sous-systèmes, qui vont être décrits séparément par différentes approches. Cette approche correspond à une logique d'organisation industrielle, où les sous-systèmes sont caractérisés séparément avant d'être assemblés en un système complexe. Ainsi, la coque cylindrique immergée est décrite par la résolution des équations de Flügge dans le domaine des nombres d'onde. Les structures internes axisymétriques telles que les raidisseurs et les cloisons sont modélisées par éléments finis axisymétriques. Les structures internes non-axsiymétriques sont modélisées par éléments finis. Cette subdivision permet de résoudre le problème sur une large gamme fréquentielle, en conservant le couplage avec le fluide extérieur et en ayant une flexibilité sur la géométrie des structures internes. Cette méthode baptisée CTF, pour fonctions de transfert condensées, est décrite dans le prochain paragraphe.

E.2 PRINCIPE DE LA MÉTHODE CTF

La méthode CTF est développée dans le cas général de deux structures mécaniques couplées le long d'une ligne, comme illustré sur la Fig. 10. Cette méthode peut être vue comme une extension de la méthode des admittances (ou mobilités) utilisée dans le cas de systèmes couplés ponctuellement [124]. Un ensemble de fonctions orthonormées, baptisées fonctions de condensation, est défini sur la jonction Γ entre les deux sous-systèmes. Ces fonctions permettent d'approximer les forces et les déplacements au niveau de la jonction pour les sous-systèmes découplés. On désigne par déplacement condensé (resp. force condensée) le déplacement (resp. la force) au niveau de la jonction projeté sur une fonction de condensation. On définit alors des fonctions de transfert condensées comme le rapport d'un déplacement condensé sur une force condensée, pour toutes les combinaisons possibles dans l'ensemble des fonctions de condensation, comme décrit dans l'Eq. (40). Le principe de superposition permet ensuite d'écrire que le déplacement condensé d'un sous-système est la somme de la contribution de la force extérieure et des contributions des forces condensées sur la ligne de couplage (*cf*

Eq. (42)). La continuité des déplacements et l'équilibre des forces à la jonction entre les deux sous-systèmes permettent d'aboutir à l'équation suivante :

$$\left(\mathbf{Y}^1 + \mathbf{Y}^2\right) \mathbf{F}^c = \bar{\mathbf{U}}^2 - \bar{\mathbf{U}}^1 \tag{133}$$

où $\mathbf{Y}^1$ et $\mathbf{Y}^2$ représentent les matrices des fonctions de transfert condensées des deux sous-systèmes, et $\bar{\mathbf{U}}^1$ et $\bar{\mathbf{U}}^2$ sont les vecteurs des déplacements libres condensés (c'est-à-dire les déplacements condensés lorsque les sous-systèmes sont découplés et uniquement soumis aux excitations extérieures). $\mathbf{F}^c$ est le vecteur inconnu des forces de couplage condensées et traduit l'interaction entre les deux sous-systèmes. $\mathbf{F}^c$ est déterminé en inversant le terme $\left(\mathbf{Y}^1 + \mathbf{Y}^2\right)$ dans l'Eq. (133). On injecte ensuite $\mathbf{F}^c$ dans l'Eq. (134) pour obtenir le déplacement $\mathbf{U}$ en un point M_1 du sous-système 1 et en un point M_2 du sous-système 2 :

$$\begin{cases} \mathbf{U}(M_1) = \bar{\mathbf{U}}^1(M_1) + \sum_{i=1}^{N} \mathbf{Y}^1_{M_1 i} \mathbf{F}^c_i \\ \mathbf{U}(M_2) = \bar{\mathbf{U}}^2(M_2) - \sum_{i=1}^{N} \mathbf{Y}^2_{M_2 i} \mathbf{F}^c_i \end{cases} \tag{134}$$

où $\bar{\mathbf{U}}$ désigne le déplacement libre d'un sous-système découplé, et $\mathbf{Y}^1_{M_1 i}$ et $\mathbf{Y}^2_{M_2 i}$ les fonctions de transfert condensées entre un point et une fonction de condensation (c'est-à-dire le rapport entre le déplacement en un point sur une force condensée lorsque le sous-système est découplé). On remarque que le comportement global du système est ainsi totalement déterminé uniquement à partir de grandeurs calculées sur les sous-systèmes découplés.

Cette méthode est validée sur le cas d'une plaque libre excitée ponctuellement. D'un côté, on fait un calcul de référence par la méthode des éléments finis par calcul direct. D'un autre côté, on divise le système en deux plaques de tailles différentes afin d'y appliquer la méthode CTF. Les fonctions de transfert condensées sont calculées pour chaque sous-système découplé par superposition modale avec prise en compte des modes résiduels [85]. Trois différents ensembles de fonctions de condensation sont testés : des fonctions portes (qui consistent à découper la jonction en segments de longueur égale), des fonctions exponentielles et des polynômes de Tchebychev. Une étude numérique permet de mettre en avant plusieurs résultats, et en particulier un critère sur la taille de l'ensemble des fonctions de condensation afin d'avoir une bonne convergence de la méthode. Dans le cas des fonctions portes, qu'on privilégie tout au long de cette étude du fait de leur facilité d'implémentation et du bon conditionnement des matrices,

on observe que les segments doivent être plus petits qu'une demi-longueur d'onde de flexion à la fréquence considérée. La méthode est ensuite validée sur une coque afin de montrer que la jonction n'a pas nécessairement besoin d'être rectiligne. On applique cette approche au cas d'intérêt pour notre étude dans le paragraphe suivant.

E.3 INFLUENCE D'UNE STRUCTURE INTERNE NON-AXISYMÉTRIQUE POUR UNE EXCITATION MÉCANIQUE

La méthode CTF décrite dans le paragraphe précédent permet de coupler des structures minces le long de lignes. La méthode est appliquée afin de calculer la réponse d'une coque raidie immergée axisymétrique avec des structures internes non-axisymétrique. On considère dans un premier temps un excitation mécanique ponctuelle. D'un côté, les structures internes non-axisymétriques sont décrites par FEM, en utilisant la superposition modale avec modes résiduels. D'un autre côté, la coque cylindrique est décrite par la méthode CAA [21]. La CAA est une approche de sous-structuration dédié à l'étude vibro-acoustique de coques cylindriques raidies immergées. L'approche est basée sur l'expression des admittances dans l'espace des ordres circonférentiels. Elle permet de coupler un modèle de coque cylindrique immergée décrit par les équations de Flügge avec des modèles éléments finis de structures internes axisymétriques. La CAA peut être vue comme un cas particulier de la méthode CTF où les grandeurs sont projetées sur les ordres circonférentiels (fonctions de condensation exponentielles). La méthode est cependant basée sur l'hypothèse d'un système axisymétrique dans un domaine fluide infini, permettant de calculer chaque ordre circonférentiel séparémment.

Pour coupler la CAA avec un modèle FEM, on utilise les fonctions portes pour calculer les fonctions de transfert condensées nécessaires à la méthode CTF. La coque raidie immergée étant axisymétrique, on considère que les couplages entre les sous-systèmes se font le long de la circonférence (c'est-à-dire que seule la coordonnée θ évolue le long de la jonction dans le repère cylindrique associé). Ainsi, en utilisant l'invariance par rotation, des simplifications peuvent être faites dans le calcul des fonctions de transfert condensées du système axisymétrique. On montre ainsi qu'il suffit d'exciter le système axisymétrique en un point sur la jonction pour être capable de calculer les fonctions

de transfert condensées sur toute la jonction. L'inclusion d'une structure interne non-axisymétrique n'alourdit donc pas les calculs de manière drastique.

La méthode CTF est ainsi appliquée sur une coque raidie cylindrique couplée à une structure interne non-axisymétrique. On commence par le cas d'une coque de 4 m de long *in vacuo*, afin de pouvoir valider les résultats par rapport à une référence calculée par la méthode FEM. Ensuite, le cas plus réaliste d'une coque cylindrique immergée de 42,3 m de long est considéré. On y ajoute consécutivement différentes structures (plaques incurvées, plancher) et on s'intéresse à l'influence des non-axisymétries sur le comportement vibro-acoustique du système. Si on s'intéresse aux vibrations de la coque dans l'espace des nombres d'onde, on se rend compte qu'un plus grand nombre d'ordres circonférentiels interviennent dans la réponse du système avec la structure interne non-axisymétrique par rapport au cas sans la structure non-axisymétrique. Or, on sait que dans le cas d'une plaque, les nombres d'onde de flexion inférieurs au nombre d'onde acoustique sont les principaux contributeurs à la pression rayonnée en champ lointain. Ainsi, on montre qu'au-dessus de la fréquence d'anneau, l'efficacité de rayonnement d'une coque cylindrique a tendance à augmenter lorsqu'on y ajoute une structure interne non-axisymétrique. D'autre part, on observe une modification des cartographies de vibration sur la coque, liée au fait que des vibrations peuvent se propager le long des structures internes.

E.4 CAMPAGNE EXPÉRIMENTALE

Afin de vérifier les tendances observées sur les simulations numériques, une campagne expérimentale est menée. On cherche à mesurer l'influence d'une structure interne non-axisymétrique sur une maquette de cylindre raidi. Les mesures sont réalisées en air, dans une chambre semi-anéchoïque. Les manipulations n'ont pas été réalisées en eau pour des raisons de coûts et de délais, mais on a observé sur des simulations qu'une augmentation de l'efficacité de rayonnement peut avoir lieu quelque soit le fluide environnant. On dispose d'une coque cylindrique de 1,5 m de long, de 0,1 m de rayon et de 1,5 mm d'épaisseur, raidi non-périodiquement, et également d'un plancher d'une longueur d'environ 0,9 m et de 1,5 mm d'épaisseur que l'on colle à l'intérieur du cylindre. Le dispositif expérimental consiste à suspendre le système à une potence équipée d'un

plateau tournant. Le cylindre est excité par un pot vibrant sur lequel est connecté une tête d'impédance qui mesure la force et l'accélération au point d'excitation. On place à une position fixe un vibromètre laser à balayage. L'expérience consiste à faire pivoter le système sur lui-même afin de balayer toutes les génératrices du cylindre et d'y mesurer les déplacements radiaux. On extrait ainsi des cartographies de déplacement sur toute la surface extérieure du cylindre et on peut en déduire la vitesse quadratique moyenne. Une transformée de Fourier spatiale 2D permet d'étudier la réponse dans l'espace des nombres d'onde et d'observer le couplage des ordres circonférentiels. Le théorème de la phase stationnaire est utilisé afin de calculer la pression et la puissance rayonnée en champ lointain à partir des déplacements dans l'espace des nombres d'onde. Les mesures sont réalisées dans le cas axisymétrique et non-axisymétrique, c'est-à-dire sans et avec structure interne. On observe bien les phénomènes mis en avant par l'étude numérique du paragraphe précédent : les cartographies de déplacement sont modifiées, un plus grand nombre d'ordres circonférentiels interviennent dans la réponse et l'efficacité de rayonnement augmente. Un effet d'amortissement est également observé, du fait de la forte densité modale de la structure interne et de l'adaptation d'impédance entre les deux sous-systèmes. Des courbes de dispersion opérationnelles sont également tracées pour voir si la structure interne a une influence sur la propagation des ondes sur la coque cylindrique.

E.5 DIFFRACTION D'UNE COQUE RAIDIE COUPLÉE À DES STRUCTURES INTERNES NON-AXISYMÉTRIQUES

La méthode CTF est ensuite appliquée au cas d'un système excité par une onde plane acoustique. Le principe de la méthode et du calcul des fonctions de transfert condensées reste inchangé. La différence réside dans l'expression du déplacement libre de la coque axisymétrique, qui est calculé à partir de la CAA dans le cas d'une excitation acoustique [150]. Dans ce cas, les équations de Flügge sont modifiées afin de prendre en compte un terme de pression bloquée au second membre.

On s'intéresse à un cas test proposé par Liétard *et al.* [48] constitué d'une coque cylindrique de 75 cm de long et 10 cm de diamètre, immergée et régulièrement raidie, et dont les spectres angle-fréquence de la pression rétrodiffusé sont obtenus expérimen-

talement. Trois principaux phénomènes sont observés : la propagation d'ondes hélicoïdales le long de la coque, la diffraction de Bragg due aux réflexions géométriques sur les raidisseurs et la diffraction de Bloch-Floquet due à l'interaction des ondes de flexion dans le coque avec les raidisseurs. On utilise la méthode CTF pour observer l'influence de structures internes non-axisymétriques sur ces phénomènes. Ces structures internes sont composées de plaques incurvées couvrant environ un quart de la circonférence et reliant deux raidisseurs adjacents, sur toute la longueur de la coque. On remarque que la propagation des ondes hélicoïdales et la diffraction de Bragg sont très peu impactées par les structures internes. Par contre, de nouvelles trajectoires apparentées à des phénomènes de diffraction de Bloch-Floquet sont observées. Un modèle de diffraction simplifié est développé et permet d'expliquer que les trajectoires supplémentaires observées sont liées à la propagation des ondes dans les structures internes.

E.6 MODÉLISATION D'UN SYSTÈME COMPLEXE SOUMIS À DES EXCITATIONS ALÉATOIRES

Une structure peut être soumise à un champ de pression aléatoire, tel qu'un champ acoustique diffus ou une couche limite turbulente. En particulier pour cette dernière, de nombreux auteurs se sont intéressés à la réponse d'une plaque, en la couplant éventuellement à un fluide lourd ou à des raidisseurs. Cependant, très peu d'éléments sont disponibles dans la littérature dans le cas de coques cylindriques. C'est pourquoi on propose ici d'utiliser le principe de réciprocité (k, M) [84] en conjonction avec la méthode CTF afin d'évaluer les moments du second ordre des grandeurs vibro-acoustiques d'une structure excitée sur une surface Σ_p. On utilise la formulation en nombre d'onde-fréquence, où la densité spectrale de puissance du déplacement d'un point $\mathbf{x}$ du système peut être écrite :

$$S_{WW}(\mathbf{x}, f) = \frac{1}{4\pi^2} \iint_{-\infty}^{+\infty} |\tilde{\tilde{H}}_W(\mathbf{x}, \mathbf{k}, f)|^2 \phi_{pp}(\mathbf{k}, f) \mathrm{d}^2\mathbf{k} \tag{135}$$

Dans l'Eq. (135), le terme $\phi_{pp}(\mathbf{k}, f)$ est l'interspectre de la pression pariétale et représente l'excitation aléatoire. Pour une couche limite turbulente, le rayon de courbure de la coque cylindrique étant grand par rapport à l'épaisseur de la couche limite, on peut utiliser des modèles développés dans le cas de plaques et très largement rensei-

gnés dans la littérature. $\tilde{\tilde{H}}_W(\mathbf{x}, \mathbf{k}, f)$ est appelé fonction de sensibilité et représente la réponse de la structure. Elle peut être vue comme la transformée de Fourier dans l'espace d'une fonction de transfert :

$$\tilde{\tilde{H}}_W(\mathbf{x}, \mathbf{k}, f) = \frac{1}{(2\pi)^2} \int_{\Sigma_p} H_W(\mathbf{x}, \check{\mathbf{x}}, f)\, e^{-\mathrm{j}\mathbf{k}\check{\mathbf{x}}} \mathrm{d}\check{\mathbf{x}} \tag{136}$$

On remarque qu'une intégration selon les nombres d'onde $\mathbf{k}$ est effectuée dans l'Eq. (135). Cependant, il est difficile et très coûteux en pratique de calculer les fonctions de sensibilité telles que définies dans l'Eq. (136) pour une multitude de valeurs de $\mathbf{k}$. C'est pourquoi on utilise le principe de réciprocité en vibro-acoustique, qui indique qu'une fonction de transfert reste inchangée si on échange le point d'excitation et le point d'observation. Ainsi la fonction de sensibilité de l'Eq. (136) peut également être définie comme suit :

$$\tilde{\tilde{H}}_W(\mathbf{x}, \mathbf{k}, f) = \frac{1}{(2\pi)^2} \int_{\Sigma_p} H_W(\check{\mathbf{x}}, \mathbf{x}, f)\, e^{-\mathrm{j}\mathbf{k}\check{\mathbf{x}}} \mathrm{d}\check{\mathbf{x}} \tag{137}$$

De ce point de vue, la fonction de sensibilité est la réponse spectrale du système sur la surface Σ_p en réponse à une excitation au point $\mathbf{x}$. En pratique, il est plus commode d'estimer cette fonction de sensibilité réciproque et l'Eq. (135) peut donc être facilement calculée. La même procédure peut être utilisée pour calculer la densité spectrale de puissance de pression à un point $\mathbf{z}$:

$$S_{pp}(\mathbf{z}, f) = \frac{1}{4\pi^2} \iint_{-\infty}^{+\infty} |\tilde{\tilde{H}}_p(\mathbf{z}, \mathbf{k}, f)|^2 \phi_{pp}(\mathbf{k}, f) \mathrm{d}^2\mathbf{k} \tag{138}$$

où $\tilde{\tilde{H}}_p(\mathbf{z}, \mathbf{k}, f)$ est une fonction de sensibilité qui, en vertu du principe de réciprocité, peut être vue comme la réponse spectrale des déplacements sur la surface Σ_p en réponse à une excitation monopolaire au point $\mathbf{z}$.

On utilise la méthode CTF pour calculer les fonctions de sensibilité d'une coque cylindrique raidie immergée couplée à une structure interne non-axisymétrique. Pour calculer les densités spectrales de puissance du déplacement en un point, on a besoin de la réponse dans l'espace des nombres d'onde lorsque le système est soumis à une force ponctuelle en ce point. Aucun développement supplémentaire n'est donc nécessaire par rapport aux cas sous excitation mécanique présentés précédemment. Pour calculer les densités spectrales de puissance en pression, on a besoin de la réponse dans l'espace des nombres d'onde lorsque le système est soumis à une excitation acoustique

monopolaire. La méthode CTF permet de prendre en compte l'excitation monopolaire au travers du déplacement libre de la coque cylindrique immergée découplée des structures internes. Pour ce sous-système, l'excitation intervient par un terme de pression bloquée au second membre des équations de Flügge. La pression bloquée sur la surface d'un cylindre infini est calculée à partir de l'équation de Helmholtz cylindrique et des conditions aux limites infiniment rigides sur la surface.

Le couplage du principe de réciprocité et de la méthode CTF donne donc un outil puissant et flexible, permettant l'étude de systèmes complexes soumis à une excitation aléatoire. Un cas test d'une coque raidie immergée couplée à un plancher permet d'évaluer l'influence de la structure interne sur le déplacement en un point de la coque et sur la pression en un point du domaine acoustique, pour deux excitations différentes : un champ acoustique diffus dans une portion du cylindre entre deux cloisons et une couche limite turbulente modélisée par le produit de l'autospectre de Goody et l'interspectre de Corcos. On remarque que dans les deux cas, une influence du plancher peut être vue sur les densités spectrales de puissance. Pour les déplacements, la densité spectrale de puissance peut augmenter jusqu'à 6 dB pour certaines fréquences. Cette augmentation peut être expliquée en regardant les fonctions de sensibilité, où on se rend compte qu'un plus grand nombre d'ordres circonférentiels ont une forte contribution dans le cas non-axisymétrique. Pour la densité spectrale de puissance de la pression cependant, l'influence du plancher est plus faible, avec une augmentation n'atteignant pas plus de 2 dB. Dans ce cas, le point d'observation est très éloigné de la structure (500 m) et on peut donc dire que la non-axisymétrie a plutôt un effet local.

E.7 CONCLUSIONS ET PERSPECTIVES

Une nouvelle méthode de sous-structuration a été développée dans ces travaux afin de coupler des structures mécaniques minces le long d'une ligne. Elle présente l'avantage de pouvoir coupler des sous-systèmes décrits par différentes approches, en ne connaissant uniquement les admittances des sous-systèmes découplés sur la ligne de couplage. La méthode est appliquée en particulier à des coques cylindriques raidies immergées couplées à des structures internes non-axisymétriques. Dans ce cas on couple un modèle de coque raidie immergée axisymétrique décrit par CAA avec des structures

internes non-axisymétriques décrites par FEM. Des cas tests ont été présentés, et des résultats jusque dans les moyennes fréquences ($k_0 R \simeq 40$) ont pu être présentés, tout en gardant des coûts de calculs raisonnables. On a d'ailleurs pu illustrer la flexibilité de la méthode en choisissant successivement plusieurs géométries pour les structures internes. Une des perspectives de ces travaux est d'implémenter la méthode de sous-structuration dans un outil informatique afin de pouvoir être facilement utilisée dans le processus de conception d'un produit industriel. Plusieurs géométries de structures internes pourraient alors être testées et leur influence sur les exigences en termes de bruit et vibrations pourrait être examinée. Justement, un autre avantage de cette méthode est que la réanalyse est facile, dans la mesure où des résultats intermédiaires peuvent être stockés, et qu'on peut conserver une base de données pour certains sous-systèmes que l'on souhaite réutiliser.

L'une des perspectives à court terme est d'utiliser l'outil développé pour le calcul de la réponse d'une coque cylindrique à une excitation aléatoire afin de comprendre l'influence de la complexité structurelle. Ainsi, on commencera par examiner l'effet de raidisseurs périodiques afin de voir si on peut observer des phénomènes similaires à ceux observés sur les plaques raidies. Une autre perspective pourrait être d'étendre le formalisme de la méthode à des couplages surfaciques, en considérant des fonctions de condensation à deux variables. Des systèmes comportant des matériaux absorbants ou de masquage pourraient alors être abordés.

PUBLICATIONS ARISING FROM THE THESIS

- **Articles in international peer-reviewed journals**
  - [172] V. Meyer, L. Maxit, J.-L. Guyader, T. Leissing and C. Audoly. A condensed transfer function method as a tool for solving vibroacoustic problems. *Proc IMechE Part C: J Mechanical Engineering Science*, 230(6):928–938, 2016.
  - [173] V. Meyer, L. Maxit, J.-L. Guyader and T. Leissing. Prediction of the vibroacoustic behavior of a submerged shell with non-axisymmetric internal substructures by a condensed transfer function method. *Journal of Sound and Vibration*, 360:260–276, 2016.
  - [201] V. Meyer, L. Maxit and C. Audoly. A substructuring method for modeling the acoustic scattering from stiffened submerged shells coupled to non-axisymmetric internal structures. *Journal of the Acoustical Society of America*, 140(3):1609–1617, 2016.
- **Proceedings of international conferences**
  - [202] V. Meyer, L. Maxit, J.-L. Guyader, T. Leissing and C. Audoly. A condensed transfer function method as a tool for solving vibroacoustic problems. NOVEM 2015, Dubrovnik, Croatia, 2015.
  - [193] V. Meyer, L. Maxit, J.-L. Guyader, T. Leissing and C. Audoly. Scattering of a periodically stiffened submerged shell coupled to non-axisymmetric internal frames. 22nd International Congress on Sound and Vibration, Florence, Italy, 2015.
  - [203] L. Maxit and V. Meyer. Condensed Transfer Function (CTF) method as a tool for substructuring vibro-acoustic problem. Inter-noise, San Francisco, CA, USA, 2015.
  - [195] V. Meyer, L. Maxit, Y. Renou and C. Audoly. Vibroacoustic modeling of submerged stiffened cylindrical shells with internal structures under random excitations. Inter-noise, Hamburg, Germany, 2016.

- **Proceedings of national conferences**
  - [179] V. Meyer, L. Maxit, J.-L. Guyader, C. Audoly and Y. Renou. Vibrations et rayonnement acoustique des coques cylindriques raidies : Étude expérimentale de l'influence des structures internes non-axisymétriques. Congrès Français d'Acoustique, Le Mans, France, 2016.

BIBLIOGRAPHY

[1] R. J. Urick. *Principles of underwater sound for engineers*. Tata McGraw-Hill Education, 1967.

[2] A. W. Leissa. *Vibration of shells*, volume 288. Scientific and Technical Information Office, National Aeronautics and Space Administration Washington, DC, USA, 1973.

[3] W. Flügge. *Statik und dynamik der schalen*. Springer, 1962.

[4] D. G. Karczub. Expressions for direct evaluation of wave number in cylindrical shell vibration studies using the flügge equations of motion. *The Journal of the Acoustical Society of America*, 119(6):3553–3557, 2006.

[5] R. Ruotolo. A comparison of some thin shell theories used for the dynamic analysis of stiffened cylinders. *Journal of Sound and Vibration*, 243(5):847–860, 2001.

[6] H.W. Lee and M. K. Kwak. Free vibration analysis of a circular cylindrical shell using the rayleigh–ritz method and comparison of different shell theories. *Journal of Sound and Vibration*, 353:344–377, 2015.

[7] L. Maxit. Modelling of a non-periodically stiffened shell immerged in water by the circumferential admittance approach: comparison of different methods to estimate the shell admittances. NOVEM 2009, Oxford, United Kingdom, 2009.

[8] M. C. Junger and D. Feit. *Sound, structures, and their interaction*, volume 240. MIT press Cambridge, MA, 1972.

[9] J. E. Manning and G. Maidanik. Radiation properties of cylindrical shells. *The Journal of the Acoustical Society of America*, 36(9):1691–1698, 1964.

[10] A. Harari. Dynamic characteristics of cylindrical shells at the neighborhood of the ring frequency. *The Journal of the Acoustical Society of America*, 76(3):968–972, 1984.

[11] M. Heckl. Vibrations of point-driven cylindrical shells. *The Journal of the Acoustical Society of America*, 34(10):1553–1557, 1962.

[12] C. E. Wallace. Radiation resistance of a rectangular panel. *The Journal of the Acoustical Society of America*, 51(3):946–952, 1972.

[13] M. S. Qatu. Recent research advances in the dynamic behavior of shells: 1989–2000, part 2: homogeneous shells. *Applied Mechanics Reviews*, 55(5):415–434, 2002.

[14] G. Galletly. On the in-vacuo vibrations of simply supported, ring-stiffened cylindrical shells. *Proceedings of the United States National Congress of Applied Mechanics*, 2:225–231, 1954.

[15] R. N. Arnold and G. B. Warburton. Flexural vibrations of the walls of thin cylindrical shells having freely supported ends. *Proceedings of the Royal Society of London. Series A. Mathematical and Physical Sciences*, 197(1049):238–256, 1949.

[16] W. H. Hoppmann II. Some characteristics of the flexural vibrations of orthogonally stiffened cylindrical shells. *The Journal of the Acoustical Society of America*, 30(1):77–82, 1958.

[17] T. Wah and W. C. L. Hu. Vibration analysis of stiffened cylinders including interring motion. *The Journal of the Acoustical Society of America*, 43(5):1005–1016, 1968.

[18] D. E. Beskos and J. B. Oates. Dynamic analysis of ring-stiffened circular cylindrical shells. *Journal of Sound and Vibration*, 75(1):1–15, 1981.

[19] A. M. J. Al-Najafi and G. B. Warburton. Free vibration of ring-stiffened cylindrical shells. *Journal of Sound and Vibration*, 13(1):9–25, 1970.

[20] J.-F. Imbert. *Analyse des structures par éléments finis*. 1979.

[21] L. Maxit and J.-M. Ginoux. Prediction of the vibro-acoustic behavior of a submerged shell non periodically stiffened by internal frames. *The Journal of the Acoustical Society of America*, 128(1):137–151, 2010.

[22] D. M. Photiadis. The propagation of axisymmetric waves on a fluid-loaded cylindrical shell. *The Journal of the Acoustical Society of America*, 88(1):239–250, 1990.

[23] C. B. Burroughs. Acoustic radiation from fluid-loaded infinite circular cylinders with doubly periodic ring supports. *The Journal of the Acoustical Society of America*, 75(3):715–722, 1984.

[24] C. B. Burroughs and J. E. Hallander. Acoustic radiation from fluid-loaded, ribbed cylindrical shells excited by different types of concentrated mechanical drives. *The Journal of the Acoustical Society of America*, 91(5):2721–2739, 1992.

[25] A. Harari and B. E. Sandman. Radiation and vibrational properties of submerged stiffened cylindrical shells. *The Journal of the Acoustical Society of America*, 88(4):1817–1830, 1990.

[26] B. E. Sandman. Fluid-loading influence coefficients for a finite cylindrical shell. *The Journal of the Acoustical Society of America*, 60(6):1256–1264, 1976.

[27] B. Laulagnet and J.-L. Guyader. Modal analysis of a shell's acoustic radiation in light and heavy fluids. *Journal of Sound and Vibration*, 131(3):397–415, 1989.

[28] B. Laulagnet and J.-L. Guyader. Sound radiation by finite cylindrical ring stiffened shells. *Journal of Sound and Vibration*, 138(2):173–191, 1990.

[29] J. E. Cole III. Vibrations of a framed cylindrical shell submerged in and filled with acoustic fluids: spectral solution. *Computers & structures*, 65(3):385–393, 1997.

[30] J. Yan, T. Y. Li, T. G. Liu, and J. X. Liu. Characteristics of the vibrational power flow propagation in a submerged periodic ring-stiffened cylindrical shell. *Applied acoustics*, 67(6):550–569, 2006.

[31] M. Caresta and N. J. Kessissoglou. Structural and acoustic responses of a fluid-loaded cylindrical hull with structural discontinuities. *Applied Acoustics*, 70(7):954–963, 2009.

[32] M. Caresta and N. J. Kessissoglou. Free vibrational characteristics of isotropic coupled cylindrical–conical shells. *Journal of Sound and Vibration*, 329(6):733–751, 2010.

[33] M. Caresta and N. J. Kessissoglou. Acoustic signature of a submarine hull under harmonic excitation. *Applied acoustics*, 71(1):17–31, 2010.

[34] M. Caresta and N. J. Kessissoglou. Reduction of the sound pressure radiated by a submarine by isolation of the end caps. *Journal of Vibration and Acoustics*, 133(3):031008, 2011.

[35] Y. Qu, H. Hua, and G. Meng. Vibro-acoustic analysis of coupled spherical–cylindrical–spherical shells stiffened by ring and stringer reinforcements. *Journal of Sound and Vibration*, 355:345–359, 2015.

[36] S. Merz, R. Kinns, and N. Kessissoglou. Structural and acoustic responses of a submarine hull due to propeller forces. *Journal of Sound and Vibration*, 325(1):266–286, 2009.

[37] S. Merz, N. J. Kessissoglou, R. Kinns, and S. Marburg. Minimisation of the sound power radiated by a submarine through optimisation of its resonance changer. *Journal of Sound and Vibration*, 329(8):980–993, 2010.

[38] H. Peters, N. J. Kessissoglou, and S. Marburg. Modal decomposition of exterior acoustic-structure interaction problems with model order reduction. *The Journal of the Acoustical Society of America*, 135(5):2706–2717, 2014.

[39] Q. Zhou and P. F. Joseph. A numerical method for the calculation of dynamic response and acoustic radiation from an underwater structure. *Journal of Sound and Vibration*, 283(3):853–873, 2005.

[40] M. Zampolli, A. Tesei, F. B. Jensen, N. Malm, and J. B. Blottman III. A computationally efficient finite element model with perfectly matched layers applied to scattering from axially symmetric objects. *The Journal of the Acoustical Society of America*, 122(3):1472–1485, 2007.

[41] J.-P. Berenger. A perfectly matched layer for the absorption of electromagnetic waves. *Journal of Computational Physics*, 114:185–200, 1994.

[42] L. Flax, V. K. Varadan, and V. V. Varadan. Scattering of an obliquely incident acoustic wave by an infinite cylinder. *The Journal of the Acoustical Society of America*, 68(6):1832–1835, 1980.

[43] F. Léon, F. Lecroq, D. Décultot, and G. Maze. Scattering of an obliquely incident acoustic wave by an infinite hollow cylindrical shell. *The Journal of the Acoustical Society of America*, 91(3):1388–1397, 1992.

[44] M. L. Rumerman. Contribution of membrane wave reradiation to scattering from finite cylindrical steel shells in water. *The Journal of the Acoustical Society of America*, 93(1):55–65, 1993.

[45] S. F. Morse, P. L. Marston, and G. Kaduchak. High-frequency backscattering enhancements by thick finite cylindrical shells in water at oblique incidence: Experiments, interpretation, and calculations. *The Journal of the Acoustical Society of America*, 103(2):785–794, 1998.

[46] D. M. Photiadis, J. A. Bucaro, and B. H. Houston. Scattering from flexural waves on a ribbed cylindrical shell. *The Journal of the Acoustical Society of America*, 96(5):2785–2790, 1994.

[47] B. H. Houston, J. A. Bucaro, and D. M. Photiadis. Broadband acoustic scattering from a ribbed shell. *The Journal of the Acoustical Society of America*, 98(5):2851–2853, 1995.

[48] R. Liétard, D. Décultot, G. Maze, and M. Tran-Van-Nhieu. Acoustic scattering from a finite cylindrical shell with evenly spaced stiffeners: Experimental investigation. *The Journal of the Acoustical Society of America*, 118(4):2142–2146, 2005.

[49] M. Tran-Van-Nhieu. Scattering from a ribbed finite cylindrical shell. *The Journal of the Acoustical Society of America*, 110(6):2858–2866, 2001.

[50] Y. P. Guo. Sound scattering from cylindrical shells with internal elastic plates. *The Journal of the Acoustical Society of America*, 93(4):1936–1946, 1993.

[51] A. Klauson and J. Metsaveer. Sound scattering by a cylindrical shell reinforced by lengthwise ribs and walls. *The Journal of the Acoustical Society of America*, 91(4):1834–1843, 1992.

[52] A. G. Pathak and P. R. Stepanishen. Acoustic harmonic radiation from fluid-loaded infinite cylindrical elastic shells using elasticity theory. *The Journal of the Acoustical Society of America*, 96(1):573–582, 1994.

[53] A. Baillard, J.-M. Conoir, D. Décultot, G. Maze, A. Klauson, and J. Metsaveer. Acoustic scattering from fluid-loaded stiffened cylindrical shell: Analysis using elasticity theory. *The Journal of the Acoustical Society of America*, 107(6):3208–3216, 2000.

[54] Y. P. Guo. Sound scattering by bulkheads in cylindrical shells. *The Journal of the Acoustical Society of America*, 95(5):2550–2559, 1994.

[55] J. M. Cuschieri and D. Feit. Acoustic scattering from a fluid-loaded cylindrical shell with discontinuities: Single plate bulkhead. *The Journal of the Acoustical Society of America*, 98(1):320–338, 1995.

[56] J. M. Cuschieri and D. Feit. Acoustic scattering from a fluid-loaded cylindrical shell with discontinuities: Double plate bulkhead. *The Journal of the Acoustical Society of America*, 98(1):339–352, 1995.

[57] S. Park. *Sound wave scattering by cylindrical shells with internal structures*. PhD thesis, Massachusetts Institute of Technology, 1995.

[58] A. Pan, J. Fan, and B. Wang. Acoustic scattering from a double periodically bulkheaded and ribbed finite cylindrical shell. *The Journal of the Acoustical Society of America*, 134(5):3452–3463, 2013.

[59] D. M. Photiadis and B. H. Houston. Anderson localization of vibration on a framed cylindrical shell. *The Journal of the Acoustical Society of America*, 106(3):1377–1391, 1999.

[60] M. H. Marcus, B. H. Houston, and D. M. Photiadis. Wave localization on a submerged cylindrical shell with rib aperiodicity. *The Journal of the Acoustical Society of America*, 109(3):865–869, 2001.

[61] D. M. Photiadis, J. A. Bucaro, and B. H. Houston. The effect of internal oscillators on the acoustic response of a submerged shell. *The Journal of the Acoustical Society of America*, 101(2):895–899, 1997.

[62] M. Tran-Van-Nhieu. Scattering from a ribbed finite cylindrical shell with internal axisymmetric oscillators. *The Journal of the Acoustical Society of America*, 112(2):402–410, 2002.

[63] C. Soize. Probabilistic structural modeling in linear dynamic analysis of complex mechanical systems, I-theoretical elements. *La Recherche Aérospatiale (English edition)*, 5:Pages–23, 1986.

[64] A. D. Pierce. Resonant-frequency-distribution of internal mass inferred from mechanical impedance matrices, with application to fuzzy structure theory. *Journal of vibration and acoustics*, 119(3):324–333, 1997.

[65] W. K. Blake. Aero-hydroacoustics for ships. vol I. Technical report, DTNSRDC-84/010, David W. Taylor Naval Ship Research and Development Centre, Bethesda, 1984.

[66] W. K. Blake. Aero-hydroacoustics for ships, vol. II. Technical report, DTNSRDC-84/010, David W. Taylor Naval Ship Research and Development Centre, Bethesda, 1984.

[67] M. Aucejo. *Vibro-acoustique des structures immergées sous écoulement turbulent*. PhD thesis, INSA de Lyon, 2010.

[68] W. A. Strawderman and R. S. Brand. Turbulent-flow-excited vibration of a simply supported, rectangular flat plate. *The Journal of the Acoustical Society of America*, 45(1):177–192, 1969.

[69] W. W. Willmarth and C. S. Yang. Wall-pressure fluctuations beneath turbulent boundary layers on a flat plate and a cylinder. *Journal of Fluid Mechanics*, 41(01):47–80, 1970.

[70] W. W. Willmarth, R. E. Winkel, L. K. Sharma, and T. J. Bogar. Axially symmetric turbulent boundary layers on cylinders: mean velocity profiles and wall pressure fluctuations. *Journal of Fluid Mechanics*, 76(01):35–64, 1976.

[71] R. M. Lueptow. Turbulent boundary layer on a cylinder in axial flow. Technical report, DTIC Document, 1988.

[72] G. M. Corcos. Resolution of pressure in turbulence. *The Journal of the Acoustical Society of America*, 35(2):192–199, 1963.

[73] D. M. Chase. The character of the turbulent wall pressure spectrum at subconvective wavenumbers and a suggested comprehensive model. *Journal of Sound and Vibration*, 112(1):125–147, 1987.

[74] W. K. Blake and R. V. Waterhouse. The use of cross-spectral density measurements in partially reverberant sound fields. *Journal of Sound and Vibration*, 54(4):589–599, 1977.

[75] H. Nélisse and J. Nicolas. Characterization of a diffuse field in a reverberant room. *The Journal of the Acoustical Society of America*, 101(6):3517–3524, 1997.

[76] B. Arguillat, D. Ricot, C. Bailly, and G. Robert. Measured wavenumber: Frequency spectrum associated with acoustic and aerodynamic wall pressure fluctuations. *The Journal of the Acoustical Society of America*, 128(4):1647–1655, 2010.

[77] W. A. Strawderman. Turbulence-induced plate vibrations: an evaluation of finite-and infinite-plate models. *The Journal of the Acoustical Society of America*, 46(5B):1294–1307, 1969.

[78] F. Birgersson, N. S. Ferguson, and S. Finnveden. Application of the spectral finite element method to turbulent boundary layer induced vibration of plates. *Journal of Sound and Vibration*, 259(4):873–891, 2003.

[79] W. A. Strawderman and R. A. Christman. Turbulence-induced plate vibrations: Some effects of fluid loading on finite and infinite plates. *The Journal of the Acoustical Society of America*, 52(5B):1537–1552, 1972.

[80] M. L. Rumerman. Estimation of broadband acoustic power radiated from a turbulent boundary layer-driven reinforced finite plate section due to rib and boundary forces. *The Journal of the Acoustical Society of America*, 111(3):1274–1279, 2002.

[81] W. A. Strawderman. Wavevector-frequency analysis with applications to acoustics. Technical report, DTIC Document, 1994.

[82] C. Maury, P. Gardonio, and S. J. Elliott. A wavenumber approach to modelling the response of a randomly excited panel, part I: general theory. *Journal of Sound and Vibration*, 252(1):83–113, 2002.

[83] C. Maury, P. Gardonio, and S. J. Elliott. A wavenumber approach to modelling the response of a randomly excited panel, part II: Application to aircraft panels excited by a turbulent boundary layer. *Journal of Sound and Vibration*, 252(1):115–139, 2002.

[84] L. Maxit and V. Denis. Prediction of flow induced sound and vibration of periodically stiffened plates. *The Journal of the Acoustical Society of America*, 133(1):146–160, 2013.

[85] S. Rubin. Improved component-mode representation for structural dynamic analysis. *AIAA Journal*, 13(8):995–1006, 1975.

[86] E. Balmes. Modes and regular shapes. how to extend component mode synthesis theory. XI DINAME, Ouro Preto, MG, Brazil, 2005.

[87] N. Roy and M. Lapi. Efficient computation of the radiated sound power of vibrating structures using a modal approach. Acoustics'08, Paris, France, 2008.

[88] W. C. Hurty. Dynamic analysis of structural systems using component modes. *AIAA journal*, 3(4):678–685, 1965.

[89] W. C. Hurty, J. D. Collins, and G. C. Hart. Dynamic analysis of large structures by modal synthesis techniques. *Computers & Structures*, 1(4):535–563, 1971.

[90] M. C. C. Bampton and R. R. Craig Jr. Coupling of substructures for dynamic analyses. *AIAA Journal*, 6(7):1313–1319, 1968.

[91] G. M. L. Gladwell. Branch mode analysis of vibrating systems. *Journal of Sound and Vibration*, 1(1):41–59, 1964.

[92] W. A. Benfield and R. F. Hruda. Vibration analysis of structures by component mode substitution. *AIAA Journal*, 9(7):1255–1261, 1971.

[93] R. L. Goldman. Vibration analysis by dynamic partitioning. *AIAA journal*, 7(6):1152–1154, 1969.

[94] S. N. Hou. Review of modal synthesis techniques and a new approach. *Shock and vibration bulletin*, 40(4):25–39, 1969.

[95] W.-H. Shyu, Z.-D. Ma, and G. M. Hulbert. A new component mode synthesis method: quasi-static mode compensation. *Finite elements in Analysis and Design*, 24(4):271–281, 1997.

[96] M. A. Tournour, N. Atalla, O. Chiello, and F. Sgard. Validation, performance, convergence and application of free interface component mode synthesis. *Computers & Structures*, 79(20):1861–1876, 2001.

[97] D. J. Rixen. A dual craig–bampton method for dynamic substructuring. *Journal of Computational and applied mathematics*, 168(1):383–391, 2004.

[98] R. H. MacNeal. A hybrid method of component mode synthesis. *Computers & Structures*, 1(4):581–601, 1971.

[99] A. L. Hale and L. Meirovitch. A general substructure synthesis method for the dynamic simulation of complex structures. *Journal of Sound and Vibration*, 69(2):309–326, 1980.

[100] A. L. Hale and L. Meirovitch. A general procedure for improving substructures representation in dynamic synthesis. *Journal of Sound and vibration*, 84(2):269–287, 1982.

[101] F. J. Fahy. Statistical energy analysis: a wolf in sheep's clothing? In *Internoise*, volume 1, pages 13–13. Noise Control Foundation, 1993.

[102] E. Rebillard and J.-L. Guyader. Vibrational behaviour of a population of coupled plates: hypersensitivity to the connexion angle. *Journal of Sound and Vibration*, 188(3):435–454, 1995.

[103] R. H. Lyon and G. Maidanik. Power flow between linearly coupled oscillators. *The Journal of the Acoustical Society of America*, 34(5):623–639, 1962.

[104] R. S. Langley. A general derivation of the statistical energy analysis equations for coupled dynamic systems. *Journal of Sound and Vibration*, 135(3):499–508, 1989.

[105] F. J. Fahy. Statistical energy analysis: a critical overview. *Philosophical Transactions of the Royal Society of London A: Mathematical, Physical and Engineering Sciences*, 346(1681):431–447, 1994.

[106] A. Le Bot and V. Cotoni. Validity diagrams of statistical energy analysis. *Journal of sound and vibration*, 329(2):221–235, 2010.

[107] L. Maxit. *Reformulation and extension of SEA model by taking the modal energy distribution into account (in French)*. PhD thesis, INSA Lyon, 2000.

[108] L. Maxit and J.-L. Guyader. Estimation of SEA coupling loss factors using a dual formulation and FEM modal information, part I: theory. *Journal of sound and vibration*, 239(5):907–930, 2001.

[109] L. Maxit and J.-L. Guyader. Estimation of SEA coupling loss factors using a dual formulation and FEM modal information, part II: Numerical applications. *Journal of sound and vibration*, 239(5):931–948, 2001.

[110] L. Maxit and J.-L. Guyader. Extension of SEA model to subsystems with non-uniform modal energy distribution. *Journal of sound and vibration*, 265(2):337–358, 2003.

[111] R. S. Langley and P. Bremner. A hybrid method for the vibration analysis of complex structural-acoustic systems. *The Journal of the Acoustical Society of America*, 105(3):1657–1671, 1999.

[112] P. J. Shorter and R. S. Langley. Vibro-acoustic analysis of complex systems. *Journal of Sound and Vibration*, 288(3):669–699, 2005.

[113] V. Cotoni, P. J. Shorter, and R. S. Langley. Numerical and experimental validation of a hybrid finite element-statistical energy analysis method. *The Journal of the Acoustical Society of America*, 122(1):259–270, 2007.

[114] V. Cotoni, R. S. Langley, and P. J. Shorter. A statistical energy analysis subsystem formulation using finite element and periodic structure theory. *Journal of Sound and Vibration*, 318(4):1077–1108, 2008.

[115] R. S. Langley and J. A. Cordioli. Hybrid deterministic-statistical analysis of vibro-acoustic systems with domain couplings on statistical components. *Journal of Sound and Vibration*, 321(3):893–912, 2009.

[116] G. Tanner. Dynamical energy analysis—determining wave energy distributions in vibro-acoustical structures in the high-frequency regime. *Journal of Sound and Vibration*, 320(4):1023–1038, 2009.

[117] D. J. Chappell and G. Tanner. Solving the stationary liouville equation via a boundary element method. *Journal of Computational Physics*, 234:487–498, 2013.

[118] W. Desmet. *A wave based prediction technique for coupled vibro-acoustic analysis*. PhD thesis, Katholieke Universiteit Leuven, 1998.

[119] E. Deckers, O. Atak, L. Coox, R. D'Amico, H. Devriendt, S. Jonckheere, K. Koo, B. Pluymers, D. Vandepitte, and W. Desmet. The wave based method: An overview of 15 years of research. *Wave Motion*, 51(4):550–565, 2014.

[120] P. Ladeveze, L. Arnaud, P. Rouch, and C. Blanzé. The variational theory of complex rays for the calculation of medium-frequency vibrations. *Engineering Computations*, 18(1/2):193–214, 2001.

[121] H. Riou, P. Ladeveze, and P. Rouch. Extension of the variational theory of complex rays to shells for medium-frequency vibrations. *Journal of Sound and Vibration*, 272(1):341–360, 2004.

[122] H. Riou, P. Ladevèze, and L. Kovalevsky. The variational theory of complex rays: An answer to the resolution of mid-frequency 3d engineering problems. *Journal of Sound and Vibration*, 332(8):1947–1960, 2013.

[123] P. Gardonio and M. J. Brennan. On the origins and development of mobility and impedance methods in structural dynamics. *Journal of Sound and vibration*, 249(3):557–573, 2002.

[124] F. A. Firestone. The mobility method of computing the vibration of linear mechanical and acoustical systems: Mechanical-electrical analogies. *Journal of Applied Physics*, 9(6):373–387, 1938.

[125] E. L. Hixson. Mechanical impedance. *Shock and vibration handbook*, pages 10–1, 1976.

[126] S. Rubin. Mechanical immittance-and transmission-matrix concepts. *The Journal of the Acoustical Society of America*, 41(5):1171–1179, 1967.

[127] S. M. Kim and M. J. Brennan. A compact matrix formulation using the impedance and mobility approach for the analysis of structural-acoustic systems. *Journal of Sound and Vibration*, 223(1):97–113, 1999.

[128] L. Cremer and M. Heckl. Structure-borne sound: structural vibrations and sound radiation at audio frequencies. *Berlin and New York, Springer-Verlag, 1988, 590 p. Translation.*, 1, 1988.

[129] G. J. O'Hara. Mechanical impedance and mobility concepts. *The journal of the Acoustical Society of America*, 41(5):1180–1184, 1967.

[130] B. Petersson and J. Plunt. On effective mobilities in the prediction of structure-borne sound transmission between a source structure and a receiving structure, part i: Theoretical background and basic experimental studies. *Journal of Sound and Vibration*, 82(4):517–529, 1982.

[131] B. Petersson and J. Plunt. On effective mobilities in the prediction of structure-borne sound transmission between a source structure and a receiving structure, part ii: Procedures for the estimation of mobilities. *Journal of Sound and Vibration*, 82(4):531–540, 1982.

[132] B. Petersson. An approximation for the point mobility at the intersection of two perpendicular plates. *Journal of Sound and Vibration*, 91(2):219–238, 1983.

[133] B. Petersson. A thin-plate model for the moment mobility at the intersection of two perpendicular plates. *Journal of sound and vibration*, 108(3):471–485, 1986.

[134] J. M. Mondot and B. Petersson. Characterization of structure-borne sound sources: the source descriptor and the coupling function. *Journal of sound and vibration*, 114(3):507–518, 1987.

[135] B. A. T. Petersson and B. M. Gibbs. Use of the source descriptor concept in studies of multi-point and multi-directional vibrational sources. *Journal of Sound and Vibration*, 168(1):157–176, 1993.

[136] B. A. T. Petersson and B. M. Gibbs. Towards a structure-borne sound source characterization. *Applied Acoustics*, 61(3):325–343, 2000.

[137] I. D. Wilken and W. Soedel. The receptance method applied to ring-stiffened cylindrical shells: analysis of modal characteristics. *Journal of Sound and Vibration*, 44(4):563–576, 1976.

[138] I. D. Wilken and W. Soedel. Simplified prediction of the modal characteristics of ring-stiffened cylindrical shells. *Journal of Sound and Vibration*, 44(4):577–589, 1976.

[139] M. El-Raheb and P. Wagner. Acoustic radiation from a shell with internal structures. *The Journal of the Acoustical Society of America*, 85(6):2452–2464, 1989.

[140] D. T. Huang and W. Soedel. Natural frequencies and modes of a circular plate welded to a circular cylindrical shell at arbitrary axial positions. *Journal of Sound and Vibration*, 162(3):403–427, 1993.

[141] D. T. Huang and W. Soedel. On the free vibrations of multiple plates welded to a cylindrical shell with special attention to mode pairs. *Journal of sound and vibration*, 166(2):315–339, 1993.

[142] D. T. Huang and W. Soedel. Study of the forced vibration of shell-plate combinations using the receptance method. *Journal of Sound and Vibration*, 166(2):341–369, 1993.

[143] M. Chen, K. Xie, J. Wei, and N. Deng. An analytical substructure method for the analysis of vibration characteristics on conical-cylindrical-spherical combined shells in vacuum. Inter-noise, Melbourne, Australia, 2014.

[144] M. Ouisse, L. Maxit, C. Cacciolati, and J.-L. Guyader. Patch transfer functions as a tool to couple linear acoustic problems. *Journal of vibration and acoustics*, 127(5):458–466, 2005.

[145] J.-D. Chazot and J.-L. Guyader. Prediction of transmission loss of double panels with a patch-mobility method. *The Journal of the Acoustical Society of America*, 121(1):267–278, 2007.

[146] M. Aucejo, L. Maxit, N. Totaro, and J.-L. Guyader. Convergence acceleration using the residual shape technique when solving structure–acoustic coupling with the patch transfer functions method. *Computers & Structures*, 88(11):728–736, 2010.

[147] L. Maxit, M. Aucejo, and J.-L. Guyader. Improving the patch transfer function approach for fluid-structure modelling in heavy fluid. *Journal of Vibration and Acoustics*, 134(5):051011, 2012.

[148] G. Veronesi, C. Albert, E. Nijman, J. Rejlek, and A. Bocquillet. Patch transfer function approach for analysis of coupled vibro-acoustic poblems involving porous materials. *SAE Technical Paper*, 2014-01-2092, 2014.

[149] M. Boucher, B. Pluymers, and W. Desmet. Coupled (vibro-) acoustic problems using geometrical acoustics and patch transfer functions. ICSV22, Florence, Italy, 2015.

[150] L. Maxit. Scattering model of a cylindrical shell with internal axisymmetric frames by using the circumferential admittance approach. *Applied Acoustics*, 80:10–22, 2014.

[151] M. R. Peterson and D. E. Boyd. Free vibrations of circular cylinders with longitudinal, interior partitions. *Journal of Sound and Vibration*, 60(1):45–62, 1978.

[152] R. S. Langley. A dynamic stiffness technique for the vibration analysis of stiffened shell structures. *Journal of Sound and Vibration*, 156(3):521–540, 1992.

[153] J. Missaoui and L. Cheng. Vibroacoustic analysis of a finite cylindrical shell with internal floor partition. *Journal of Sound and Vibration*, 226(1):101–123, 1999.

[154] Y.-S. Lee and M.-H. Choi. Free vibrations of circular cylindrical shells with an interior plate using the receptance method. *Journal of Sound and Vibration*, 248(3):477–497, 2001.

[155] Z. Zhao, M. Sheng, and Y. Yang. Vibration transmission of a cylindrical shell with an interior rectangular plate with the receptance method. *Advances in Acoustics and Vibration*, 2012, 2012.

[156] E. Rebillard, B. Laulagnet, and J.-L. Guyader. Influence of an embarked spring-mass system and defects on the acoustical radiation of a cylindrical shell. *Applied Acoustics*, 36(2):87–106, 1992.

[157] J. D. Achenbach, J. Bjarnason, and T. Igusa. Effect of a vibrating substructure on acoustic radiation from a cylindrical shell. *Journal of Vibration and Acoustics*, 114(3):312–318, 1992.

[158] J. Bjarnason, J. D. Achenbach, and T. Igusa. Acoustic radiation from a cylindrical shell with an internal plate. *Wave Motion*, 15(1):23–41, 1992.

[159] S.-H. Choi, J. D. Achenbach, and T. Igusa. The effect of periodically attached substructures on the excitation of submerged cylindrical shells. *Journal of Sound and Vibration*, 177(3):379–392, 1994.

[160] S.-H. Choi, T. Igusa, and J. D. Achenbach. Nonaxisymmetric vibration and acoustic radiation of a submerged cylindrical shell of finite length containing internal substructures. *The Journal of the Acoustical Society of America*, 98(1):353–362, 1995.

[161] S.-H. Choi, T. Igusa, and J. D. Achenbach. Acoustic radiation from a finite-length shell with non-axisymmetric substructures using a surface variational principle. *Journal of Sound and Vibration*, 197(3):329–350, 1996.

[162] B. Laulagnet and J.-L. Guyader. Sound radiation from finite cylindrical shells, partially covered with longitudinal strips of compliant layer. *Journal of Sound and Vibration*, 186(5):723–742, 1995.

[163] J. M. Cuschieri and D. Feit. Influence of circumferential partial coating on the acoustic radiation from a fluid-loaded shell. *The Journal of the Acoustical Society of America*, 107(6):3196–3207, 2000.

[164] D. M. Photiadis, B. H. Houston, E. G. Williams, and J. A. Bucaro. Resonant response of complex shell structures. *The Journal of the Acoustical Society of America*, 108(3):1027–1035, 2000.

[165] J. A. Bucaro, A. J. Romano, A. Sarkissian, D. M. Photiadis, and B. H. Houston. Local admittance model for acoustic scattering from a cylindrical shell with many internal oscillators. *The Journal of the Acoustical Society of America*, 103(4):1867–1873, 1998.

[166] G. Maidanik. Response of ribbed panels to reverberant acoustic fields. *The Journal of the Acoustical Society of America*, 34(6):809–826, 1962.

[167] M. H. Marcus and B. H. Houston. The effect of internal point masses on the radiation of a ribbed cylindrical shell. *The Journal of the Acoustical Society of America*, 112(3):961–965, 2002.

[168] S. Sadiq. Submerged double cylinder multi-excitation analysis through linear superposition method with FEM-BEM experimental approach. In *Proceedings of International Bhurban Conference on Applied Sciences & Technology, Islamabad, Pakistan*, 2010.

[169] H. Peters, R. Kinns, and N. J. Kessissoglou. Effects of internal mass distribution and its isolation on the acoustic characteristics of a submerged hull. *Journal of Sound and Vibration*, 333(6):1684–1697, 2014.

[170] C. Li, J. Su, J. Wang, and H. Hua. Effects of symmetrical foundation on sound radiation from a submarine hull structure. *The Journal of the Acoustical Society of America*, 138(5):3195–3201, 2015.

[171] M. M. Ettouney, R. P. Daddazio, and N. N. Abboud. The interaction of a submerged axisymmetric shell and three-dimensional internal systems. *International Journal for Numerical Methods in Engineering*, 37(17):2951–2970, 1994.

[172] V. Meyer, L. Maxit, J.-L. Guyader, T. Leissing, and C. Audoly. A condensed transfer function method as a tool for solving vibroacoustic problems. *Proc IMechE Part C: J Mechanical Engineering Science*, 230(6):928–938, 2016.

[173] V. Meyer, L. Maxit, J.-L. Guyader, and T. Leissing. Prediction of the vibroacoustic behavior of a submerged shell with non-axisymmetric internal substructures by a condensed transfer function method. *Journal of Sound and Vibration*, 360:260–276, 2016.

[174] R. D. Mindlin. Influence of rotary inertia and shear on flexural motions of isotropic elastic plates. 18:31–38.

[175] B. Fornberg. *A practical guide to pseudospectral methods*, volume 1. Cambridge university press, Cambridge, 1998.

[176] A. J. Jerri. The shannon sampling theorem – its various extensions and applications: A tutorial review. *Proceedings of the IEEE*, 65(11):1565–1596, 1977.

[177] P. A. Nelson and S.-H. Yoon. Estimation of acoustic source strength by inverse methods: Part I, conditioning of the inverse problem. *Journal of sound and vibration*, 233(4):639–664, 2000.

[178] E. G. Williams, B. H. Houston, and J. A. Bucaro. Experimental investigation of the wave propagation on a point-driven, submerged capped cylinder using k-space analysis. *The Journal of the Acoustical Society of America*, 87(2):513–522, 1990.

[179] V. Meyer, L. Maxit, J.-L. Guyader, C. Audoly, and Y. Renou. Vibrations et rayonnement acoustique des coques cylindriques raidies : étude expérimentale de l'influence des structures internes non-axisymétriques. Congrès Français d'Acoustique, Le Mans, France, 2016.

[180] F. J. Fahy and P. Gardonio. *Sound and structural vibration: radiation, transmission and response*. Academic press, Cambridge, 2007.

[181] J. Van de Loock. *Étude de la source de rayonnement acoustique des résonances générées dans une coque cylindrique partiellement immergée. Application au domaine de l'éolien offshore.* PhD thesis, Université du Havre, 2015.

[182] G. Maidanik and J. Dickey. Localization and delocalization in periodic one-dimensional dynamic systems. *Acta Acustica united with Acustica*, 73(3):119–128, 1991.

[183] G. Maidanik and K. J. Becker. Potential for the presence of additional stop bands in the modal response of regularly ribbed cylinders. *The Journal of the Acoustical Society of America*, 104(2):700–707, 1998.

[184] G. Maidanik and J. Dickey. Quadratic and energy estimates of the partial response of ribbed panels. *The Journal of the Acoustical Society of America*, 94(3):1435–1444, 1993.

[185] G. Maidanik and J. Dickey. Influence of variations in loss factor of a panel and line impedances of attached ribs. *The Journal of the Acoustical Society of America*, 94(3):1445–1452, 1993.

[186] L. Maxit. Wavenumber space and physical space response of a periodically ribbed plate to a point drive: A discrete approach. *Applied Acoustics*, 70:563–578, 2009.

[187] D. Havelock, S. Kuwano, and M.l Vorländer. *Handbook of signal processing in acoustics*. Springer Science & Business Media, 2008.

[188] C. R. Fuller. The effects of wall discontinuities on the propagation of flexural waves in cylindrical shells. *Journal of Sound and Vibration*, 75(2):207–228, 1981.

[189] C. R. Fuller and F. J. Fahy. Characteristics of wave propagation and energy distributions in cylindrical elastic shells filled with fluid. *Journal of sound and vibration*, 81(4):501–518, 1982.

[190] ISO. 9614-2. *Acoustics – Determination of sound power levels of noise sources using sound intensity – Part II: Measurement by scanning*, 1996.

[191] C. Li, J. Wang, and H. Hua. Experimental investigation of submerged shaft-hull coupled models with different types of base in vibration and radiation. 22nd International Congress on Sound and Vibration, Florence, Italy, 2015.

[192] J. Su, C. Li, and H. Hua. Numerical and experimental study on the vibro-acoustic characteristics of coupled propeller-shaft-hull structures. 22nd International Congress on Sound and Vibration, Florence, Italy, 2015.

[193] V. Meyer, L. Maxit, J.-L. Guyader, T. Leissing, and C. Audoly. Scattering of a periodically stiffened submerged shell coupled to non-axisymmetric internal frames. 22nd International Congress on Sound and Vibration, Florence, Italy, 2015.

[194] L. Maxit. Circumferential admittance approach for vibro-acoustic prediction of a submerged cylindrical shell with rib aperiodicity and transversal bulkhead. Acoustics'08, Paris, France, 2008.

[195] V. Meyer, L. Maxit, Y. Renou, and C. Audoly. Vibroacoustic modeling of submerged stiffened cylindrical shells with internal structures under random excitations. Inter-noise, Hamburg, Germany, 2016.

[196] F. J. Fahy. Some applications of the reciprocity principle in experimental vibroacoustics. *Acoustical Physics*, 49(2):217–229, 2003.

[197] E. A. Skelton and J. H. James. Acoustics of an anisotropic layered cylinder. *Journal of sound and vibration*, 161(2):251–264, 1993.

[198] C. Marchetto, L. Maxit, O. Robin, and A. Berry. Caractérisation expérimentale de structures sous champ acoustique diffus : mesure des fonctions de sensibilité par principe de réciprocité. CFA/VISHNO 2016, Le Mans, France, 2016.

[199] M. S. Howe. Surface pressures and sound produced by turbulent flow over smooth and rough walls. *The Journal of the Acoustical Society of America*, 90(2):1041–1047, 1991.

[200] M. Goody. Empirical spectral model of surface pressure fluctuations. *AIAA journal*, 42(9):251–264, 2004.

[201] V. Meyer, L. Maxit, and C. Audoly. A substructuring approach for modeling the acoustic scattering from stiffened submerged shells coupled to non-axisymmetric internal structures. *The Journal of the Acoustical Society of America*, 140(3):1609–1617, 2016.

[202] V. Meyer, L. Maxit, J.-L. Guyader, T. Leissing, and C. Audoly. A condensed transfer function method as a tool for solving vibroacoustic problems. NOVEM 2015, Dubrovnik, Croatia, 2015.

[203] L. Maxit and V. Meyer. Condensed transfer function (CTF) method as a tool for substructuring vibro-acoustic problem. Inter-noise, San Francisco, CA, USA, 2015.

FOLIO ADMINISTRATIF

THESE DE L'UNIVERSITE DE LYON OPEREE AU SEIN DE L'INSA LYON

NOM : MEYER

DATE de SOUTENANCE : 28/10/2016

Prénoms : Valentin, Noël

TITRE : Development of a substructuring approach to model the vibroacoustic behavior of submerged stiffened cylindrical shells coupled to non-axisymmetric internal frames

NATURE : Doctorat

Numéro d'ordre : 2016LYSEI111

Ecole doctorale : Mécanique - Energétique - Génie civil - Acoustique

Spécialité : Acoustique

RESUME : De nombreux travaux dans la littérature se sont concentrés sur la modélisation vibro-acoustique de coques cylindriques raidies immergées, du fait des nombreuses applications industrielles, en particulier dans le domaine aéronautique ou naval. Cependant, peu d'entre elles prennent en compte des structures internes non-axisymétriques telles que des supports moteurs, des planchers ou des carlingages, qui peuvent avoir une influence importante sur le comportement vibro-acoustique du système. C'est pourquoi une méthode de sous-structuration baptisée CTF est présentée dans cette thèse. Elle est développée dans le cas général de deux structures minces couplées le long d'une ligne. Un ensemble de fonctions orthonormées, baptisées fonctions de condensation, est défini afin d'approximer les forces et déplacements à la jonction entre les sous-systèmes. Des fonctions de transfert condensées sont définies pour chaque sous-système découplé. L'utilisation du principe de superposition, de l'équilibre des forces et de la continuité des déplacements permet de déduire le comportement des sous-systèmes couplés. La méthode est d'abord développée et validée dans le cas de plaques, puis ensuite appliquée au cas d'une coque cylindrique raidie immergée couplée à des structures internes non-axisymétriques. Le système est dans ce cas décomposé en 3 familles de sous-systèmes : la coque cylindrique immergée décrite par une méthode semi-analytique basée sur la résolution des équations de Flügge dans le domaine des nombres d'onde, les structures internes axisymétriques (raidisseurs, cloisons) décrites par éléments finis axisymétriques et les structures non-axisymétriques décrites pas des modèles éléments finis. La méthode CTF est appliquée à différents cas tests afin de montrer l'influence des structures internes non-axisymétriques sur le comportement vibro-acoustique d'une coque cylindrique pour différents types d'excitations pertinents dans le domaine naval : une force ponctuelle, une onde plane acoustique et un champ de pression aléatoire (tel qu'un champ acoustique diffus ou une couche limite turbulente).

MOTS-CLÉS : modélisation numérique, sous-structuration, coque cylindrique raidie, vibro-acoustique, structure interne non-axisymétrique

Laboratoire (s) de recherche : LVA

Directeur de thèse: Laurent Maxit

Président de jury : Cédric Maury

Composition du jury : Christian Audoly, Wim Desmet, Jean-Louis Guyader, Nicole Kessissoglou, Cédric Maury, Laurent Maxit